

**Di-hadron correlations with identified leading  
hadrons at intermediate transverse momentum  
in Pb-Pb 2.76 TeV in ALICE**

*By*

**Subikash Choudhury**

**Enrollment No. : PHYS04201004006**

*Variable Energy Cyclotron Centre, Kolkata*

*A thesis submitted to the  
Board of Studies in Physical Sciences  
In partial fulfillment of requirements  
For the Degree of*

**DOCTOR OF PHILOSOPHY**

*of*



**HOMI BHABHA NATIONAL INSTITUTE**  
**Bhabha Atomic Research Centre**  
**Mumbai-400085, India**

August, 2016

## STATEMENT BY AUTHOR

This dissertation has been submitted in partial fulfillment of requirements for an advanced degree at Homi Bhabha National Institute (HBNI) and is deposited in the Library to be made available to borrowers under rules of the HBNI.

Brief quotations from this dissertation are allowable without special permission, provided that accurate acknowledgement of source is made. Requests for permission for extended quotation from or reproduction of this manuscript in whole or in part may be granted by the Competent Authority of HBNI when in his or her judgment the proposed use of the material is in the interests of scholarship. In all other instances, however, permission must be obtained from the author.

SUBIKASH CHOUDHURY

## DECLARATION

I, hereby declare that the investigation presented in the thesis has been carried out by me. The work is original and has not been submitted earlier as a whole or in part for a degree / diploma at this or any other Institution / University.

SUBIKASH CHOUDHURY

# List of Publications

## In peer-reviewed Journal

1. “*Present and future of QGP research in high energy heavy ion collision experiments*”, Subhasis Chattopadhyay, **Subikash Choudhury**, Debojit Sarkat, **Indian Natn Sci Acad** **81**, **321-335 (2015)**.
2. “*Testing of the coalescence mechanism in high energy heavy ion collisions using two-particle correlations with identified particle trigger*”, **Subikash Choudhury**, Debojit Sarkat, Subhasis Chattopadhyay, **Phys. Rev. C** **93**, **054902 (2016)**.
3. “*Effect of radial flow on two particle correlations with identified triggers at intermediate  $p_T$  in  $p$ -Pb collisions at  $\sqrt{s_{NN}} = 5.02$  TeV*”, Debojit Sarkar, **Subikash Choudhury**, Subhasis Chattopadhyay, **Physics Letters B**, **pp. 763-768 (2016)**.
4. “*Fluctuations in Charged Particle Multiplicities in Relativistic Heavy-Ion Collisions*”, Maitreyee Mukherjee, Sumit Basu, **Subikash Choudhury**, Tapan K. Nayak, **J. Phys. G: Nucl. Part. Phys.** **43**, **085102 (2016)**.
5. “*Fabrication and Characterisation of Oil-Free Large High Pressure Laminate Resistive Plate Chamber*”, Rajesh Ganai, Arindam Roy, Kshitij Agarwal, Zubayer Ahammed, **Subikash Choudhury**, Subhasis Chattopadhyay, **JINST** **11 P04026, (2016)**.

## Conferences and Symposia

1. “*Two particle correlations with identified at intermediate  $p_T$  with identified leading hadrons at the LHC energy using AMPT model*”, **Subikash Choudhury**, Debojit Sarkat, Subhasis Chattopadhyay **Springer Proceedings in Physics, XXI DAE-BRNS, High Energy Physics Symposium Proceedings, pp.183-188.**
2. “*Long Term Performance Studies of Large Oil-Free Bakelite Resistive Plate Chamber*”, Rajesh Ganai, Arindam Roy, Kshitij Agarwal, Zubayer Ahammed, **Subikash Choudhury**, Subhasis Chattopadhyay, **To appear in JINST Conf. Series, arXiv: 1604.03668 [physics.ins-det].**

## ACKNOWLEDGEMENTS

I express my sincerest gratitude to my supervisor, Prof. Subhasis Chattopadhyay for his supervision, training and constant motivation. I thank you Sir, for your patience, enthusiasm and encouragement. My heartfelt thanks to Prof. Tapan Kr. Nayak for his valuable time, immense patience and his constant motivation and encouragement. You have been a nice companion and I have learnt a lot from you. Also thanks for taking loads of my Pre-CERN visits at every occasion. I take this opportunity to thank Dr. Partha Pratim Bhaduri and Dr. Prithwish Tribedy for entertaining me every time a I knocked your doors. Thanks a lot for guiding me and inspiring me throughout the course of this work. Thank you all for your valuable time, your support and for sharing your knowledge and experiences with me. I am indebted to my juniour turned friend Debojit Sarkar for helping me out in every way while doing this analysis. Thanks for shareing all my frustration since last four years. We have lived through several agreements and conflicts but the journey was indeed fascinating and memorable. I am grateful to Dr. Zubayer Ahammed, Dr. Anand K. Dubey, Mr. Sanjib Muhuri, Dr. Premomoy Ghosh, for their valuable suggestions and discussions. I acknowledge the computing facilities of grid-peer Kolkata at VECC. None of this would have happened without the constant, unwavering support of my family and friends. I do not have any words to thank my father and mother. Without your immense love, sacrifice, patience, support and motivation I would not have come this far. My dear friends Arindam, Balaram, Rajesh, Sumit (names placed in alphabetical order) have been a constant source of enthusiasm and inspiration in my life. Thank you for all your help and support on and off the court.

# Contents

<b>SYNOPSIS</b> . . . . .	x
<b>List of Figures</b> . . . . .	xviii
<b>List of Tables</b> . . . . .	xxviii
<b>1 Introduction</b>	<b>1</b>
1.1 The Standard Model . . . . .	3
1.2 The Quantum Chromodynamics . . . . .	5
1.3 QCD Phase structure . . . . .	7
1.4 Heavy Ion Collisions at Relativistic Energy . . . . .	10
1.4.1 Probing the Quark Gluon Plasma . . . . .	10
1.4.2 Motivation of the Present Thesis . . . . .	28
<b>2 Testing of the coalescence mechanism using identified particle angular correlations at intermediate <math>p_T</math></b>	<b>40</b>
2.1 Introduction . . . . .	40
2.2 The AMPT Model . . . . .	43
2.3 Analysis Method . . . . .	45
2.4 Results . . . . .	48
2.4.1 Particle species dependence of $v_2(p_T)$ . . . . .	48
2.4.2 NCQ-scaling of $v_2(p_T)$ . . . . .	53
2.4.3 Baryon enhancement and $\Delta\eta - \Delta\phi$ correlations at intermediate $p_T$ . . . . .	57
2.5 Discussion . . . . .	59
<b>3 A Large Ion Collider Experiment at LHC</b>	<b>67</b>

3.1	The Large Hadron Collider (LHC) . . . . .	68
3.1.1	Accelerating protons . . . . .	69
3.1.2	Pb <sup>82+</sup> Source and its acceleration . . . . .	70
3.1.3	Beam parameters . . . . .	70
3.2	The ALICE Experiment . . . . .	71
3.2.1	The Central Barrel Detectors . . . . .	72
3.2.2	The Forward Detectors . . . . .	81
3.2.3	The Muon Spectrometers . . . . .	84
3.2.4	Data Reconstruction . . . . .	86
<b>4</b>	<b>Dihadron Correlation Measurements</b>	<b>95</b>
4.1	Data sample and Event Selection . . . . .	96
4.1.1	Track Selection . . . . .	98
4.2	Making of Correlation Function . . . . .	100
4.3	Corrections . . . . .	102
4.3.1	Efficiency correction . . . . .	103
4.3.2	Two-Track Efficiency . . . . .	104
4.3.3	Wing Effect . . . . .	107
4.3.4	Resonance Decays . . . . .	109
4.3.5	Validation of Correction Factors: Monte Carlo Closure Test	109
4.4	Yield Extraction . . . . .	110
4.4.1	Flow Subtraction by $\eta$ -gap Method . . . . .	111
4.4.2	Extraction of Near Side Jetlike Yield . . . . .	112
4.5	Results . . . . .	114
4.5.1	$\Delta\phi$ Distributions of Associated Particle Yield . . . . .	116
4.5.2	Integrated Associated Yield . . . . .	120
<b>5</b>	<b>Dihadron Correlations with Identified Trigger Particles at Intermediate- <math>p_T</math></b>	<b>124</b>
5.1	Introduction . . . . .	124
5.2	Particle Identification in ALICE . . . . .	128

5.2.1	Particle Identification using TPC-TOF . . . . .	129
5.2.2	Evaluation of PID efficiency and Misidentification Fractions	134
5.3	Analysis and Correction Procedure . . . . .	136
5.4	Yield Extraction, Results and Discussions . . . . .	138
5.4.1	Track Splitting and Merging effects . . . . .	141
5.4.2	Near Side Depletion in MC models . . . . .	144
5.4.3	Extraction of Near Side Yield . . . . .	146
5.5	Systematic Uncertainty . . . . .	148
5.6	Results and Discussions . . . . .	150
5.6.1	Model Comparision . . . . .	154
<b>Appendix</b>	. . . . .	<b>i</b>

# SYNOPSIS

The work done in this thesis has two parts:

- Understanding the particle production mechanism in high energy heavy collisions at LHC energy. This part of work include a) analysis of the ALICE data and b) model-based studies to understand the particle production mechanisms at intermediate  $p_T$ .
- Development of Resistive Plate Chamber for high-energy physics experiment.

## Particle production mechanism in high energy heavy ion collisions

Heavy ion collisions at ultra-relativistic energy facilitates probing an exotic state of matter where quarks and gluons are no longer bounded as a color neutral object- hadron. As per Quantum Chromodynamics (QCD), the theory of the strongly interacting colored objects (quarks and gluons), at very high temperature and energy density *asymptotic freedom* would lead to a formation of a de-confined state of quarks and gluons known as Quark Gluon Plasma [1, 2, 3]. Results obtained from the experiments at RHIC-BNL have indicated that a strongly coupled nearly perfect liquid was formed in central Au-Au collisions at  $\sqrt{s_{NN}} = 200\text{GeV}$  [4, 5, 6]. Hot and dense matter thus formed, expands, cools and finally undergoes color confinement (hadronization).

Heavy ion programs at RHIC-BNL and LHC-CERN have been dedicated towards precise understanding of dynamics of the strongly interacting system of quarks and gluons and their subsequent evolution to hadrons. The transverse

momentum ( $p_T$ ) distribution of the particles produced in these collisions found to be a crucial observable in characterizing the medium formed at the early stage of collisions [7, 8, 9]. A typical transverse momentum spectrum available from the experiments feature a clear transition from an exponential shape below  $p_T \approx 2$  GeV/ $c$  to a power law behaviour at higher  $p_T$ . While the behaviour at lower  $p_T$  has been found to be consistent with the hydrodynamical evolution of the bulk matter, particle production at higher  $p_T$  is in agreement with the perturbative QCD processes that lead to the fragmentation of the energetic partons originating from the hard scatterings at the primordial stage [10, 11, 12, 13]. However, none of these formalisms could account for the particle production at intermediate  $p_T$  ( $2 < p_T < 6$  GeV/ $c$ ). The  $p_T$  spectra of the identified particles in this  $p_T$  window reveal an unusually enhanced baryon yield as compared to that of the mesons. The nuclear modification factor,  $R_{AA}$  that measures the  $p_T$  dependent modification of particle spectra/yield in nucleus-nucleus collisions as compared to that of the p-p collisions also exhibits lower suppression for baryons compared to mesons at the intermediate  $p_T$  [14, 15]. Lack of agreement with the existing models of particle production discussed earlier calls for a new technique of hadronization.

It has been found, a very simplistic model that involves recombination or coalescence of boosted (anti-)quarks from a collectively expanding source and in close proximity to each-other in the phase-space convincingly replicate the experimental observations. This mechanism of hadronization is commonly referred to as the quark coalescence model [16, 17, 18, 19, 20]. Additionally, the quark number scaling (NCQ) of elliptic flow ( $v_2$ ), a natural outcome of such conjecture was also confirmed from the experimental results [21]. Hence coalescence has been regarded as a plausible mechanism of hadronization at the intermediate  $p_T$ .

At the LHC energy, as per the results at 2.76 TeV Pb-Pb collisions, the constituent quark-scaling seems to be an approximation, differing by  $\sim 20\%$  from perfect scaling [22]. Such an observation has triggered discussion on the relevance of coalescence model in the context hadronization. On the other hand, alternative theoretical ideas based on the mass dependent radial boost pushing the massive hadrons to higher  $p_T$  or baryon generation from gluon junctions found to have reproduced the enhancement observed in the inclusive baryon over meson ratio. Interestingly, the angular correlation measurements at the RHIC in the region of baryon over meson enhancement have revealed that the observed correlation among the particles are consistent with the in-medium jet-fragmentations [23, 24]. This seems to confront with the idea of dominance of the non-perturbative physics processes (hydrodynamics, coalescence and etc) in generating the anomalous baryon enhancement. Following this, various modifications to the coalescence formalism was prescribed that include recombination of quarks from quenched jets (shower partons) and/or thermalized medium quarks (thermal partons) generally known as shower-thermal or shower-shower recombinations. These refinements found to reproduce the inclusive baryon enhancement quantitatively better than that was done previously along with the scaling violation of the elliptic flow ( $v_2$ ) coefficient. As indicated by Fries *et.al.* such recombination schemes may lead to correlated emission of hadrons at small angles (apparently jet-like correlations) even at the intermediate  $p_T$  region [18].

## a) ALICE-Data Analysis

The two-particle angular correlation measurements provide information on the hadron production from the hard-scattering processes. This technique offer a convenient way to probe the influence of the medium on the jet-fragmentations

which are not accessible through the inclusive measurements. In this thesis, I will address how the jet-medium interactions contribute towards particle production in heavy ion collisions at the intermediate  $p_T$  at LHC energy with ALICE detectors. The two particle angular correlation measurements with leading particles (trigger) identified as mesons ( $\pi^\pm$ ) and baryons ( $p/\bar{p}$ ) with un-identified charged hadrons (associated) at intermediate  $p_T$  have been performed in Pb-Pb collisions at 2.76 TeV. Pions and (anti-)protons have been identified on a track-by-track basis through combined  $n\sigma$  PID method using specific energy loss (dE/dx) information from the ALICE-Time Projection Chamber (TPC) and timing information from the ALICE-Time of Flight (TOF) detectors. Details on the particle identifications will be discussed later in this thesis.

The two-dimensional angular correlations obtained in  $\Delta\eta - \Delta\phi$  have been corrected for limited acceptance through mixed event. There are also other correction factors that include detector inefficiencies and contaminations due to the mis-identifications of the particles. These correction factors have been estimated from the Monte-Carlo (MC) productions passed through GEANT to model the detector response. The detector geometry and the reconstruction schemes in MC productions have been done in analogy with the data. To validate the correction factors, MC-closure test have been carried out.

To quantify the effect of medium, the near side per trigger jet-like yield i.e the average number particles associated with a trigger particle is calculated after subtracting the flow-modulated combinatorial background. It is argued that if the origin of enhanced baryon production is associated with the coalescence of quarks, the baryon trigger yield would be less compared to that of meson. This phenomenon is called trigger dilution. Baryon generation being favoured within the coalescence formalism, dilution is expected to be more in central collisions where coalescence is expected to be a dominant mode of hadronization

at intermediate  $p_T$ .

## **b) Model based Study**

Analogous measurements have been carried out using A Multi Phase Transport Model (AMPT) that uses quark-coalescence as an underlying mechanism of hadronization [25]. The simulated data have been analyzed to calculate near side per trigger jet-like yield associated with  $\pi^\pm$  and p/ $\bar{p}$  triggers at the intermediate  $p_T$  in different centrality bins. The centrality dependence of the yield associated with the (anti-)proton trigger have been found to exhibit suppression compared to  $\pi^\pm$  from peripheral to central events. The effect is found to be in compliance with coalescence formalism that predicts dilution of baryon triggered yield in the most central events [27].

The results from analysis of the ALICE-data have been compared with the different event generators like AMPT, EPOS [26]. The outcome of this comparison and its relevance in the context of coalescence as a mechanisms of hadronization have been discussed in this thesis.

## **Development of Resistive Plate Chamber (RPC) for high energy physics experiments**

Resistive Plate Chamber (RPC) is a gas-based detector made of highly resistive materials like glass or High Pressure Laminate (HPL), better known as bakelite. Excellent time resolution (0.5 ns), large surface area and relatively low-cost makes RPC best-choice for triggering and muon detection in high energy experiments. A large size (240 cm  $\times$  120 cm  $\times$  0.2 cm) oil-free bakelite Resistive Plate Chamber (RPC) has been fabricated at VECC-Kolkata using locally available P-302 OLTC grade HPL [28]. The chamber has been subjected to streamer

mode of operation using Argon, Freon (R134a) and Iso-butane in a ratio of 34:57:9 by volume. The performance of the chamber has been characterised by measuring the long term efficiency, its uniformity and stability against the variation of humidity and temperature by detecting the cosmic muons. Timing measurement has been performed at a central location of the chamber. The chamber maintained an efficiency of  $\approx 95\%$  and time resolution at the point of measurement, 0.83 ns at 9000V over a period of 30 days at the time of writing this thesis [29].

# Bibliography

- [1] F. Karsch, Nucl. Phys. A 698, 199 (2002).
- [2] A. Adare et al. (PHENIX Collaboration), Phys. Rev. Lett. 104, 132301 (2010).
- [3] M. Wilde (ALICE Collaboration), Nucl. Phys. A 904-905, 573c (2013).
- [4] G. Kestin and U. W. Heinz, Eur. Phys. J. C 61, 545 (2009).
- [5] H. Song, S. A. Bass, U. Heinz, T. Hirano, C. Shen, Phys. Rev. Lett. 106, 192301 (2011).
- [6] D. Teaney, J. Lauret and E. V. Shuryak, Phys. Rev. Lett. 86, 4783 (2001).
- [7] J. L. Klay et al. (STAR Collaboration), Nucl. Phys. A, 715-733 (2003).
- [8] S. S. Adler et al. (PHENIX Collaboration), Phys. Rev. C 69, 034909 (2004).
- [9] B. Abelev et al. (ALICE Collaboration), Phys. Rev. C 88, 044910 (2013).
- [10] S. A. Bass and A. Dumitru, Phys. Rev. C 61, 064909 (2000).
- [11] T. Hirano et al., Phys. Rev. C 77, 044909 (2008).
- [12] F. Arleo, Eur. Phys. J. C 61, 603-627 (2009).
- [13] D. d'Enterria and B. Betz, High- $p_T$  Hadron Suppression and Jet Quenching. Lect. Notes. Phys. 785, 285-339 (2010).

- [14] B. Abelev et al. (ALICE Collaboration) Phys. Lett. B. 736, 196-207 (2014).
- [15] B. I. Abelev et al. (STAR Collaboration) Phys. Rev. Lett. 97, 152301 (2006).
- [16] R. Fries, B. Müller, C. Nonaka, and S. Bass, Phys. Rev. Lett. 90, 202303 (2003).
- [17] R. J. Fries, B. Müller, C. Nonaka and S. A. Bass , Phys. Rev. C 68, 044902 (2003).
- [18] R. J. Fries, S. A. Bass and B. Müller Phys. Rev. Lett. 94, 122301 (2005) .
- [19] V. Greco, C. Ko, and P. Lévai, Phys. Rev. Lett. 90 (2003) 202302.
- [20] R. Hwa and C. B. Yang, Phys. Rev. C 70, 024904 (2004).
- [21] A. Adare et al.(PHENIX Collaboration), Phys. Rev. C 85 064914 (2012).
- [22] B.Abelev et al. (ALICECollaboration), J.High Energy Phys. 06, 190 (2015).
- [23] S.S. Adler et. al (PHENIX Collaboration) Phys. Rev. C 71, 051902 (2005).
- [24] L. Adamczyk et al. (STAR Collaboration), Phys. Lett. B 751, 233 (2015).
- [25] Zi-Wei Lin et. al, Phys. Rev. C 72, 064901 (2005).
- [26] K. Werner et. al, Phys. Rev. C 85, 064907 (2012).
- [27] S. Choudhury, D. Sarkar and S. Chattopadhyay, Phys. Rev. C 93, 054902 (2016).
- [28] R. Ganai et. al., 2016 JINST 11 P04026, arXiv:1510.02028.
- [29] R. Ganai et. al., arXiv:1604.03668 .

# List of Figures

1.1	(Color online) A pictorial depiction on the chronological evolution of the universe after the Big Bang . . . . .	2
1.2	(Color online) Three generations of the Standard Model elementary particles and the quanta of their fundamental interactions .	4
1.3	(Color online) The strong coupling constant $\alpha_s$ as a function of the momentum transfer $Q$ . A manifestation of <i>asymptotic freedom</i> . . . . .	5
1.4	(Color online) An artist's impression when quark-(anti)quark pair is stretched, representing the increase in static quark-(anti)quark potential . . . . .	7
1.5	(Color online) Lattice QCD prediction on the temperature dependence of energy density of QCD medium, showing an abrupt change in the energy density below and above a critical temperature ( $T_c$ ) - an evidence of phase change [13]. . . . .	8
1.6	(Color online) <b>Left panel:</b> Phase diagram in $T$ - $\mu_B$ space as conjectured by the Lattice QCD. <b>Right Panel:</b> $T$ - $\mu_B$ coordinate space representations of heavy-ion collisions at RHIC-BES, LHC and FAIR. . . . .	9
1.7	(Color online) A schematic representation of different stages of a heavy ion collision [16]. . . . .	10
1.8	(Color online) <b>Top:</b> $\sqrt{s_{NN}}$ dependence of Bjorken energy density ( $\varepsilon_{Bj}$ ) for Au-Au, Cu-Au, and Cu-Cu collisions at $\sqrt{s_{NN}} = 200$ and 62.4 GeV [22]. <b>Bottom:</b> The values of Bjorken energy density are shown for Pb-Pb collisions at LHC energy, together with energies available for Au-Au collisions at RHIC [23]. . . . .	12
1.9	(Color online) A schematic representation of nucleon profile in an asymmetric heavy ion collision. Also highlighted dominant initial anisotropy- elliptic( <b>left</b> ) and triangular ( <b>right</b> ) . . . . .	14

1.10 (Color online) The mass and baryon-meson ordering of $v_2(p_T)$ of identified particles at low and intermediate $p_T$ : <b>(left)</b> Au-Au $\sqrt{s_{NN}} = 130$ GeV [44]. <b>(right)</b> Au-Au $\sqrt{s_{NN}} = 200$ GeV [45]. The Solid lines on the figure in the left panel show the predictions from hydrodynamic calculations . . . . .	15
1.11 (Color online) The $v_2(p_T)$ of identified particles showing mass and baryon-meson ordering at low and intermediate $p_T$ of Pb-Pb collisions at $\sqrt{s_{NN}} = 2.76$ TeV [46]. . . . .	16
1.12 (Color online) Measurement of $R_{AA}$ in central heavy ion collisions at $\sqrt{s_{NN}} = 17.3$ GeV, 200 GeV and 2.76 TeV [51, 52, 53, 54, 55, 56, 57]. Also shown comparison with different model predictions[58, 59, 60, 61] . . . . .	18
1.13 (Color online) The nuclear modification factor $R_{AA}$ as a function of $p_T$ for $\pi$ , K, $p/\bar{p}$ and hadrons. Results are shown for different collision centralities [91]. . . . .	20
1.14 (Color online) Baryon-to-meson ratio in Jet and bulk. (top) $p/\pi$ [66] and (bottom) $\Lambda/K_s^0$ [67]. . . . .	21
1.15 (Color online) <b>Left:</b> $R_{AA}$ of D-meson as a function of $p_T$ in central Pb-Pb collisions at $\sqrt{s_{NN}} = 2.76$ TeV [70] compared to $D_s^0$ [75], charged particle [69] and pion [91] $R_{AA}$ . <b>Right:</b> D-meson [77] and non-prompt $J/\psi$ [78, 73] $R_{AA}$ as a function of centrality in Pb-Pb collisions at the LHC. . . . .	22
1.16 (Color online) Measurement of nuclear effects on direct photons in different collision centrality for Pb-Pb collisions at $\sqrt{s_{NN}} = 2.76$ TeV compared with number of binary collision scaled pQCD calculation [79]. . . . .	23
1.17 (Color online) $Z$ boson $R_{AA}$ in Pb-Pb collisions at $\sqrt{s_{NN}} =$ as a function of centrality, rapidity and transverse momentum comparing the muon and electron channel results . . . . .	24
1.18 (Color Online) <b>Top:</b> The inclusive $p/\pi$ and $\bar{p}/\pi^-$ ratio from d-Au and Au-Au at $\sqrt{s_{NN}} = 200$ GeV. The dotted-dashed lines shows the inclusive $p/\pi$ ratio from light quark jets in $e^+ + e^-$ collisions at 91.2 GeV. Also shown comparisons with different model calculations. <b>Bottom:</b> $p_T$ -dependence of particle ratios measured in pp and 0-5% most central Pb-Pb collisions at 2.76 TeV. Comparison with theoretical predictions for 0-5% Pb-Pb collisions are also shown. . . . .	25
1.19 (Color online) Pictorial representation of coalescence mechanism of hadronization from hot and dense quark gluon plasma. . . . .	26

1.20	(Color online) The $p_T/n_q$ or $KE_T/n_q$ dependence of $v_2/n_q$ for identified hadrons, $n_q$ is the number of valance quarks in a given hadron( for mesons, $n_q = 2$ ;and,for baryons $n_q =3$ ): (left) minimum bias Au-Au $\sqrt{s_{NN}} = 200$ GeV, (right) for 10-20 % collision centrality in Pb-Pb $\sqrt{s_{NN}} = 2.76$ TeV. . . . .	27
1.21	(Color online) Double ratio of $v_2/n_q$ as a function of $p_T/n_q$ relative to the seventh order polynomial fit to $v_2/n_q$ of $p/\bar{p}$ for Pb-Pb $\sqrt{s_{NN}} = 2.76$ TeV in 10-20% collision centrality[46] . . . . .	29
2.1	(Color online) (a) The 2D correlation function taking unidentified charged hadrons as both trigger and associated particles. Transverse momentum of trigger and associated particles are mentioned in the text. (b) $\Delta\phi$ projection of the 2D function for different $\Delta\eta$ regions as indicated in the plot. (c) Near side jet-like region after bulk subtraction . . . . .	47
2.2	(Color online) Elliptic flow parameter $v_2$ for pions( $\pi^+ + \pi^-$ ), kaons ( $K^+ + K^-$ ) phi mesons( $\phi$ ) and protons ( $p^+ + \bar{p}$ ) as a function of transverse momentum calculated from the SM version of AMPT (a) with hadronic rescattering (ART) (b) without hadronic rescattering (No ART) in 20-40% Pb-Pb collisions at $\sqrt{s_{NN}} = 2.76$ TeV. . . . .	48
2.3	(Color online) Ratio of $v_2^\phi(p_T)/v_2^p(p_T)$ as a function of transverse momentum calculated from the SM version of AMPT (a) with hadronic rescattering (ART) (b) without hadronic rescattering (No-ART) in 20-40% Pb-Pb collisions at $\sqrt{s_{NN}} = 2.76$ TeV. Filled boxes represent statistical uncertainties . . . . .	50
2.4	(Color online) Transverse momentum dependence $v_2$ of $\phi$ -mesons calculated from the SM version of AMPT with ART (solid star), without ART (solid circle) and with ART but $K\bar{K} \rightarrow \phi$ forbidden (solid square) in 20-40% Pb-Pb collisions at $\sqrt{s_{NN}} = 2.76$ TeV. Filled boxes and the bands represent statistical uncertainties . . . . .	52
2.5	(Color online) The $v_2$ of identified particles for different hadronic cascade time scaled by their respective quark content $n_q$ plotted as a function of $p_T/n_q$ for 0-40% Au-Au collisions at $\sqrt{s_{NN}} = 200$ GeV. Bottom panel shows the ratio with respect to a fit to $K_s^0$ - $v_2$ . . . . .	54
2.6	(Color online) $v_2/n_q$ for some identified particles as a function of $p_T/n_q$ for different hadronic cascade time ((a)30, (c)10 and (e)0.6 fm/c) in 20-40% Pb-Pb collisions at $\sqrt{s_{NN}} = 2.76$ TeV. Bottom panel shows the ratio with respect to a fit to $K_s^0$ - $v_2$ . . . . .	56

2.7	(Color online) The ratio of the yields of proton to pion from two versions of AMPT in Pb-Pb collisions at $\sqrt{s} = 2.76$ TeV. The ratio in SM version (a) shows a clear peak around 2 GeV/c as opposed to the default version (b) which does not show any such peak. . . . .	57
2.8	(Color online) $\Delta\eta$ - $\Delta\phi$ correlation function in 40-60 % centrality of Pb-Pb collisions at $\sqrt{s} = 2.76$ TeV from AMPT SM with proton (a) and pion (b) as trigger particles. . . . .	58
2.9	(Color online) Centrality dependence of the near side yield from the background subtracted correlation function. The yields from default version of AMPT have been multiplied by 1.5 for better visualisation. . . . .	60
2.10	(Color online) Ratio of proton trigger yield to pion trigger yield ( $Y^p/Y^\pi$ ) at high and intermediate $p_{T,trigger}$ regions as indicated in the figure . . . . .	61
2.11	(Color online) Ratio of proton trigger yield to pion trigger yield ( $Y^p/Y^\pi$ ) for Au+Au collisions at $\sqrt{s} = 200$ AGeV, results from PHENIX ([22] superposed. . . . .	62
3.1	(Color online) Aerial view of the LHC complex . . . . .	68
3.2	(Color online) LHC acceleration and collision schemes [3] . . . . .	69
3.3	(Color online) A schematic view of ALICE detector system. The central-barrel detectors are ITS, TPC, TRD, TOF, PHOS, EM-Cal, and HMPID. The forward detectors are PMD, FMD, V0 (often called VZERO in the text), T0, ZDC, and the MUON-spectrometers. Photo Courtesy: CERN Document Server (ALICE-PHO-GEN-2012-001-12). . . . .	72
3.4	(Color online) A schematic view of ALICE-Inner Tracking Chamber. Also shown different sub-layers: SPD, SDD and SSD. . . . .	74
3.5	(Color online) Schematics of ALICE-TPC [7] . . . . .	77
3.6	(Color online) <b>Left:</b> Energy-loss, $\frac{dE}{dx}$ versus momentum (p) in the TPC active volume. For each particle there is a distinctly separated band below $p_T < 1$ GeV/c which merges at higher $p_T$ . <b>Right:</b> Transverse momentum resolution of the tracks upto 100 GeV/c for ITS-TPC combined tracks [10]. . . . .	78
3.7	(Color online) TOF $\beta = v/c = L/tc$ distribution as measured by ALICE-TOF detector as a function of momentum in Pb-Pb collisions at $\sqrt{s_{NN}} = 2.76$ TeV . . . . .	79
3.8	(Color online) Photograph of 10-gap glass-MRPC used to fabricate ALICE-TOF [13]. . . . .	80

3.9	(Color online) V0 detector modules [17] . . . . .	83
3.10	(Color online) Comparison of centrality percentile resolutions as a function of centrality for different centrality estimators used in ALICE [15] . . . . .	84
3.11	(Color online) A schematic diagram of Muon Spectrometer [21, 22]	85
3.12	(Color online) <b>Left:</b> Three distinct event classes can be characterized using correlations between sum and difference of signal time information available from V0A and V0C : <b>a)</b> collision at IP (8.3 ns, 14.3 ns), <b>b)</b> beam background behind V0A (-14.3 ns, -8.3 ns) and <b>c)</b> beam background V0C (14.3 ns, 8.3 ns). <b>Right:</b> A schematic diagram showing arrival time of particles from different locations of beam induced interactions to the V0 detectors [25]. . . . .	88
4.1	(Color online) The Z-vertex position distribution of all minimum biased events, and those selected for this analysis are shown in different colors . . . . .	96
4.2	(Color online) An event statistics bar-chart: showing number of events collected after each selection cuts . . . . .	97
4.3	(Color online) Parameters after filtering through hybrid track cuts: <b>a)</b> $DCA_{xy}$ distribution, <b>b)</b> $DCA_z$ distribution, <b>c)</b> number of TPC clusters and, <b>d)</b> TPC $\chi^2$ /per cluster distribution. Y-axis of all plots represents counts in arbitrary unit (a.u.) . . . . .	99
4.4	(Color online) $\eta, \phi$ distributions of hybrid tracks . . . . .	99
4.5	(Color online) <b>(a)</b> Same event pairs ( $S(\Delta\eta, \Delta\phi)$ ), <b>(b)</b> mixed event pairs ( $B(\Delta\eta, \Delta\phi)$ ) and <b>(c)</b> ratio of same event over mixed event pairs . . . . .	100
4.6	(Color online) <b>(a)</b> The transverse momentum dependence of single particle efficiency in 0%-10% central events. <b>(b)</b> the ratio of the same in central and peripheral events, for Pb-Pb collisions at 2.76 TeV . . . . .	103
4.7	(Color online) Two track separation in the transverse plane . . .	105
4.8	(Color online) Same and mixed event distributions <b>top:</b> without and <b>bottom:</b> with applying the two-track efficiency cut [21]. . .	106
4.9	(Color online) 1-D $\Delta\phi$ ( $\Delta\eta$ ) projections without <b>(black)</b> and with <b>(red)</b> applying the two-track efficiency cut [21]. . . . .	106

4.10 (Color online) 1-D $\Delta\eta$ projections of the correlation function at $\Delta\phi = \pi \pm 0.25$ (red) and $\Delta\phi = \pi/2 \pm 0.25$ (black) in different $p_{T,trig}$ , $p_{T,asso}$ , and centrality classes (( <b>a</b> ) 60%-90% and ( <b>b</b> ) 0%-10%), obtained from MC HIJING simulations. Plot shows <i>wing</i> -like structures at large $\Delta\eta$ . . . . .	107
4.11 (Color online) 1-D $\Delta\eta$ projections of the correlation function at $\Delta\phi = \pi \pm 0.25$ (red) and $\Delta\phi = \pi/2 \pm 0.25$ (black) in different $p_{T,trig}$ , $p_{T,asso}$ , and centrality classes (( <b>a</b> ) 60%-90% and ( <b>b</b> ) 0%-10%), obtained from MC HIJING simulations, after <i>wing</i> corrections. . . . .	108
4.12 (Color online) 1-D $\Delta\eta$ projections of the correlation function at $\Delta\phi = \pi \pm 0.25$ (red) and $\Delta\phi = \pi/2 \pm 0.25$ (black) in different $p_{T,trig}$ , $p_{T,asso}$ , and centrality classes, obtained from data at 2.76 TeV Pb-Pb collisions, ( <b>a</b> ) before <i>wing</i> corrections and ( <b>b</b> ) after <i>wing</i> corrections. . . . .	108
4.13 (Color online) Steps of closure test: ( <b>a</b> ) 2-D correlation at generator level, ( <b>b</b> ) 2-D correlation at reconstruction level but corrected for detector in-efficiencies and ( <b>c</b> ) ratio $\frac{\text{corrected reconstructed}(\mathbf{b})}{MC\ generated(\mathbf{a})}$ . The ratio is found to be at unity except at large $\Delta\eta$ . . . . .	110
4.14 (Color online) <b>a</b> ) 2D $C(\Delta\eta, \Delta\phi)$ correlation function <b>b</b> ) projections on $\Delta\phi$ for $ \Delta\eta  < 1$ (red) and $ \Delta\eta  > 1$ (black); <b>c</b> ) subtracted near side per-trigger-particle jet like yield . . . . .	111
4.15 (Color online) 1-D $\Delta\phi$ correlation function fitted with ( <b>top</b> ) double Gaussian and ( <b>bottom</b> ) generalized Gaussian. Respective $\chi^2/ndf$ values are also mentioned in the figures . . . . .	113
4.16 (Color online) Two-dimensional (2-D) per-trigger-particle yield of associated charged hadrons are shown as function of $\Delta\eta$ and $\Delta\phi$ for $2.5 < p_{T,trig} < 5$ GeV/c and $1.8 < p_{T,asso} < 5$ GeV/c, for 0%-10% most central Pb–Pb collisions at 2.76 TeV. <b>a</b> ) The near-side region is zoomed-in, <b>b</b> ) after $\eta$ -gap subtraction, <b>c</b> ) projection of the same on $\Delta\phi$ for $ \Delta\eta  < 1$ . . . . .	114
4.17 (Color online) Two-dimensional (2D) per-trigger-particle yield of associated charged hadrons are shown as function of $\Delta\eta$ and $\Delta\phi$ for $6 < p_{T,trig} < 12$ GeV/c and $1.8 < p_{T,asso} < 5$ GeV/c, for 0%-10% most central Pb–Pb collisions at 2.76 TeV. <b>a</b> ) The near-side region is zoomed-in, <b>b</b> ) after $\eta$ -gap subtraction, <b>c</b> ) projection of the same for $ \Delta\eta  < 1$ . . . . .	115

4.18 (Color online) Two-dimensional (2-D) flow-subtracted per-trigger-particle associated yield of charged hadrons as a function of $\Delta\eta$ and $\Delta\phi$ for $2.5 < p_{T,trig} < 5$ GeV/c and $1.8 < p_{T,trig} < 5$ GeV/c, in (a) 0%-10% , (b) 20%-40% and (c) 60%-90% centrality classes of Pb-Pb collisions at 2.76 TeV. Near side zoomed-in for better clarity . . . . .	116
4.19 (Color online) Two-dimensional (2-D) flow-subtracted per-trigger-particle associated yield of charged hadrons as a function of $\Delta\eta$ and $\Delta\phi$ for $6 < p_{T,trig} < 12$ GeV/c and $1.8 < p_{T,trig} < 5$ GeV/c, in (a) 0%-10% , (b) 20%-40% and (c) 60%-90% centrality classes of Pb-Pb collisions at 2.76 TeV. . . . .	117
4.20 (Color online) 1-D $\Delta\phi$ correlation (a): for $2.5 < p_{T,trig} < 6$ GeV/c and $1.8 < p_{T,trig} < 5$ GeV/c, and, (b):for $6 < p_{T,trig} < 12$ GeV/c and $1.8 < p_{T,trig} < 5$ GeV/c, in 0%-10%, 20%-40% and 60%-90% centrality classes of Pb-Pb collisions at 2.76 TeV. . . . .	117
4.21 (Color online) Per-trigger-particle associated yields of charged hadrons as a function of $\Delta\phi$ <b>Top</b> :for $6 < p_{T,trig} < 12$ GeV/c and $1.5 < p_{T,asso} < 3$ GeV/c , and, <b>Bottom</b> :for $6 < p_{T,trig} < 12$ GeV/c and $3 < p_{T,asso} < 6$ GeV/c are shown for 4 centrality event class of Pb-Pb collisions at 2.76 TeV. For reference, results from most peripheral 60%-90% event classes are superimposed. . . . .	118
4.22 (Color online) Per-trigger-particle associated yields of charged hadrons as a function of $\Delta\phi$ <b>Top</b> :for $3 < p_{T,trig} < 6$ GeV/c and $1.8 < p_{T,asso} < 5$ GeV/c , and, <b>Bottom</b> :for $3 < p_{T,trig} < 6$ GeV/c and $2.75 < p_{T,asso} < 5$ GeV/c are shown for 4 centrality event class of Pb-Pb collisions at 2.76 TeV. For reference, results from most peripheral 60%-90% event classes are superimposed. . . . .	119
4.23 (Color online) Integrated per-trigger-particle near side jetlike yield, for $6 < p_{T,trig} < 12$ GeV/c and $p_{T,asso}$ intervals of (a) $1.5 < p_{T,asso} < 3.0$ GeV/c and (b) $3.0 < p_{T,asso} < 6.0$ GeV/c are shown as a function of $N_{part}$ in Pb–Pb collisions at 2.76 TeV. Yield calculated from double Gaussian and generalized Gaussian fit to 1D $\Delta\phi$ correlation functions are also shown in different markers . . . . .	120
4.24 (Color online) Integrated per-trigger-particle near side jet-like yield, for $3 < p_{T,trig} < 6$ GeV/c and two different intervals of $p_{T,asso}$ are shown as a function of $N_{part}$ in Pb–Pb collisions at 2.76 TeV. Per-trigger yield for the $p_{T,asso}$ interval 2.75-5.0 GeV/c is scaled for better display . . . . .	122

5.1	(Color online) The combined PID signal of TPC-TOF is shown in 2-D plots for the $p_T$ range of ( <b>top</b> ) $1.5 < p_T < 1.75$ GeV/c and ( <b>bottom</b> ) $2.5 < p_T < 3.0$ GeV/c. The PID signals are expressed in terms of the number-of-standard deviation ( $n\sigma$ ) from the expected response for pions in each detector . . . . .	130
5.2	(Color online) The separation power $S_\sigma$ as a function of $p_T$ : ( <b>top panels</b> ) for TPC and ( <b>bottom panels</b> ) for TOF. Results are shown for Pb-Pb collisions, averaging over all centrality classes between 0%-90%. Since the detector responses could be track-length dependent, separation power is also calculated in a small $\eta$ -interval. The red and black lines represent separation power in $ \eta  < 0.5$ and $0.8$ , respectively . . . . .	131
5.3	(Color online) The $n\sigma_{PID}$ distributions for pions as function of $p_T$ ( <b>top panel</b> ) and its projections in different $p_T$ bins ( <b>bottom panel</b> ), before PID cuts. . . . .	133
5.4	(Color online) The $n\sigma_{PID}$ distributions for pions as function of $p_T$ ( <b>top panel</b> ) and its projections in different $p_T$ bins ( <b>bottom panel</b> ), after PID cuts. . . . .	133
5.5	(Color online) The PID efficiency matrix for ( <b>a</b> ) $2.0 < p_T < 2.5$ GeV/c and ( <b>b</b> ) $3.5 < p_T < 4.0$ GeV/c . . . . .	135
5.6	(Color online) Identification efficiency or the weight factor obtained from Eq. 5.9 as a function of $p_T$ for ( <b>Left</b> ) $\pi$ and ( <b>Right</b> ) $p/\bar{p}$ in different intervals of centrality. . . . .	137
5.7	(Color online) Weight factors in Eq. 5.9 for different particle species in different intervals of $\eta$ are presented as a function of $p_T$ ( <b>a</b> ). The ratio of the weight factors between central (0%-10%) and peripheral (60%-90%) are shown in ( <b>b</b> ). . . . .	138
5.8	(Color online) Two-dimensional $\Delta\eta, \Delta\phi$ correlation functions for pion triggers for different centrality classes of Pb-Pb at 200 GeV. All trigger and associated charged hadrons are selected in the respective $p_T$ ranges $2.5 < p_{T,trig} < 5$ GeV/c and $1.8 < p_{T,asso} < 5$ GeV/c. The z-axis for all plots in this figure represent associated per-trigger yield expressed by $\frac{1}{N_{trig}} \frac{d^2 N_{asso}}{d\Delta\eta d\Delta\phi} (rad^{-1})$ . . . . .	139
5.9	(Color online) Two-dimensional $\Delta\eta, \Delta\phi$ correlation functions for proton triggers for different centrality classes of Pb-Pb at 200 GeV. All trigger and associated charged hadrons are selected in the respective $p_T$ ranges $2.5 < p_{T,trig} < 5$ GeV/c and $1.8 < p_{T,asso} < 5$ GeV/c. The z-axis for all plots in this figure represent associated per-trigger yield expressed by $\frac{1}{N_{trig}} \frac{d^2 N_{asso}}{d\Delta\eta d\Delta\phi} (rad^{-1})$ . . .	140

5.10	(Color online) The dip region in $(\Delta\eta, \Delta\phi)$ for proton-hadron correlations in 10-20% central Pb-Pb collisions at 2.76 TeV for four charge combinations of trigger and associated particles : <b>(a)</b> (trig , assoc ) = (+, -), <b>(b)</b> (trig , assoc ) = (+, +), <b>(c)</b> (trig , assoc ) = (-, +), and <b>(d)</b> (trig , assoc ) = (-, -). . . . .	142
5.11	(Color online) The $\Delta\eta$ projection of unsubtracted 2-D correlation function, showing comparison of dip structure on the near side peak region after correcting for the two-track resolution effects in three different ranges of radial distances . . . . .	143
5.12	(Color online) The $\Delta\eta$ projection of unsubtracted 2-D correlation function, showing comparison of dip structure on the near side peak region for different magnitudes of two-track resolution cuts . . . . .	144
5.13	(Color online) Associated yields per trigger proton as a function of $\Delta\phi$ and $\Delta\eta$ for 10%-20% most central events in trigger and associated $p_T$ ranges of $2 < p_{T,trig} < 5$ GeV/c and $1 < p_{T,asso} < 4$ GeV/c, respectively are shown for 3 MC models. <b>(a)</b> : EPOS 3.107 with hadronic rescattering, <b>(b)</b> : AMPT string melting (AMPT SM) with hadronic rescattering, <b>(c)</b> : HIJING, only jets and minijets. The combinatorial and flow backgrounds are not subtracted . . . . .	145
5.14	(Color online) Illustration of the fitting procedure for the 0-10% most central PbPb collisions $\sqrt{s_{NN}} = 2.76$ TeV for pion triggered correlations in $2.5 < p_{T,trig} < 5.0$ GeV/c and $1.8 < p_{T,asso} < 5.0$ GeV/c: <b>(a)</b> the 2-D $\Delta\eta$ and $\Delta\phi$ distributions of associated particles per-trigger yield, <b>(b)</b> the 2-D fit of the near side region, <b>(c)</b> the signal peak component from the fit by Eq. 5.10 and <b>(d)</b> the difference between the data and the fit. The z-axis for all plots in this figure represent associated per-trigger yield expressed by $\frac{1}{N_{trig}} \frac{d^2 N_{asso}}{d\Delta\eta d\Delta\phi} (rad^{-1})$ . . . . .	147
5.15	(Color online) Illustration of the fitting procedure for the 0-10% most central PbPb collisions $\sqrt{s_{NN}} = 2.76$ TeV for proton triggered correlations in $2.5 < p_{T,trig} < 5.0$ GeV/c and $1.8 < p_{T,asso} < 5.0$ GeV/c: <b>(a)</b> the 2-D $\Delta\eta$ and $\Delta\phi$ distributions of associated particles per-trigger yield, <b>(b)</b> the 2-D fit of the near side region, <b>(c)</b> the signal peak component from the fit by Eq. 5.10 and <b>(d)</b> the difference between the data and the fit. The z-axis for all plots in this figure represent associated per-trigger yield expressed by $\frac{1}{N_{trig}} \frac{d^2 N_{asso}}{d\Delta\eta d\Delta\phi} (rad^{-1})$ . . . . .	147
5.16	(Color online) $\chi^2/Ndf$ of the 2-D fit to the correlation functions for pion and proton triggered correlations for all centrality classes of Pb-Pb collision at 2.76 TeV . . . . .	148

5.17 (Color online) The dip on the near side peak of proton triggered correlation is zoomed in. . . . .	149
5.18 (Color online) The centrality dependence of yield in the depletion region with respect to the overall peak yield calculated from the 2-D fit. Vertical lines indicate systematic errors associated with the variation of the size of the exclusion region. . . . .	149
5.19 (Color online) The near side per-trigger yield of associated charged hadrons triggered by pions (blue) and protons (red) in $2.5 < p_{T,trig} < 5.0$ GeV/c and $1.8 < p_{T,asso} < 5.0$ GeV/c as function of $N_{part}$ for Pb-Pb collisions at 2.76 TeV. Error bars on the yield are statistical only . . . . .	150
5.20 (Color online) The near side yields per trigger for baryon (squares) and meson (circles) triggers with associated mesons. Triggers have $2.5 < p_{T,trig} < 4.0$ GeV/c and associated particles have $1.8 < p_{T,asso} < 2.5$ GeV/c. The error bars are the statistical errors and the boxes show the systematic errors. There is an additional 13.6% normalization error [11]. . . . .	152
5.21 (Color online) The ratio of the per-trigger jet-like yield of protons to that of the pions are shown as function of collision centrality, characterized by $N_{part}$ . The blue triangle and green dashed line represent comparison with AMPT-SM and EPOS MC event generators, respectively. Error bars are statistical and the boxes denote the systematic uncertainty primarily due to the loss of small angle correlated pairs in the depletion region for proton triggered correlations. . . . .	155
5.22 (Color Online) <b>Left:</b> Photograph of graphite coated RPC module, <b>Middle:</b> Button and side spacers, <b>Right:</b> Photograph of RPC module with pick-up panel used for signal extraction . . .	iii
5.23 (Color online) Variation of surface and bulk resistivities as a function of applied voltage. . . . .	iii
5.24 (Color Online) RPC performance, <b>Left:</b> Efficiency as a function of applied voltage, <b>Right:</b> Plot showing spatial efficiency distribution. Different locations where efficiency values were measured are highlighted in red color (not upto the scale). . . . .	iv

# List of Tables

4.1	Summary of hybrid track cuts . . . . .	98
5.1	Summary of cut values . . . . .	132

# Chapter 1

## Introduction

“The success of *A Brief History* indicates that there is a widespread interest in the big questions like: where did we come from ? And why is the universe the way it is” – *Stephan Hawking* [1]

Where did we come from ? This is indeed a big question ! The answer, as has been agreed upon almost universally: we came from one explosive event 13.7 billion years ago – **The Big Bang** [2].

Corroborated by Edwin Hubble’s first observational evidence on the red-shift of light from distant galaxies, Georges Lemaître’s “**Big Bang theory of universe**” was accredited as the first conceptually formulated idea of the cosmological origin of the universe [3, 4].

To our current understanding, an incredibly hot and dense baby universe, popped-out of this explosion, was expanding and cooling rapidly. In the course of expansion, it went through sequences of cosmological phase transitions that mark some of the important epochs of the expanding early universe[5], pictorially shown in Fig 5.23. Approximately  $10^{-10}$ s after the Big Bang, universe entered a cosmic phase of quarks and gluons, that had lasted upto a few microseconds. At that exceptionally high temperature, all matter had existed as

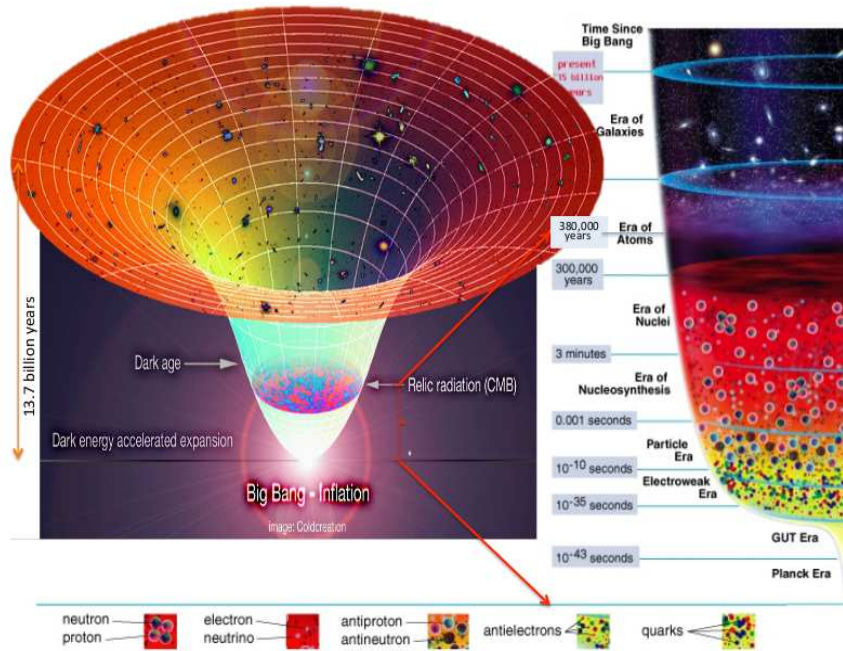


Figure 1.1: (Color online) A pictorial depiction on the chronological evolution of the universe after the Big Bang

a weakly interacting soup of quarks, gluons and other elementary particles. Around  $10 \mu\text{s}$  after the explosion, when the temperature of the universe was cooled down to  $10^{12}\text{K}$  or  $200 \text{ MeV}$  [6], another phase transition took place that had resulted in the confinement of quarks and gluons into baryons and mesons (hadrons)- the building blocks of our present universe.

It is understood that the hierarchical levels in the microscopic structure of macroscopic objects has a unique resemblance with the consecutive stages of evolution that universe had undergone. Thus several efforts were made to enrich our microscopic understanding of the matter beyond the level of the ordinary atomic systems.

Towards the end of  $20^{\text{th}}$  century (1980 to be specific), an extensive work by Edward Shuryak [7] had shown that it would be possible to probe the fundamental constituents of matter by subjecting it to an ultra high temperature or

energy density. It was perceived that such extreme conditions could be achieved and made accessible for experimental investigations by colliding two heavy nuclei at ultra-relativistic energies. However, the task was daunting and indeed challenging.

But, the outstanding collaborative effort of the scientific communities across the globe, paved the way towards the establishment of two most powerful accelerators: The Relativistic Heavy Ion Collider (RHIC) at Brookhaven National Laboratory (BNL) in New York and Large Hadron Collider (LHC) at the Conseil Européen pour la Recherche Nucléaire (CERN) in Geneva. Both these facilities were aimed to recreate those elusive moments from few microseconds after the Big Bang, by colliding stable nuclei at relativistic energies in the terrestrial laboratories.

As conjectured, by smashing nuclei at unprecedented energies at RHIC and LHC, it would be possible to excite the ordinary hadronic matter into a new phase of *locally equilibrated system of de-confined state of quarks and gluons*, a reminiscent of the primordial universe following the Big Bang. The phrase Quark-Gluon Plasma (QGP) was coined for the first time to describe this newly formed matter comprising quarks and gluons as fundamental degrees of freedom.

The study of QGP was of great interest not only because of its cosmic-connection, but it also rendered a platform to test some of the intriguing aspects of Quantum Chromodynamics- the Standard Model (SM) theory of the strongly interacting quarks and gluons [8, 9, 10, 11].

## 1.1 The Standard Model

The Standard Model (SM) in particle physics is an elementary and experimentally-tested theoretical framework that describe interactions among the fundamental

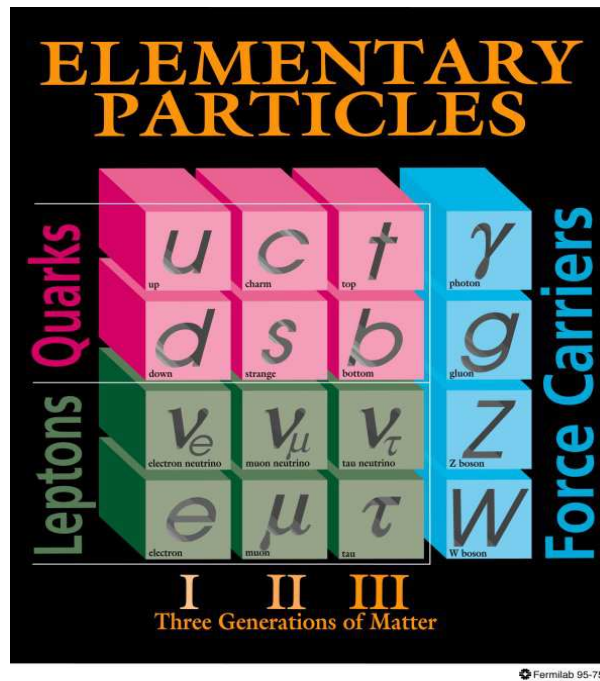


Figure 1.2: (Color online) Three generations of the Standard Model elementary particles and the quanta of their fundamental interactions

particles and force-carriers. As per the SM, the fundamental constituents of matter are a bunch of elementary particles which are supposed to be indivisible. Hitherto, these basic particles are classified into two groups- “quarks” and “leptons”. The leptons along with their respective associated neutrinos and quarks are further categorized into 3 generations. The 1<sup>st</sup> generation of quark and lepton pairs are the lightest and most stable fundamental particles that build-up all objects that we experience in our every-day life.

Four basic interactions between these fundamental particles have also been identified, called as strong, weak, electromagnetic and gravitation. Leaving aside gravity, rest of the three interactions are mediated by spin 1 particles called gauge bosons. For example, the strong force which is responsible for binding quarks within the hadrons is mediated by gluons. Photons are the carrier for the electromagnetic forces and weak interactions are represented by massive  $W^\pm$  (80 GeV) and  $Z^0$  (91 GeV) vector bosons. However, the SM has

remained skeptical about the gravitational interactions as streamlining gravity into this framework could not be achieved because of the lack of well-tested evidence of hypothetical gravitons - a conjectured mediator for the gravitational interactions.

Although it is popularly known as a “model”, in reality, it is a collection of well-tested theories that could describe phenomena from the microscopic scale of quarks and leptons to the large scale of present-day universe using the Quantum Electrodynamics (QED), the Electro-Weak theory postulated by Glashow, Weinberg and Salam and the Quantum Chromodynamics (QCD). While QED is the theory for the electromagnetic interactions, weak interactions are described by Electro-Weak theory and the fundamental theory of strong interactions is QCD.

## 1.2 The Quantum Chromodynamics

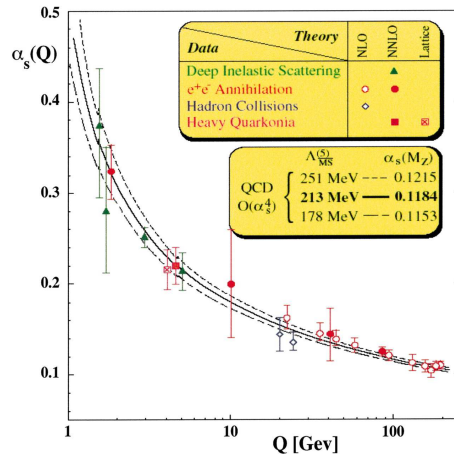


Figure 1.3: (Color online) The strong coupling constant  $\alpha_s$  as a function of the momentum transfer  $Q$ . A manifestation of *asymptotic freedom*.

Quantum chromodynamics, familiar as QCD, is a universally accepted theory of the strong interaction that offers precise understanding of the microscopic structures and interactions of the hadronic matter. According to QCD, hadrons

are composed of elementary quarks and gluons that participate in strong interactions by virtue of their color charges. The color charges are analogous to the electrical charges in Quantum Electrodynamics (QED). Unlike electrical charge, which is a scalar quantity, color charge in QCD is a quantized vector quantity that has three possible states in a complex vector space termed as: Red, Blue and Green. The net-color charge of the constituent quarks in a hadron must cancel out vectorially owing to the confining property of the strong interactions that only allow color-singlet states to exist in nature freely.

One of the intriguing features of QCD is the *asymptotic freedom* [12] which states that strength of interaction between quarks weakens as the distance between them get shorter. For this discovery Politzer, Wilzek and Gross was awarded Noble Prize in 2004. This phenomenon can be naively explained from the momentum transfer ( $Q$ ) dependence of the strong coupling constant  $\alpha_s(Q^2)$  as shown in Eqn. 1.1.

$$\alpha_s(Q^2) = \frac{12\pi}{(33 - 2n_f)\ln(Q^2/\Lambda_{QCD}^2)} \quad (1.1)$$

Where  $n_f$  is the number of flavors (6) in the QCD and,  $\Lambda_{QCD}$  is the so-called “QCD scale” with a typical value of  $\approx 200$  MeV. In limit of large momentum transfer, the effective coupling between the quarks decreases, as a result the interaction strength becomes so weak that they almost behave like quasi-free particles. This is familiarly called *asymptotic freedom*. Because of this property, in the limit of high-momentum transfer, physics of strong interactions can be reliably calculated under the perturbative approximations.

Fig.1.3 shows the experimental measurements of the strong coupling constant,  $\alpha_s$ , as function of momentum transfer ( $Q$ ) from various scattering processes. Also shown the expectations from the QCD theoretical calculations.

Another remarkable property of the QCD particularly in the domain of

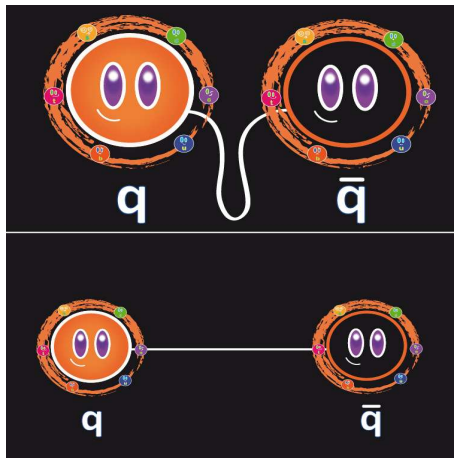


Figure 1.4: (Color online) An artist's impression when quark-(anti)quark pair is stretched, representing the increase in static quark-(anti)quark potential

low energy or small momentum transfer is the color *confinement*. It states that at a distance larger than the scale of  $1/\Lambda_{QCD}$ , any strongly interacting system should be color neutral. Where  $\Lambda_{QCD}$  is a dynamically generated scale parameter portraying the limit of confinement. Comparing QCD calculations with the experimental results the value  $\Lambda_{QCD}$  was found to be  $\sim 200$  MeV or 1fm approximately similar to the hadronic length scale. As a consequence of this *confinement* property isolated free quarks does not exist in nature rather they are strongly bounded within the hadronic dimensions. The color *confinement* is a theoretical conjecture in QCD corroborated by the experimental facts but till date it could not be proven analytically. However, numerical simulations based on lattice-QCD suggest that the linear increase ( $\sim Kr$ ) in static quark-anti-quark potential from distances larger than a few fermi is consistent with the property of *confinement* beyond the scale of hadronic dimensions.

### 1.3 QCD Phase structure

The idea of the *asymptotic freedom* led to the establishment of the fact that a deconfined state of quarks and gluons could be achieved when normal nuclear

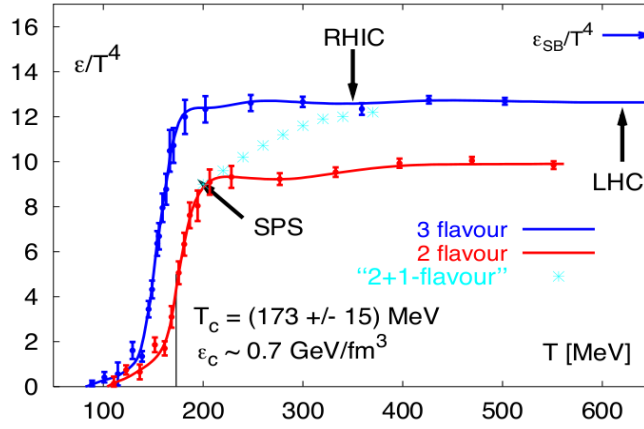


Figure 1.5: (Color online) Lattice QCD prediction on the temperature dependence of energy density of QCD medium, showing an abrupt change in the energy density below and above a critical temperature ( $T_c$ ) - an evidence of phase change [13].

matter is subjected to high temperature or pressure. Lattice QCD calculations clearly show that on increasing the energy density of the medium, system undergoes a sharp transition beyond a threshold or critical temperature  $T_c$ . Fig.1.5 shows the transverse energy density as a function of the temperature, obtained from lattice-QCD calculations for 3, 2 and 2+1 light quark flavors, and zero baryo-chemical potential [14, 15]. Here 2+1 refers to two light quarks and one heavy quark. The energy density of a system of ideal, relativistic parton gas scale with the fourth power of the temperature as  $\varepsilon = gT^4$ , where  $g$  represents the number of degrees of freedom. The quantity  $\varepsilon/T^4$  or  $g$  is seen to rise steeply when the temperature  $T$  approaches a critical temperature  $T_c$  around  $173 \pm 15$  MeV. This sharp transition demonstrates the change in number of effective degrees of freedom below and above  $T_c$ - a manifestly evident signature of phase transitions. The latest lattice QCD calculations [24, 25] predict that hadronic to QGP transition may occur around a  $T_c$  value of  $154 \pm 9$  MeV [26]. However, due to color *confinement*, the deconfined state of quarks and gluons would eventually undergo a reverse phase transition to a system of ordinary hadrons.

Different phases of the QCD matter can be explored in a hypothetical diagram called the **QCD phase diagram**. It shows the theoretically predicted values of temperature, ( $T$ ) and the baryon chemical potential, ( $\mu_B$ ), at which a phase transition from the ordinary hadronic matter to a deconfined QGP phase might take place. As can be seen from the left panel of the Fig. 1.6, at vanishingly small net-baryon densities ( $\mu_B \approx 0$ ), recent calculations predict a cross-over phase transition within a temperature range of  $T_c \approx 150$ -170 MeV. At LHC, a predicted cross-over phase transition is likely to occur around 160 MeV. Whereas, at finite  $\mu_B$ , although the theory has large uncertainty, the phase transition is most likely to be of the first-order. In addition, there is a conjectured QCD *critical end point* (CEP) that marks the end of first-order phase transition and the onset of the cross-over region. Depending on the temperature and density, QGP may exist in different forms. At temperatures and densities close to QCD chiral phase transitions ( $T_c$ ), QGP exhibit properties of a strongly interacting nearly perfect liquid and, at high net-baryon densities it may form a color superconducting plasma that might exist deep inside the neutron stars.

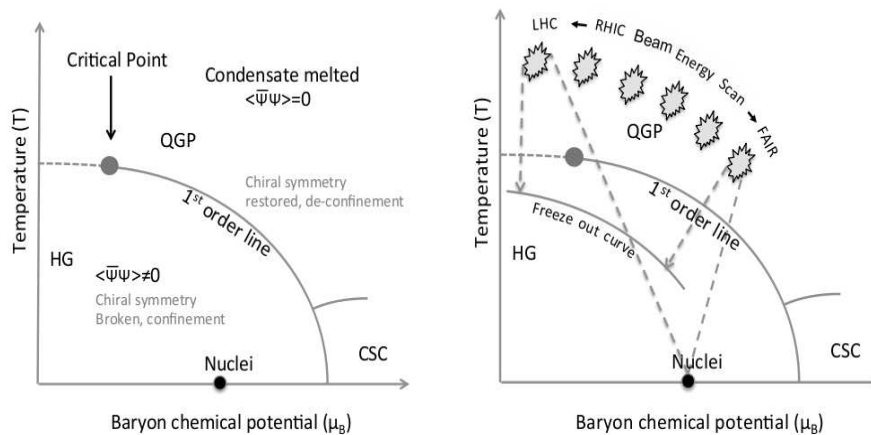


Figure 1.6: (Color online) **Left panel:** Phase diagram in  $T$ - $\mu_B$  space as conjectured by the Lattice QCD. **Right Panel:**  $T$ - $\mu_B$  coordinate space representations of heavy-ion collisions at RHIC-BES, LHC and FAIR.

A lot of theoretical and experimental efforts have been made and many are the in pipe-line to explore phase structure (in  $T - \mu_B$  space) of nuclear matter and locate various regions of interest as mentioned above. If broadly classified, there exist two extremes in the phase diagram of the nuclear matter, high temperature and high density. The top-RHIC and LHC energies probe the high temperature limit. On the other hand, SPS, AGS, lower energies in Beam Energy Scan program at RHIC and the upcoming facilities like FAIR and NICA are likely to scan the phase diagram in the region of high net-baryon densities (right panel of Fig.1.6).

## 1.4 Heavy Ion Collisions at Relativistic Energy

### 1.4.1 Probing the Quark Gluon Plasma

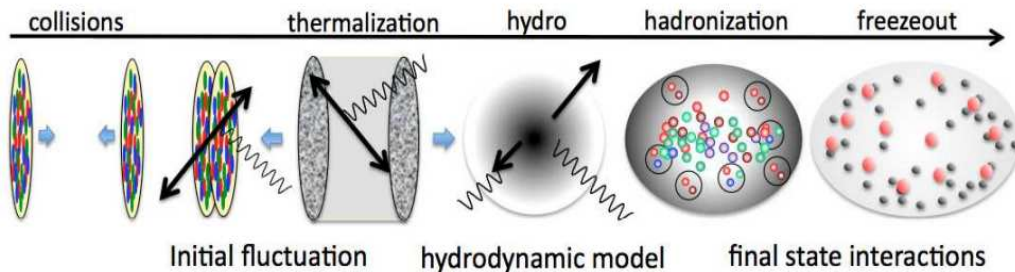


Figure 1.7: (Color online) A schematic representation of different stages of a heavy ion collision [16].

The search for QGP was initiated almost 30 years ago with Au-ion beam at 1 GeV/nucleon at the Bevalac in Berkeley National Lab, USA. Soon it was followed by series of experiments at the Alternate Gradient Synchrotron (AGS) at BNL, USA and Super Proton Synchrotron (SPS) at CERN, Geneva. Results from several experiments (NA44, NA45, NA49, NA50, NA52, WA98, etc) at CERNs' SPS have helped to form a general consensus on the creation of a new state of matter with quarks and gluons as pertinent degrees of freedom at the

top-SPS energy.

In the year 2000, the Relativistic Heavy Ion Collider (RHIC), a dedicated facility for QGP search became operational. RHIC is a collider facility and the major advantage of colliders over fixed-target collisions is the large gain in center-of-mass energy available for particle production. Data collected by the four experiments (BRAHMS, PHENIX, PHOBOS and STAR) for Au-Au collisions at top-RHIC energy provided compelling evidence on the formation of new a state of matter of very high gluon density. The medium formed at RHIC was further charecterized as a strongly interacting quark-gluon plasma (s-QGP) [17, 18, 20, 19].

About 10 times increase in center-of-mass energy was achieved when Pb-nuclei were smashed against each other at 2.76 TeV/A at CERNs' Large Hadron Collider in year of 2008. At LHC, ALICE is a dedicated experiment for QGP search whereas, the ATLAS and CMS are general purpose detectors equipped sufficiently to carry out excellent research on QGP.

Understanding the spatial and temporal evolution of the system created in heavy ion collisions offers an unique way to probe the underlying dynamics of normal nuclear matter when subjected to extreme conditions. When two Lorentz contracted heavy ions collide, energy carried by the incoming nucleons are concentrated in a small region of space in short time span. Using the Bjorken prescription, initial spatial energy density can be estimated using the following relation:

$$\varepsilon_{Bj}(\tau_0) = \frac{1}{A_{trans}} \frac{dE_T}{\tau_0 dy} \tag{1.2}$$

where  $A_{trans}$  is the transverse area of the over-lapped geometry of the incident nuclei and  $\frac{dE_T}{dy}$  denotes the transverse energy of the final state particles per unit of rapidity. At SPS, initial transverse energy density( $\varepsilon$ ) was estimated to be  $\sim$

$3.0 \pm 0.6 \text{ GeV}/\text{fm}^3$  using a conservative approximation of  $\tau_0 = 1 \text{ fm}/c$ . This is certainly in excess to the lattice-QCD predicted critical energy density ( $\varepsilon(\tau_0)$ ) of  $1 \text{ GeV}/\text{fm}^3$  required for deconfinement of quarks and gluons. Adhering to the similar formalism,  $\varepsilon(\tau_0)$  was estimated to be  $6.0 \pm 1.0$  and  $14 \pm 1.0 \text{ GeV}/\text{fm}^3$  for Au-Au at  $\sqrt{s_{NN}} = 200 \text{ GeV}$  and Pb-Pb at  $\sqrt{s_{NN}} = 2.76 \text{ TeV}$  at RHIC and LHC respectively [21]. From these estimations it would suffice to claim that the matter created have enormously high energy density and temperature, sufficient to form a baryon-free QGP.

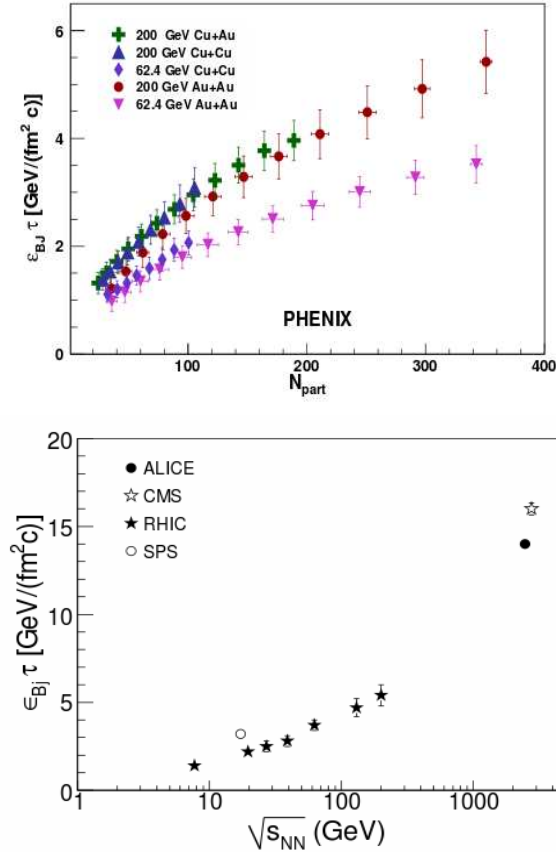


Figure 1.8: (Color online) **Top:**  $\sqrt{s_{NN}}$  dependence of Bjorken energy density ( $\varepsilon_{Bj}$ ) for Au-Au, Cu-Au, and Cu-Cu collisions at  $\sqrt{s_{NN}} = 200$  and  $62.4 \text{ GeV}$  [22]. **Bottom:** The values of Bjorken energy density are shown for Pb-Pb collisions at LHC energy, together with energies available for Au-Au collisions at RHIC [23].

The hot and dense quark-gluon plasma may not be in equilibrium at the initial stages of collision. But through subsequent interactions a local thermal equilibration might be achieved and thereafter system may be governed by the laws of thermodynamics. As the system expands and cools down to a critical temperature  $T_C = 150\text{-}160$  MeV, a transition occurs from a partonic to hadronic phase. Soon after the hadronization, system achieves a state of hadro-chemical equilibrium at the chemical freeze-out temperature,  $T_{ch}$ , in the immediate vicinity of quark-hadron phase transition temperature ( $T_C$ ) [27, 28]. At this point, all in-elastic interactions between the constituents of the system ceases and the relative abundances of different particle species are frozen [29, 27, 30]. However, resonance rescatterings and elastic interactions may still continue until the temperature of the system drops below the kinetic freeze-out temperature,  $T_{kin}$ . It was observed that kinetic freeze-out occurs at temperatures as low as 80-100 MeV [31]. Until then, the momentum distributions of the particles may be significantly modified, predominantly due to elastic scatterings and build-up of hadronic radial flow. After the kinetic freeze-out, mean free path of the system becomes larger than the scale of strong interactions causing hadrons to decouple from the medium and stream freely to the detectors.

As the short lived plasma could not be detected directly, these final state particles could be used to probe various stages of collision.

- **The Collective Dynamics:** At RHIC, the collective emission of final state particles has immensely contributed towards characterizing the hot and dense medium [32, 33]. Detailed measurements of the observables associated with the collective emission of the particles had provided indispensable information about the evolution and transport properties of the medium. Experimentally, a part of the associated measurements are represented by the magnitudes of coefficients in the Fourier expansion of

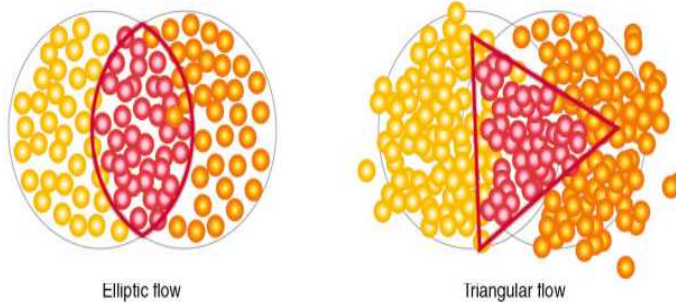


Figure 1.9: (Color online) A schematic representation of nucleon profile in an asymmetric heavy ion collision. Also highlighted dominant initial anisotropy-elliptic(**left**) and triangular (**right**)

the azimuthal ( $\phi$ ) distributions of the emitted particles when measured with respect to the reaction plane ( $\psi_R$ ). This is generally expressed as:

$$E \frac{d^3N}{dp^3} = \frac{1}{2\pi} \frac{d^2N}{p_T dp_T dy} \left( 1 + \sum_1^n 2v_n \cos(n(\phi - \psi_R)) \right) \quad (1.3)$$

The second harmonic coefficient in the expansion,  $v_2 = \langle \langle \cos(2(\phi - \psi_R)) \rangle \rangle$ , known as elliptic flow, plays a pivotal role in characterizing the matter formed in the ultra-relativistic heavy ion collisions [34, 35]. In fact this quantity was found to be sensitive to the equation of state (EoS) of the matter [36]. Results have shown that almost 50% increase in the elliptic flow coefficient ( $v_2$ ) has been observed at RHIC compared to that at the SPS [37]. The large elliptic flow at RHIC was shown to have reasonably described by the hydrodynamical calculations with a EoS that has a 1<sup>st</sup> order phase transition to QGP [38].

As per interpretations, the large elliptic anisotropy in non-central collisions results from the difference in the hydrodynamic pressure gradient developed in a thermally equilibrated but spatially anisotropic overlap region in the collision zone [39, 40, 41, 42, 43]. It is therefore understood that the initial spatial-anisotropy in a plane transverse to the direction of the colliding nuclei is transformed into a final state azimuthal momentum

anisotropy of the particles via partonic and hadronic interactions.

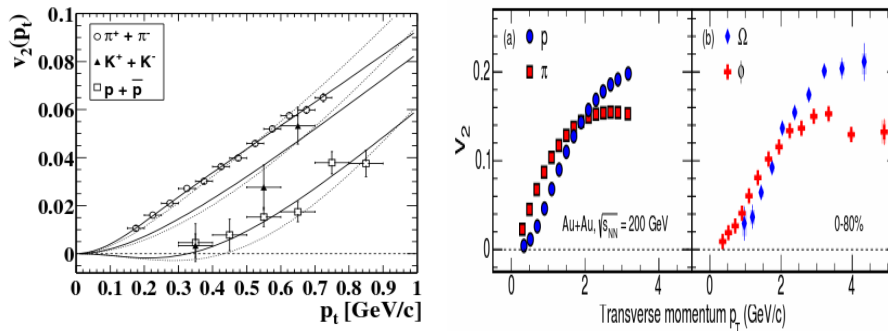


Figure 1.10: (Color online) The mass and baryon-meson ordering of  $v_2(p_T)$  of identified particles at low and intermediate  $p_T$ : **(left)** Au-Au  $\sqrt{s_{NN}} = 130$  GeV [44]. **(right)** Au-Au  $\sqrt{s_{NN}} = 200$  GeV [45]. The Solid lines on the figure in the left panel show the predictions from hydrodynamic calculations

First results from RHIC have shown that the elliptic flow coefficient,  $v_2$ , of identified particles when measured as a function of  $p_T$  exhibit a characteristic mass ordering [33, 44] for  $p_T < 1$  GeV/c, i.e,  $v_2^\pi(p_T) > v_2^K(p_T) > v_2^p(p_T)$ . As shown in the left panel of Fig. 1.10, the  $v_2(p_T)$  values of  $\pi, k$  and  $p/\bar{p}$  are ordered according to their masses in a decreasing order. This particle mass dependent flow pattern was interpreted as a consequence of interplay between radial and anisotropic flow predicted by hydrodynamical calculations [42]. The mass hierarchy in  $v_2$  is believed to have induced by a thermal pressure gradient, that generates a radially symmetric collective flow field ( $v^{radial}$ ) in an expanding thermalized medium. As a result, particles gain an additional momentum ( $p_T^{tot} = p_T^{intrinsic} + \gamma\beta v^{radial}$ ) and boosted to higher values of  $p_T$ . This causes a mass dependent depletion in the low- $p_T$  region of the spectra, but, compensated by the increase at the intermediate- $p_T$ . The large radial flow results in a stronger decrease of elliptic flow at low  $p_T$  ( $< 2$  GeV/c), and the effect is seen to be more pronounced for heavy particles, for example protons [46].

But, at the intermediate- $p_T$  region,  $2 < p_T < 5$  GeV/c, this mass ordering

is broken and  $v_2$  of baryons saturates at a larger value than mesons, as shown in the right panel of Fig.1.10. The observed baryon-meson splitting of identified particles  $v_2(p_T)$  at RHIC was found to be compatible with the models invoking hadronization of a collectively expanding partonic medium via a mechanism of quark recombination or coalescence [86]. This was further supported by the observation of constituent quark number scaling (NCQ) of hadron  $v_2(p_T)$ , providing a strong indication towards the onset of the partonic collectivity and the dominance of quark degrees of freedom at the time of hadronization. However, recent results from ALICE have revealed deviations from the NCQ scaling at the level of  $\pm 20\%$  for  $p_T > 3$  GeV/c. In addition,  $\phi$ -meson  $v_2$ , shown in Fig.1.11, at the intermediate  $p_T$  region is shifted towards the baryon band rather than following the mesons. These observations led to a possible interpretation of baryon-meson ordering of  $v_2$  as an effect of mass of the particles than that of the constituent quark number [46]. Since the magnitude of radial flow and the  $p_T$ -integrated values of  $v_2$  were shown to have increased by same amount (20-25%) at LHC than that of the RHIC, the significance of mass over quark number in  $p_T$ -differential  $v_2$  seems to be plausible.

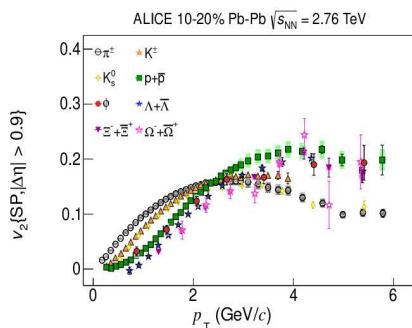


Figure 1.11: (Color online) The  $v_2(p_T)$  of identified particles showing mass and baryon-meson ordering at low and intermediate  $p_T$  of Pb-Pb collisions at  $\sqrt{s_{NN}} = 2.76$  TeV [46].

Further analysis of wealth of  $v_2$  results at RHIC and LHC have signifi-

cantly contributed in establishing the formation of a strongly interacting quark-gluon plasma with viscosity to entropy density ratio ( $\eta/s$ ) close to the AdS/CFT lower bound of  $1/4\pi$  [47].

- **Probing QGP through Hard Probes:** Particles with large transverse momenta could be used as a convenient probe of the initial instants of nucleus-nucleus collision when the medium is at its hottest and highest energy density condition [48, 49]. These so-called “hard probes” are predominantly produced in a very short time scale which allows them to propagate through the dense partonic medium formed in A-A collisions. Any possible modification of the yield or other kinematic properties of these candidates compared to the elementary hadronic interactions (QCD vacuum) may provide relevant information on the mechanisms of the energy loss and hence the transport properties of the partonic medium [48]. In heavy ion collisions, high momentum partons scatter in the color-charged medium prior to hadronization. According to QCD, colored objects are susceptible to energy loss through gluon radiations and multi-parton interactions. As a consequence of in-medium energy loss, the energy of the leading partons would be strongly degraded resulting in a modification of the inclusive momentum distributions of high- $p_T$  hadrons or jets. The standard method to quantify these modifications is given by the **nuclear modification factor** or  $R_{AA}$ , defined as:

$$R_{AA}(p_T) = \frac{d^2 N_{AA}/dydp_T}{\langle N_{coll} \rangle \times d^2 N_{pp}/dydp_T} \quad (1.4)$$

This factor measures the deviation of the yield in A-A collisions compared to the number of “binary collision” ( $N_{coll}$ ) scaled p-p reference under the assumption that a A-A collision is an incoherent superposition of  $N_{coll}$  number of nucleon-nucleon scatterings. The number of binary collisions,

$N_{coll}$ , is determined by the Glauber model [50] using the measured Wood-Saxon nucleon density profile of the colliding nuclei. In absence of any

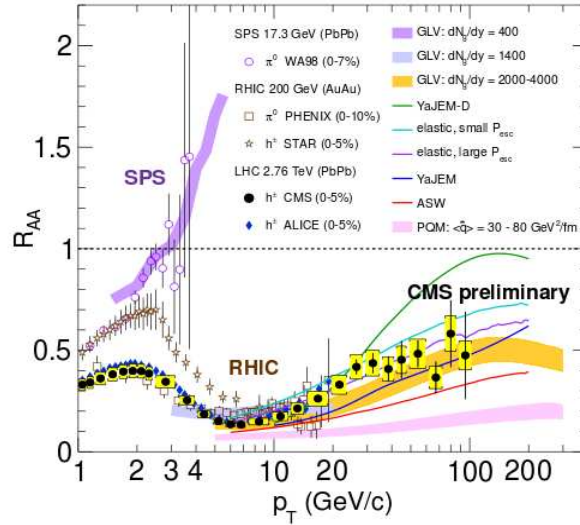


Figure 1.12: (Color online) Measurement of  $R_{AA}$  in central heavy ion collisions at  $\sqrt{s_{NN}} = 17.3 \text{ GeV}$ ,  $200 \text{ GeV}$  and  $2.76 \text{ TeV}$  [51, 52, 53, 54, 55, 56, 57]. Also shown comparison with different model predictions[58, 59, 60, 61]

modification,  $R_{AA}$  is expected to be unity i.e,  $R_{AA}=1$ , provided the mechanism of particle production scales with the number of binary collisions\*. Any deviation from unity in A-A collisions would primarily indicate a modification of the hadron yield due to the medium effects (also, there could be contributions from the initial state effects like modification of the partonic distribution within the colliding nuclei). By construction,  $R_{AA} < (>) 1$  implies suppression (enhancement) of high  $p_T$  hadron spectra compared to the  $N_{coll}$  scaled momentum spectra for p-p collisions at the same energy.

Fig. 1.12 presents a compilation of measured  $R_{AA}(p_T)$  of light flavor particles at SPS, RHIC and LHC energies. At RHIC, a large high- $p_T$  hadron suppression ( $R_{AA} \ll 1$ ) is observed above 2-3 GeV/c in central Au-Au

\* $R_{AA}$  less than unity for particles with small transverse momenta ( $< 2 \text{ GeV}/c$ ) is not necessarily because of a suppression, as, soft processes do not follow  $N_{coll}$  scaling

collisions compared to reference p-p or d-Au reactions [55, 56, 57]. The high- $p_T$  hadron suppression at RHIC can be reasonably reproduced by the parton energy loss models that assume the formation of a highly dense medium of initial gluon density  $dN^g/dy \approx 1400$  [59]. Since the energy loss ( $\Delta E_{loss}$ ) in these models are predicted to be proportional to the mid-rapidity gluon density or  $dN^g/dy$ , a larger hadron quenching is naturally expected for A-A collisions at higher values of  $\sqrt{s_{NN}}$ , as the mid-rapidity gluon density exhibits a logarithmic  $\sqrt{s_{NN}}$  dependent increase. Therefore, a strong suppression of high- $p_T$  hadron yields at LHC is in line with the predicted increase in the energy loss with  $\sqrt{s_{NN}}$ <sup>†</sup>. The  $R_{AA}$  at LHC was measured to be almost 7 times more suppressed than at RHIC in the  $p_T$  range of  $5 < p_T < 10$  GeV/c. A large attenuation of high- $p_T$  hadron spectra at LHC strongly suggest that the medium is densely populated with gluons ( $dN^g/dy \approx 2000-4000$ ) and at the same time it is highly opaque to the hard QCD-processes except for those which occur near the periphery of the fireball [51, 52, 69]. This was further confirmed by the angular correlation measurements between high- $p_T$  particles that shows a disappearance of away side yield of the back-to-back jet-hadron correlations in central A-A collisions [62, 63, 64].

Exploiting the impressive particle identification capability of the ALICE detector,  $R_{AA}$  of identified particles (pions, kaons, (anti-)protons) were measured upto a momentum range of 20 GeV/c. As shown in the figure 1.13, the nuclear modification factor at high  $p_T$  does not exhibit any particle species dependence, rather, all particles were found to be equally suppressed in the limit of the experimental uncertainties. This possibly suggests that jet-hadron chemistry of the leading particles is independent

---

<sup>†</sup>  $\frac{dN^g}{dy} \approx 0.75 \times (N_{part}/2) \times \ln(\sqrt{s_{NN}}/1.5)$

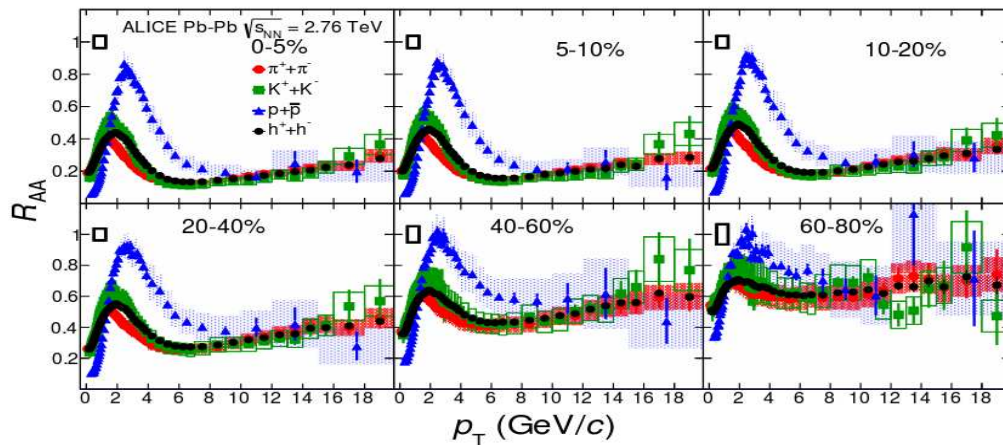


Figure 1.13: (Color online) The nuclear modification factor  $R_{AA}$  as a function of  $p_T$  for  $\pi$ , K,  $p/\bar{p}$  and hadrons. Results are shown for different collision centralities [91].

of the vacuum or medium fragmentation. Furthermore, baryon-to-meson ratio in the re-constructed jets (see Fig. 1.4.1) in heavy-ion collisions was found to be quantitatively similar to the inclusive baryon over meson ratio in p-p collisions. These observations confront with the idea, that different (medium modified) fragmentations for baryons and mesons are responsible for the stronger suppression of mesons over baryons in A-A collisions at intermediate- $p_T$  range [65].

Similar to the light flavoured particles, heavy flavour hadrons such as  $D$  and  $B$  mesons are expected to feature the evidence of heavy quark energy loss both in the inclusive spectra and correlations.  $D$ -meson  $R_{AA}$  in Pb-Pb collisions shows significant suppression at intermediate and high- $p_T$ . Since  $D$ -meson  $R_{p-Pb}$  was measured to be unity in p-Pb collisions [68], their suppression in heavy ion collisions may be regarded as an effect of charm quark energy loss due to interactions with hot and dense matter.

The heavy constituent of these particles, the charm and beauty quarks are calibrated probes of the medium, as they are only produced at a very early stage of a collision because of their heavy mass. The characteristic

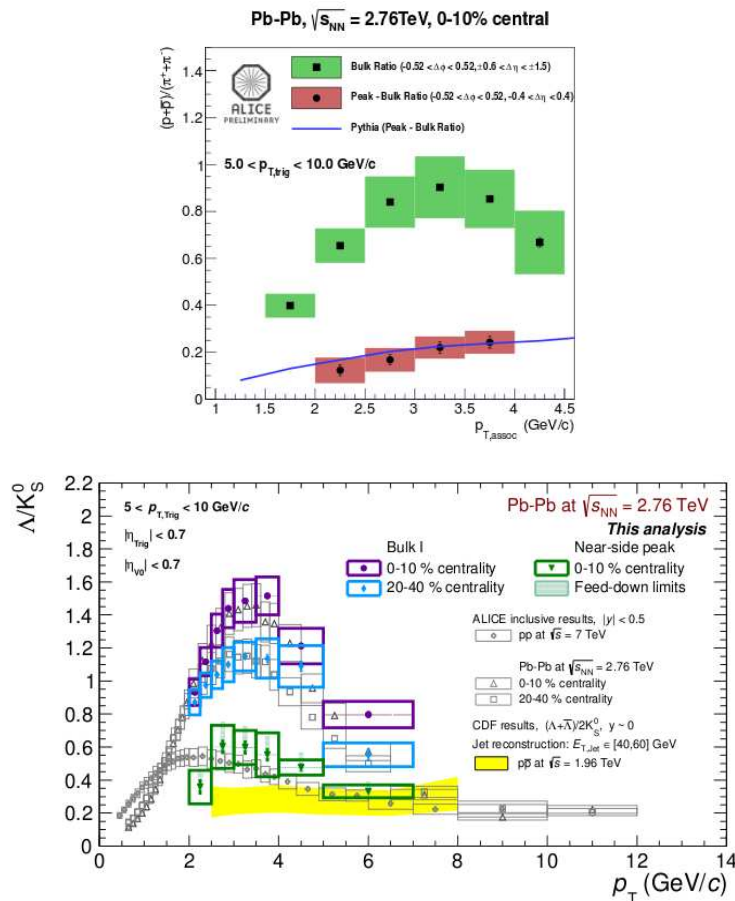


Figure 1.14: (Color online) Baryon-to-meson ratio in Jet and bulk. (top)  $p/\pi$  [66] and (bottom)  $\Lambda/K_s^0$  [67].

timescale of their production is given by  $t = 1/(2m_{c,b})$ , which is of the order of 0.1 fm/c for the charm quarks and 0.01 fm/c for the bottom quarks. This time is even shorter than the time scale of the QGP formation at LHC. As per a recent estimate, the QGP formation time at LHC is predicted to be around 0.3 fm/c [74].

Like light quarks and gluons, heavy quarks also interact with the medium constituents and lose a part of its energy by collisional and radiative processes. The heavy quark energy loss can also be studied by measuring the nuclear modification factor or  $R_{AA}$  of  $D$  and  $B$  mesons, which contain at least one heavy quark. From the theoretical perspective, the QCD en-

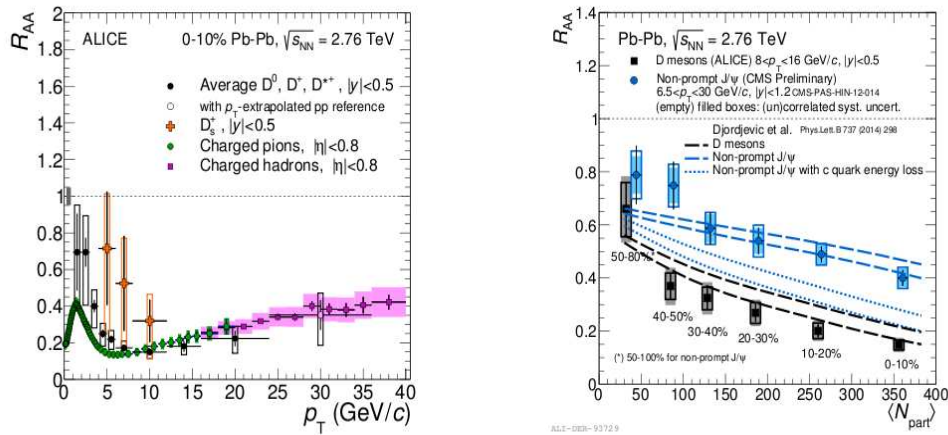


Figure 1.15: (Color online) **Left:**  $R_{AA}$  of D-meson as a function of  $p_T$  in central Pb-Pb collisions at  $\sqrt{s_{NN}} = 2.76$  TeV [70] compared to  $D_s^0$  [75], charged particle [69] and pion [91]  $R_{AA}$ . **Right:** D-meson [77] and non-prompt  $J/\psi$  [78, 73]  $R_{AA}$  as a function of centrality in Pb-Pb collisions at the LHC.

ergy loss of quarks and gluon are expected to follow a mass hierarchy, i.e.,  $\Delta E_Q^{c/b} < \Delta E_q^{u/d/s} < \Delta E_g$ . This is mainly because of the *dead cone effect*, that reduces the radiative energy loss of charm and bottom quarks by  $\sim 25\%$  and  $75\%$ , respectively. Besides the mass hierarchy of energy loss, quarks are expected to lose less energy than gluons because of their weak coupling to the medium <sup>‡</sup>. Thus, it implies a less heavy quark energy loss and, a lesser suppression of the heavy flavoured particles than the light flavor ones.

The predicted quark mass (*dead cone effect*) and colour-charge dependence of in-medium parton energy loss could be tested by comparing  $R_{AA}$  of D-mesons, B-hadrons and light flavored particles. The result of these comparisons are presented in the left panel Fig. 1.15 show, in contrary to the theoretical predictions, there is no appreciable difference between  $R_{AA}$  of D-mesons and pions. It is seen that at high- $p_T$ , both  $D$ -mesons and pions are equally suppressed. The lack of any significant difference between

<sup>‡</sup>In the analytic limit  $\Delta E_g = 2.25\Delta E_q$

pion and D-meson  $R_{AA}$  is however, not compatible with the radiative energy loss calculations with initial gluon density required to reproduce the quenching of the light flavor hadron spectra. It has been shown, apart from the color-charge and quark-mass dependence of energy loss, a harder fragmentation function of the charm quarks relative to those of the light quarks and gluons may lead to the similar values of D-mesons and pions  $R_{AA}$  at high  $p_T$  [71, 72]. Similarly a stronger suppression of D-mesons compared to non-prompt  $J/\Psi$  (from  $B$ -hadron decay), shown in the right panel of the Fig.1.15 is predominantly driven by the quark mass dependence of the parton energy loss, i.e,  $\Delta E_{rad}(c) > \Delta E_{rad}(b)$ .

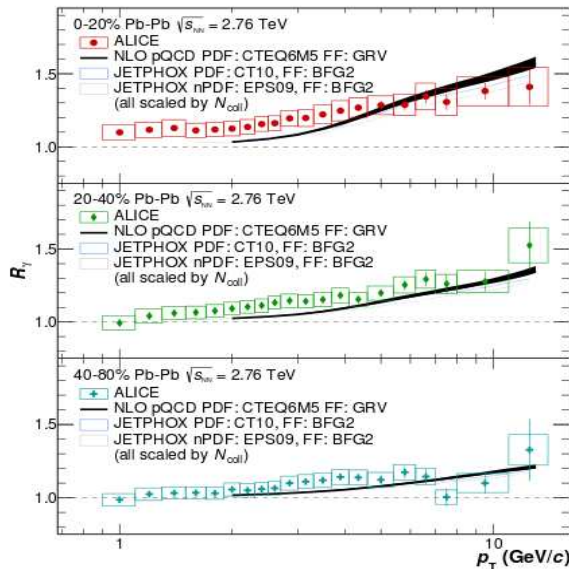


Figure 1.16: (Color online) Measurement of nuclear effects on direct photons in different collision centrality for Pb-Pb collisions at  $\sqrt{s_{NN}} = 2.76$  TeV compared with number of binary collision scaled pQCD calculation [79].

Another class of observables which has been extensively studied at LHC are the electromagnetic probes. At high  $p_T$ ,  $R_{AA}$  of prompt photons, shown in Fig. 1.16 [79, 80, 81] and vector bosons [82, 83], shown in Fig. 1.17, are seen to exhibit  $N_{coll}$  scaling over all centrality classes of Pb-Pb collisions. Within statistical and systematic uncertainties, the  $R_{AA}$

values of  $Z$ -bosons and prompt photons are seen to be consistent with unity. Since photons and gauge bosons interact through electromagnetic and weak interactions, their productions and interactions are hardly affected by the QCD medium. Therefore, the production of massive gauge bosons and photons are insensitive to the final state interactions and provide a cleaner channel to probe the nuclear modifications other than those due to the final state effects (like those associated with the modification of parton distribution function due to nuclear shadowing and the Cronin effect (initial state effects)). Lack of any significant modification of the

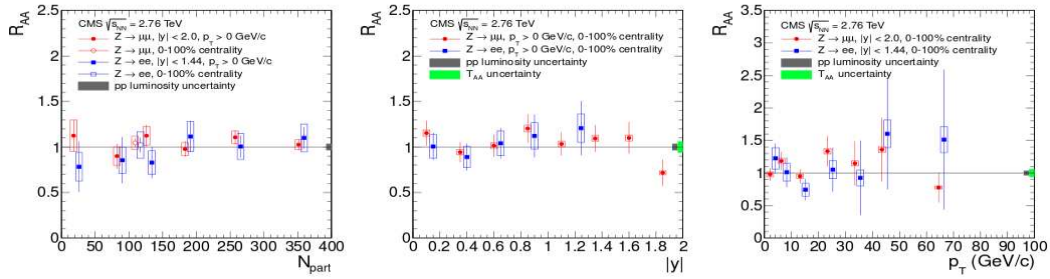


Figure 1.17: (Color online)  $Z$  boson  $R_{AA}$  in Pb-Pb collisions at  $\sqrt{s_{NN}} = 2.76$  TeV as a function of centrality, rapidity and transverse momentum comparing the muon and electron channel results

prompt photon and  $Z$ -boson yields for Pb-Pb collisions at high- $p_T$  compared to the number binary collision scaled pp reference, i.e.,  $R_{AA} \sim 1$ , suggest that the  $R_{AA} < 1$  for charged particles in A-A collisions is because of energy loss due to strong interactions in a dense partonic medium.

- Quark Coalescence- an indirect probe for de-confinement:** So far, discussions on the onset of partonic degrees of freedom mostly relied on the observations that emerged out as a consequence of parton energy loss in a de-confined quark-gluon plasma and / or large elliptic anisotropy commensurable with hydrodynamic calculations with QCD-inspired equation of states. It must be noted that an appropriate mechanism of hadronization is indeed essential to derive reliable information prior to the hadronization. Since hadronization is a non-perturbative phenomena, our current knowledge on hadron formation mostly depends on the phenomenological models.

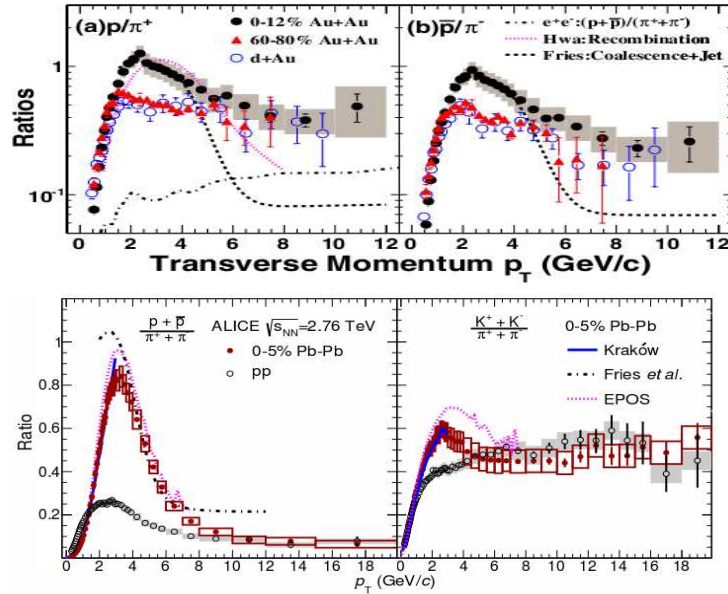


Figure 1.18: (Color Online) **Top:** The inclusive  $p/\pi$  and  $\bar{p}/\pi^-$  ratio from d-Au and Au-Au at  $\sqrt{s_{NN}} = 200$  GeV. The dotted-dashed lines shows the inclusive  $p/\pi$  ratio from light quark jets in  $e^+ + e^-$  collisions at 91.2 GeV. Also shown comparisons with different model calculations. **Bottom:**  $p_T$ -dependence of particle ratios measured in pp and 0-5% most central Pb-Pb collisions at 2.76 TeV. Comparison with theoretical predictions for 0-5% Pb-Pb collisions are also shown.

There have been several astounding discoveries at RHIC and one of them is certainly the large baryon over meson enhancement in mid-central and

central Au-Au collisions at intermediate values of transverse momentum ( $2 < p_T < 5$  GeV/c) [84]. An enhancement in  $p/\pi$  and  $\bar{p}/\pi$  ratios was observed as function of centrality and the ratios in most central Au-Au/Pb-Pb collisions was a factor of 3/5 higher than in d-Au/pp collisions at same energy, as shown in Fig 1.18. In central nucleus-nucleus collisions, ratios peak around 2-3 GeV/c, followed by a decrease at higher  $p_T$ . The drop in the  $p/\pi$  ratios at higher- $p_T$  is attributed to the growing significance of particle productions from the (modified) jet-fragmentations. But, at the intermediate- $p_T$  range, the baryons are enhanced to such an extent that it almost nullified the effect of jet-quenching (modifications) that seems to suppress the inclusive hadron and meson spectra at intermediate and high  $p_T$  ranges [85].

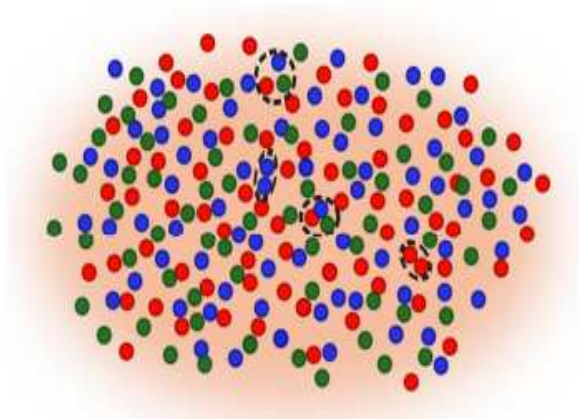


Figure 1.19: (Color online) Pictorial representation of coalescence mechanism of hadronization from hot and dense quark gluon plasma.

The different trends in suppression for baryons and mesons was inconsistent with the scenario where particles are produced from initial hard scatterings followed by parton energy loss and vacuum fragmentation. This so-called **baryon anomaly** was therefore an indication of new hadronization mechanism, which along with jet-fragmentations could account for the excess baryon production at the intermediate ranges of  $p_T$ .

It was soon realized, baryon-meson grouping in the nuclear modification factor ( $R_{AA}$ ) could be a manifestation of particle production by **quark-recombination**. In this process, hadrons at intermediate  $p_T$  are dominantly produced by the recombination or coalescence of quarks from a thermalized partonic medium [86]. This was further supported by the number of constituent quarks (NCQ) scaling of transverse momentum dependence of  $v_2$  of different particles as shown in Fig. 1.20, in the same momentum range.

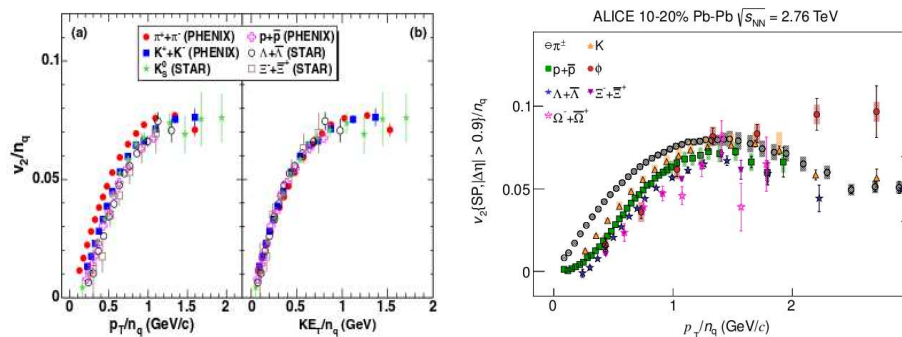


Figure 1.20: (Color online) The  $p_T/n_q$  or  $KE_T/n_q$  dependence of  $v_2/n_q$  for identified hadrons,  $n_q$  is the number of valance quarks in a given hadron( for mesons,  $n_q = 2$ ; and, for baryons  $n_q = 3$ ): (left) minimum bias Au-Au  $\sqrt{s_{NN}} = 200$  GeV, (right) for 10-20 % collision centrality in Pb-Pb  $\sqrt{s_{NN}} = 2.76$  TeV.

It was shown, that the NCQ-scaling is naturally accounted by the models invoking quark recombination as a mechanism of hadronization. As recombination models explicitly assume the dominance of quark degrees of freedom at the time of hadronization, success achieved in explaining wide range of data at intermediate  $p_T$  was considered as a concrete evidence for the development of collectivity in the early partonic stage: further confirming the discovery of strongly coupled quark-gluon plasma (s-QGP) at the RHIC.

This scaling property was also tested at LHC. Recent measurements by the ALICE collaboration have shown that not only  $v_2$  [46] but also the

higher flow harmonics ( $v_3, v_4$  and  $v_5$ ) [87] exhibit NCQ-scaling at an approximate level of  $\pm 20\%$ .

### 1.4.2 Motivation of the Present Thesis

The puzzle of baryon to meson enhancement continues at LHC without any exception. Hadronization by recombination of boosted thermal quarks from a collectively expanding partonic medium reasonably describes the enhancement of baryons relative to meson in central collision as well as it accounts for the particle species dependence of  $R_{AA}$  at the intermediate  $p_T$  range. However, in hybrid model calculations like EPOS [92], the large baryon-to-meson enhancement at intermediate  $p_T$  was argued to be a combined effect of strong radial boost generated during the hydrodynamical evolution of the bulk matter and the jet-bulk interactions. A comparison with the ALICE-data [91] shows that EPOS could reproduce the centrality dependence of proton-to-pion ratio but overestimates the magnitude. Although several models could qualitatively describe the baryon-meson effect at intermediate  $p_T$  but its exact origin is yet to be understood unambiguously.

As of now, the large baryon-to-meson enhancement at RHIC was interpreted as a consequence of the recombination of boosted thermal quarks from a collectively flowing partonic medium. This mechanism was also held responsible for the observed baryon-meson splitting of  $v_2(p_T)$  which eventually leads to the NCQ-scaling. At RHIC, this scaling was considered as a confirmation of quark-recombination- a novel mechanism of particle production which could compete with jet-fragmentations in the intermediate regions of  $p_T$  where hydrodynamics might not be dominant.

Among all particle that were studied at RHIC,  $\phi$ -mesons were of special

interest. Being a meson of mass comparable to protons and  $\Lambda$ s, it offers an unique testing ground to distinguish whether baryon-meson grouping is related to mass of the particle or type of the particle (baryon versus meson). It was observed, despite having a mass similar to protons and  $\Lambda$ s, both  $R_{AA}$  [88, 89] and  $v_2(p_T)$  [90] of  $\phi$ -mesons were consistent with other lighter mesons: implying that particle type grouping is a baryon-meson effect, naturally accounted by the quark-coalescence or recombination models.

However, at LHC, situation is somewhat complicated because of the following observations:

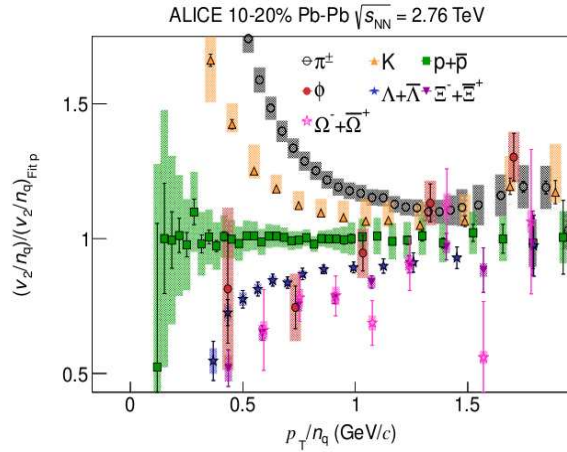


Figure 1.21: (Color online) Double ratio of  $v_2/n_q$  as a function of  $p_T/n_q$  relative to the seventh order polynomial fit to  $v_2/n_q$  of  $p/\bar{p}$  for Pb-Pb  $\sqrt{s_{NN}} = 2.76$  TeV in 10-20% collision centrality[46]

- Violation of NCQ-scaling. As can be seen from Fig. 1.21,  $v_2/n_q$  of different hadrons when compared to a common fit, maximum of 20% departure from perfect scaling is observed.
- Comparable magnitude of  $v_2(p_T)$  of  $\phi$ -mesons and protons at intermediate values of  $p_T$ .

These observations were taken as an indication, that at LHC, transverse

momentum distribution of particles at the intermediate  $p_T$  is predominantly determined by the mass of the particles rather than its number of constituent quarks. This is certainly in contradiction to the recombination expectations, but consistent with hydrodynamical calculations.

Thus it may be understood that the theoretical models that reproduce baryon/meson difference in the inclusive ratios and nuclear modification factors, employ some mechanisms that could extend the range of soft processes of particle production favouring baryons over mesons upto higher values of  $p_T$ . This could be done either by hydrodynamics or by quark-recombinations. However, in a standard picture, hadrons at high transverse momentum are dominantly produced by the fragmentation (fragmentation functions may be modified in A-A collision) of the energetic partons (hard processes)[93, 94]. But, due to the lack of any sharp cut-off, hadronic observables at intermediate  $p_T$  have contributions from both hard and soft processes. Although the combined approach of hard and soft processes particle production describes different aspects of the published result at intermediate  $p_T$ , but the origin of “baryon anomaly” has remained incomprehensible till date [95, 96].

In this thesis work, angular ( $\Delta\eta, \Delta\phi$ ) correlations measurements are performed between the identified leading hadrons (protons and pions as trigger particles) and the unidentified charged particles (associated) at intermediate  $p_T$ . The choice of the trigger  $p_T$  region is of particular interest as it is thought to have contributions from jet-fragmentations and other soft processes of particle production. As the strength of the correlations, quantified by the near side jet-like yield, is strongly sensitive to the relative abundance of trigger sample from hard and soft interactions, comparing the magnitude of baryon and meson triggered correlations over a wide range of centrality may provide additional information on the possible mechanisms of hadronization [97, 98, 99, 100]. In

addition, such measurements in different  $p_T$  ranges may reveal important information on the jet-medium interactions[101].

The main aim of this thesis is to identify the origin of baryon-meson difference at intermediate values of transverse momentum by comparing the results obtained by analyzing data collected by the ALICE collaboration for Pb-Pb collisions at  $\sqrt{s_{NN}}=2.76$  TeV with Monte Carlo model calculations like AMPT and EPOS. While AMPT implements hadronization by quark recombinations, EPOS incorporates an additional hadronization mechanism at intermediate  $p_T$  where interactions between jet and bulk is considered.

The organization of this thesis is as follows. In chapter 2, results from the AMPT model calculations including generic description on the construction of two dimensional (2-D)  $(\Delta\eta, \Delta\phi)$  angular correlation functions, yield calculations and interpretation of the results in context of coalescence formalism are presented. Discussions on the different sub-components of the ALICE detector system, general scheme of data acquisition, noise filtering, event and track reconstructions are discussed in chapter 3. Chapter 4 discusses about event and track selection criteria with emphasis on those used in this analysis, particle identification using on ALICE Time Projection Chamber (TPC) and Time of Flight (TOF) detector and build-up of efficiency and acceptance corrected two dimension  $(\Delta\eta, \Delta\phi)$  correlation functions in Pb-Pb collisions at  $\sqrt{s_{NN}} = 2.76$  TeV. Finally, in Chapter 5 results on the centrality dependence of near side jet-like yield associated with baryon and meson triggers in different  $p_T$  ranges are presented. Comparison are made with Monte Carlo models with different implementations of hadronization techniques like hydro+jets (EPOS) and coalescence (AMPT-SM). This chapter closes after summarizing the results and discussing the outcome of this analysis. A chapter is added to this thesis which illustrates hardware activity in VECC with emphasis on the fabrication and

testing of a large size bakelite Resistive Plate Chamber (RPC) [1, 103, 104] designed to meet the detector requirements for the future neutrino-hunting facilities in India (**INO**) [2] and in the Fermi Lab, USA (**DUNE**) [14].

# Bibliography

- [1] A online version of Stephen Hawking's **A Brief History of Time**.
- [2] M. Riordan and W. A. Zajc, The first few microseconds, *Sci. Am.* 294N5, 24 (2006) [*Spektrum Wiss.* 2006 N11, 36 (2006)].
- [3] Coles, P., ed (2001). *Routledge Critical Dictionary of the New Cosmology*. Routledge. p. 202. ISBN 0-203-16457-1.
- [4] G. (1927) " Expansion of the universe, A homogeneous universe of constant mass and increasing radius accounting for the radial velocity of extragalactic nebulae". *Monthly Notices of the Royal Astronomical Society* 91: 483-490, doi:10.1093/mnras/91.5.483
- [5] D. J. Schwarz, *Annalen Phys.* 12, 220 (2003) [astro-ph/0303574].
- [6] K. A. Olive, *Nucl. Phys. B* 190, 483 (1981).
- [7] E.V. Shuryak, *Phys. Rept.* 61, 71 (1980).
- [8] D.J. Gross, F.Wilczek, *Phys. Rev. D* 8, (1973).
- [9] H.D. Politzer, *Phys. Rev. Lett.* 30, (1973).
- [10] K.G. Wilson, *Phys. Rev. D* 10, 2445 (1974).
- [11] A. M. Polyakov, *Nucl. Phys. B* 120, 429 (1977) .

- [12] D. Gross, Asymptotic freedom and QCD: A historical perspective, Nucl.Phys.Proc.Suppl. 135 (2004) 193211.
- [13] F. Karsch and E. Laermann, arXiv:hep-lat/0305025, (2003).
- [14] F. Karsch, E. Laermann and A. Peikert, Phys. Lett. B 478, 447 (2000).
- [15] S. Hands, Contemp. Phys. 42, 209 (2001).
- [16] C. Nonaka and M. Asakawa, arXiv:1204.4795[nucl-th], (2012).
- [17] I. Arsene et al. (BRAHMS Collaboration), Nucl. Phys. A 757, 1 (2005), nucl-ex/0410020.
- [18] B. Back et al. (PHOBOS Collaboration), Nucl. Phys. A 757, 28 (2005), nucl-ex/0410022.
- [19] J. Adams et al. (STAR Collaboration), Nucl. Phys. A 757, 102 (2005), nucl-ex/0501009.
- [20] K. Adcox et al. (PHENIX Collaboration), Nucl. Phys. A 757, 184 (2005), nucl-ex/0410003.
- [21] S. Chatrchyan et al. (CMS Collaboration), Phys. Rev. Lett. 109, 152303 (2012).
- [22] J.T. Mitchell (for the PHENIX Collaboration), arXiv:1601.00904.
- [23] Ranbir Singh et al., Advances in High Energy Physics 761474, (2013).
- [24] A. Bazavov et al., Phys. Rev. D 90, 094503 (2014).
- [25] Y. Aoki et al., J. High Ene. Phys. 06, 088 (2009).
- [26] F. Karsch presentation in ICPAQGP 2015, VECC, Kolkata, <http://indico.vecc.gov.in/indico/getFile.py/access?contribId=181&sessionId=11&resId=0&materialId=0&confId=29>.

- [27] A. Andronic, P. Braun-Munzinger, and J. Stachel, Phys. Lett. B 673, 142 (2009).
- [28] P. Braun-Munzinger, J. Stachel, and C. Wetterich, Phys. Lett. B596, 61 (2004).
- [29] A. Andronic, P. Braun-Munzinger, K. Redlich, and J. Stachel, J.Phys.G G38, 124081 (2011).
- [30] R. Rapp and E. V. Shuryak, Phys. Rev. Lett. 86, 2980 (2001).
- [31] M. Floris [ALICE Collaboration], arXiv:1108.3257 [hep-ex].
- [32] J. Adams et al. (STAR Collaboration), Nucl.Phys. A 757, 102 (2005), nucl-ex/0501009.
- [33] K. Adcox et al. (PHENIX Collaboration), Nucl.Phys. A 757, 184 (2005), nucl-ex/0410003.
- [34] S. Voloshin and Y. Zhang, Z. Phys. C 70, 665 (1996).
- [35] A. M. Poskanzer and S. A. Voloshin, Phys. Rev. C 58, 1671 (1998).
- [36] D. Teaney, J. Lauret and E. V. Shuryak, Phys. Rev. Lett. 86, 4783 (2001).
- [37] C. Alt et al. (NA49 Collaboration), Phys. Rev. C 68, 034903 (2003).
- [38] P. F. Kolb et al., Phys. Lett. B 500, 232-240, (2001).
- [39] J.-Y. Ollitrault, Phys. Rev. D 46, 229 (1992).
- [40] H. Sorge, Phys. Rev. Lett. 82, 2048 (1999).
- [41] B. Zhang et al., Phys. Lett. B 455, 45 (1999).
- [42] P. Huovinen et al., Phys. Lett. B 503, 58 (2001).

- [43] D. Teaney, J. Lauret, and E.V. Shuryak, Phys. Rev. Lett. 86, 4783 (2001).
- [44] C. Adler et al. (STAR Collaboration), Phys. Rev. Lett. 87, 182301 (2001).
- [45] L. Adamczyk et al. (STAR Collaboration), Phys. Rev. Lett. 116, 062301 (2016).
- [46] B. Abelev et al. (ALICE Collaboration), JHEP 06 190, (2015) .
- [47] P. Kovtun, D. T. Son and A. O. Starinets, Phys. Rev. Lett. 94, 111601 (2005).
- [48] D. d'Enterria, Jet quenching, Landolt-Boernstein, Springer-Verlag Vol. 1-23A (2010) 99, arXiv:0902.2011.
- [49] S. Chatrchyan et al. (CMS Collaboration), Phys. Rev. C 84, 024906 (2011).
- [50] B. Alver et al., Phys. Rev. C 77, 014906 (2008).
- [51] B. Abelev et al. (ALICE Collaboration) Phys. Lett. B 696, 30 (2011).
- [52] S. Chatrchyan et al. (CMS Collaboration), Eur. Phys. J. C 72, 1945 (2012).
- [53] M. M. Aggarwal et al. (WA98 Collaboration) Eur. Phys. J. C 23, 225 (2002).
- [54] D. G. d'Enterria, Phys. Lett. B 596 (2004) 32.
- [55] A. Adare et al., (PHENIX Collaboration), Phys. Rev. Lett. 101, 232301 (2008).
- [56] J. Adams et al. (STAR Collaboration), Phys. Rev. Lett. 91, 172302 (2003).
- [57] B.I. Abelev et al. (STAR Collaboration), Phys. Rev. Lett. 97, 152301 (2006).
- [58] A. Dainese, C. Loizides, and G. Paic, Eur. Phys. J. C 38, 461 (2005) .

- [59] I. Vitev and M. Gyulassy, Phys. Rev. Lett. 89, 252301 (2002).
- [60] I. Vitev, J. Phys. G30, S791 (2004) .
- [61] T. Renk et al.,Phys. Rev. C 84, 014906 (2011).
- [62] C. Adler et al (STAR Collaboration),Phys. Rev. Lett. 90, 082302 (2003).
- [63] L. Adamczyk et al. (STAR Collaboration), Phys. Rev. Lett. 112, 122301 (2014).
- [64] K. Aamodt et al. (ALICE Collaboration), Phys. Rev. Lett. 108, 092301 (2012).
- [65] S. Sapeta and U. A. Wiedemann, Eur. Phys. J. C 55, 293 (2008).
- [66] Misha Veldhoen for the ALICE Collaboration, arXiv:1207.7195,
- [67] Xitzel Sanchez Castro thesis, CERN-THESIS-2015-112 - 190 p.
- [68] B. Abelev et al. (ALICE Collaboration), Phys. Rev. Lett. 113, 232301 (2014).
- [69] B. B. Abelev et al. (ALICE Collaboration) Phys. Lett. B 720, 52 (2013).
- [70] J. Adam et al. (ALICE Collaboration), JHEP 03 081, (2016).
- [71] M. Djordjevic, M. Djordjevic, and B. B. Blagojevic,Phys. Lett. B 737, 298 (2014).
- [72] M. Djordjevic and M. Djordjevic, Phys. Lett. B 734, 286 (2014).
- [73] CMS Collaboration,  $J/\psi$  results from CMS in PbPb collisions, with 150 b1 data, Tech. Rep. CMS-PAS-HIN-12-014, (2012).
- [74] F.-M. Liu and S.-X. Liu, Phys. Rev. C 89, 034906 (2014).

- [75] J. Adam et al. (ALICE Collaboration), JHEP 03 082, (2016).
- [76] B. B. Abelev et al. (ALICE Collaboration) Phys. Lett. B 736, 196 (2014).
- [77] J. Adam et al. (ALICE Collaboration), JHEP 11 205, (2015).
- [78] S. Chatrchyan et al. (CMS Collaboration), JHEP 05 063, (2012) .
- [79] J. Adam et al. (ALICE Collaboration), Phys. Lett. B 754, 235-248 (2016).
- [80] S. Chatrchyan et al (CMS Collaboration), Phys.Lett. B 710, 256277 (2012)  
.
- [81] G. Aad et al (ATLAS Collaboration), Phys. Rev. C 93, 034914 (2016).
- [82] G. Aad et al (ATLAS Collaboration), Eur. Phys. J. C 75, 23 (2015).
- [83] S. Chatrchyan et al (CMS Collaboration), JHEP 03 022, (2015).
- [84] S. S. Adler et al. (PHENIX Collaboration), Phys. Rev. Lett. 91, 172301 (2003).
- [85] B. I. Abelev et al. (STAR Collaboration), Phys. Rev. Lett. 97, 152301 (2006).
- [86] Z.W. Lin and C. M. Ko, Phys. Rev. Lett. 89, 202302 (2002); D. Molnar and S. A. Voloshin, Phys. Rev. Lett. 91, 092301 (2003); R. C. Hwa and C. B. Yang, Phys. Rev. C 67, 064902 (2003); R. J. Fries, B. Muller, C. Nonaka, and S. A. Bass, Phys. Rev. Lett. 90, 202303 (2003); V. Greco, C. M. Ko, and P. Levai, Phys. Rev. Lett. 90, 202302 (2003).
- [87] J. Adam et al. (ALICE Collaboration), arXiv:1606.06057.

- [88] J. Adam et. al (STAR Collaboration), Phys. Rev. Lett. 92, (2004) 052302.
- [89] J. Adam et. al (STAR Collaboration), Phys. Lett. B 612, 181 (2005).
- [90] B.I. Abelev et, al (STAR Collaboration), Phys. Rev. C 79, 064903 (2009).
- [91] J. Adam et. al (ALICE Collaboration), Phys. Rev. C 93, 034913 (2016).
- [92] K. Werner et. al, Phys. Rev. C 85, 064907 (2012).
- [93] S. Albino, B. Kniehl, and G. Kramer, Nucl. Phys. B 725, 181 (2005).
- [94] S. Albino, B. Kniehl, and G. Kramer, Nucl. Phys. B 803, 42 (2008).
- [95] K. Werner, Phys. Rev. Lett. 109, 129903 (2012).
- [96] R. C. Hwa and C. Yang, Phys. Rev. Lett. 97, 042301 (2006).
- [97] S.S. Adler et. al (PHENIX Collaboration) Phys. Rev. C 71, 051902 (2005).
- [98] L. Adamczyk et al. (STAR Collaboration), Phys. Lett. B 751, 233 (2015).
- [99] A. Adare et al. (PHENIX Collaboration), Phys. Lett. B 649, 359 (2007).
- [100] S. Choudhury, D. Sarkar and S. Chattopadhyay Phys. Rev. C 93, 054902 (2016).
- [101] S. Chatrchyan et al. (CMS Collaboration), Eur. Phys. C 72, 10052 (2012).
- [102] R. Ganai et al., 2016 JINST 11 P04026, arXiv:1510.02028.
- [103] R. Ganai et al., arXiv:1604.03668.
- [104] R. Ganai et al., arXiv:1603.04875.
- [105] <http://www.ino.tifr.res.in/ino//OpenReports/INOResultReport.pdf>, INO Project Report, INO/2006/01.
- [106] <http://www.dunescience.org/>

# Chapter 2

## Testing of the coalescence mechanism using identified particle angular correlations at intermediate $p_T$

### 2.1 Introduction

Temperature and energy density attained in ultra-relativistic heavy ion collisions at RHIC and LHC are compatible with the lattice quantum chromodynamics (l-QCD) thresholds for phase transition from hadronic to a de-confined state of quarks and gluons [1, 2, 3]. The Hot and dense matter thus formed, known as quark-gluon plasma (QGP), cools down in the process of evolution, re-confines to hadrons, and streams freely to detectors [4]. This gives us a unique opportunity to study the mechanism of particle production under extreme conditions. The  $p_T$  spectra of the final state particles give an insight on their production mechanism and of interactions at various stages of evolution [5, 6, 7]. Various theoretical models have been proposed but no unique prescription is available to explain the  $p_T$  spectra over the entire experimentally measured range. Particle production below  $p_T \approx 2 \text{ GeV}/c$ , referred to as the bulk region can be reproduced by the hydro-inspired models [8, 9, 10]. For

$p_T > 6$  GeV/ $c$ , hadronization is primarily through fragmentation of high  $p_T$  partons to a collimated shower of hadrons (jets). This process involves parton scattering with large momentum transfer and can be convincingly described by perturbative QCD calculations [11, 12].

However, none of these approaches could account for particle production at the intermediate  $p_T$  ( $2 < p_T < 6$  GeV/ $c$ ). The observations like the anomalous enhancement of inclusive baryon over meson yield, particle species dependence of the nuclear modification factor ( $R_{AA}, R_{CP}$ ) and baryon-meson ordering of the elliptic flow coefficient ( $v_2$ ) were found to be at odds with either of these formalisms [6, 13]. Plausible explanations to the enhanced baryon/meson or nuclear modifications were achieved from the models either incorporating recombination of quarks [14, 15, 17, 18] or a boost from a radially expanding medium pushing massive hadrons to higher  $p_T$  (Hydrodynamics) [8, 10]. In principle, both the approaches attempt to generate high  $p_T$  baryons from soft processes as opposed to mesons.

Another explanation could be in terms of energy loss of partons in the medium. The independent fragmentation of energetic partons based on pQCD calculations gives baryon/meson  $\sim 0.1$  both in light and strange flavor sectors [15]. This is in contradiction to the experimental results. However, jet fragmentations are strongly influenced by the dense medium leading to an alteration of the fragmentation function [19, 20]. It has been argued that the medium modified fragmentation can also be a potential source of enhanced baryon generation [21]. Jet-like peak structure observed in the correlation measurements between baryons and charged hadrons at intermediate  $p_T$  reported by the PHENIX and the STAR Collaborations may be an indication that the baryon enhancement is associated to the medium induced jet modification [22, 23].

The high density environment achieved in heavy-ion collisions may be conducive for hadron formation through coalescence of quarks. In simple coalescence approach, quark and anti-quark pairs close in phase space recombine into mesons and three quarks to (anti-)baryons. Thus at the same  $p_T$ , baryons and mesons are formed from the quarks with momenta  $\sim p_T/3$  and  $\sim p_T/2$  respectively. Different approaches of quark recombination have been suggested and adopted by various groups. Each of them particularly differ in the way high  $p_T$  partons from the initial hard-scatterings and the thermalized soft partons are treated. While some consider coalescence of only soft partons and hard partons to hadronize by fragmentation only [14, 15], others allow coalescence of both soft and hard mini-jet partons [18]. Since the  $p_T$  spectra of these hard partons show a power-law behaviour, an exponential thermal spectrum of soft partons is therefore imperative for large baryon to meson enhancement. All these implementations with proper tuning of parameters describe the basic features at intermediate  $p_T$  e.g.,  $p_T$  spectra,  $v_2$ -scaling reasonably well at RHIC energy. At LHC, scaling violation of  $v_2$  is somewhat larger than that at RHIC and may be naturally explained within soft-hard recombination formalism [24]. Additionally, the near-side peak structure observed in the measurements of azimuthal correlations triggered by identified particles at intermediate  $p_T$  at RHIC energy have been reasonably explained with the inclusion of mini-jet partons or partons from hard scatterings in the coalescence formalism. Thus an alternative way to look for the source of baryon anomaly at intermediate  $p_T$  is to study the baryon-charged hadron correlations. The angular correlation measurements are likely to be more sensitive to probe the contribution of hard scattering towards hadron production. This chapter, reports the sensitivity of di-hadron correlation measurements to the coalescence mechanisms when measured by taking identified mesons ( $\pi$ ) and baryons ( $p/\bar{p}$ ) at intermediate  $p_T$  as leading hadrons.

The two-particle azimuthal correlation functions triggered by leading hadrons encode the characteristic of the production mechanism of the trigger and associated particles. The correlation measurements with high  $p_T$  trigger particles ( $> 4\text{-}6 \text{ GeV}/c$ ) in p-p collisions manifest itself as di-jet peaks in azimuth, an imprint of the QCD fragmentation of back to back hard scattered partons [25]. At intermediate  $p_T$ , hadronization through recombination would lead to “trigger dilution” in central heavy ion collisions [22, 23]. Trigger particles originating from recombination or coalescence of thermal quarks from the dense partonic medium would lack correlated hadrons at small angular region (jet-like correlation). This would effectively dilute (reduce) per trigger associated yield. Furthermore, dilution is expected to be prominent for baryon trigger than meson trigger as the baryon production is more favourable through coalescence of quarks.

In this work, the sensitivity of the near side yields of proton and pion triggered azimuthal correlation functions to the coalescence mechanism have been tested using two versions of the AMPT model [26]. While the partonic version (SM) of the AMPT model produces particles by the coalescence of quarks, the default version has only mini-jets and strings fragmenting to hadrons. We have built triggered correlation functions from the events generated from either version of the AMPT model for Pb-Pb collision at  $\sqrt{s_{NN}} = 2.76 \text{ TeV}$  and extracted near side yield as final observable.

## 2.2 The AMPT Model

The AMPT model has been extensively studied at RHIC and LHC energies. Free parameters of the model have been constrained by a wide range of experimental data. If broadly classified, model has two modes: Default (mini-jets

and strings) and String Melting (replicate QGP allowing strings to melt into partons) [27]. The spatial and momentum distributions of mini-jet partons and excited soft strings, obtained from the HIJING model [28] are used as initial conditions for subsequent modelling of partonic evolution. In the default version, mini-jet partons are evolved via a parton cascade model (ZPC) [29] which basically includes 2-body elastic scatterings among the partons with a medium dependent scattering cross-section represented as  $\sigma_p \simeq 9\pi\alpha_s^2/2\mu^2$  where  $\alpha_s$  is the QCD coupling constant for strong interactions and  $\mu$  is the Debye screening mass of gluons in QGP medium. Although, it is a function of temperature and density of the partonic medium but in ZPC it is parameterised to fix the magnitude of scattering cross-section. At the end of evolution, these mini-jet partons are recombined with their parent strings and are eventually hadronized by the Lund string fragmentation [30]. The post hadronization stage is modelled by A Relativistic Transport model (ART) [31, 32], which guides the hadronic interactions till freeze-out.

To emulate the conditions similar to the de-confined QGP, AMPT has been extended to perform melting of excited strings. Taking initial conditions from HIJING, strings are first fragmented to hadrons followed by conversion of these hadrons to valance quarks/antiquarks preserving their flavor and spin quanta. Now the system comprises both mini-jet and string melted partons, which are further scattered through ZPC. Once the interaction ceases, partons are re-confined to hadrons via an implementation of coalescence formalism that combines two or three partons nearest in coordinate space to mesons and/or (anti-)baryons respectively. Mass and flavor of hadrons are determined from the invariant mass and respective flavors of the coalescing partons. Therefore a quark-antiquark pair will be recombined to pions provided di-quark invariant mass is in the proximity of pion mass. Present approach of coalescence is

therefore not exactly similar to those discussed in [14, 17, 18]. Here it allows coalescence of partons with a relatively large momentum difference. To account for the hadronic interactions prior to freeze-out, final state hadrons are then transported through ART model.

AMPT in SM mode with partonic cross section of 6-10 mb provides a good fit to the flow observables at top RHIC energy [33]. While at LHC, with increased beam energy and high initial temperature, data seem to be better reproduced with the choice of a lower parton scattering cross section [34]. In this study we have set scattering cross section to 1.5 mb by tuning  $\alpha_s = 0.33$  and  $\mu = 3.22 \text{ fm}^{-1}$  keeping in mind that this particular choice simultaneously reproduces charged particle multiplicity density and flow coefficients at LHC energy [35, 36]. The parameters for Lund string fragmentation are kept same as that of the default HIJING values corresponding to smaller string tension [36].

## 2.3 Analysis Method

In the present analysis, events generated from the AMPT model for Pb-Pb collisions at  $\sqrt{s} = 2.76 \text{ TeV}$  have been analyzed to calculate inclusive  $p/\pi$  ratio and di-hadron correlation functions between two sets of particles classified as *trigger* and *associated*. The  $p_T$  ranges of trigger and associated particles are  $1.8 < p_T < 3.0 \text{ GeV}/c$  and  $1.0 < p_T < 1.8 \text{ GeV}/c$  respectively and the pseudo-rapidity range of all particles was restricted within  $-1 < \eta < 1$ . The *trigger*  $p_T$  range was chosen in such a way that it contains the region where  $p/\pi$  ratio reaches its maximum. A two dimensional (2-D) correlation function was obtained as a function of the difference in azimuthal angle  $\Delta\phi = \phi_{\text{trigger}} - \phi_{\text{associated}}$  and pseudo-rapidity  $\Delta\eta = \eta_{\text{trigger}} - \eta_{\text{associated}}$ . The per trigger yield of the associated particles in  $\Delta\eta$  and  $\Delta\phi$  was defined as  $\frac{dN_{\text{same}}}{N_{\text{trigger}} d\Delta\eta d\Delta\phi}$  where  $N_{\text{same}}$  is the number of particles associated to the triggers particles ( $N_{\text{trigger}}$ ) on event by event basis.

The correlation function introduced above was corrected for finite acceptance of trigger and associated particles. The acceptance corrected 2D correlation function was obtained by dividing the raw correlations by a correction factor represented as  $B(\Delta\eta) = 1 - |\Delta\eta|/(2\eta_{max})$  [37]. The correction factor has a triangular shape arising out of the limited acceptance in pseudo-rapidity. Uniform  $2\pi$  acceptance in azimuth ensures that no correction is required on  $\Delta\phi$ . Fig. 2.1(a) shows a corrected 2-D correlation function for unidentified particles containing a near side jet-like peak sitting over a flow modulated background.

To obtain the near side jet like yield, the acceptance corrected correlation structure is projected on to the  $\Delta\phi$  axis for  $|\Delta\eta| < 1.2$ . The particles from jet fragments are most likely to be confined in a small angular region provided the width does not get broadened with centrality. To isolate the contribution for near side jet-like correlations, we need to subtract the modulation in  $\Delta\phi$  arising out of the correlation with the event plane as represented by  $v_2, v_3$  or higher harmonics. Flow coefficients can be extracted by fitting the  $\Delta\phi$  projection of the bulk region (large  $\Delta\eta$ ) with  $1 + 2 \sum_1^n v_n^{trig} v_n^{asso} \cos(n\Delta\phi)$  where  $v_n^{trig}, v_n^{asso}$  represent the magnitudes of the  $n^{\text{th}}$  harmonic of flow coefficient for the trigger and associated particles respectively. The Background lying beneath the jet-like peak is modulated by flow correlations dominated by elliptic flow ( $v_2$ ). Contributions from higher order flow harmonics ( $v_3, v_4$ ) were checked and found to be insignificant. In the present analysis instead of calculating different orders of flow harmonics and subtracting separately, the projected  $\Delta\phi$  distributions at larger  $\Delta\eta$  region ( $1.2 < |\Delta\eta| < 1.7$ ) was subtracted from the short-range region. The bulk subtraction by the  $\eta$ -gap method as stated above assumes that the correlations other than jet-like are  $\eta$  independent [38]. 1-D  $\Delta\phi$  correlation functions for the regions  $|\Delta\eta| < 1.2$  and  $1.2 < |\Delta\eta| < 1.7$  are shown in Fig. 2.1(b) and result from the difference of these two distributions was plotted in Fig. 2.1(c).

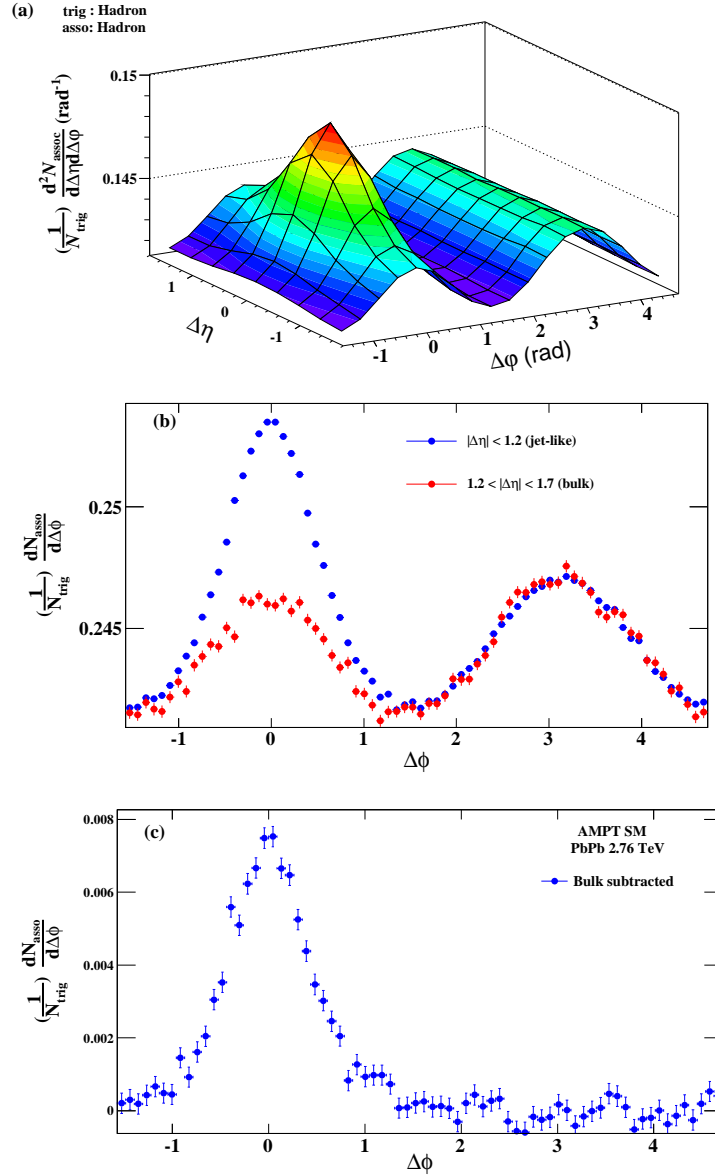


Figure 2.1: (Color online) (a) The 2D correlation function taking unidentified charged hadrons as both trigger and associated particles. Transverse momentum of trigger and associated particles are mentioned in the text. (b)  $\Delta\phi$  projection of the 2D function for different  $\Delta\eta$  regions as indicated in the plot. (c) Near side jet-like region after bulk subtraction

The near side peak centered around  $\Delta\phi = 0$  mainly represents the jet-like correlations and the strength of the correlation (per trigger yield) was calculated by integrating the  $\Delta\phi$  distribution over a range of  $|\Delta\phi| < \pi/2$ .

## 2.4 Results

In this Section, results for angular correlation measurements triggered by identified leading hadrons for Pb-Pb collisions at  $\sqrt{s}=2.76$  TeV are presented. As a first step to test features of coalescence model in the SM version of AMPT, results for particle species dependence of  $p_T$ -differential  $v_2$  for some selected species of hadrons are presented in Section 2.4.1, which is followed by a discussion about the NCQ-scaling of  $v_2(p_T)$  in Section 2.4.2. Finally the results for inclusive baryon-to-meson ratio and angular correlation measurements from both the versions of AMPT model are reported in Section 2.4.3.

### 2.4.1 Particle species dependence of $v_2(p_T)$

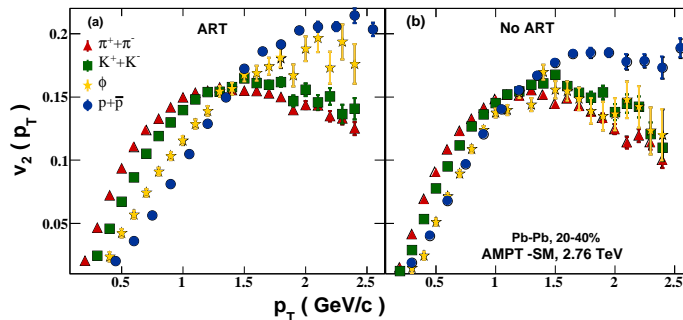


Figure 2.2: (Color online) Elliptic flow parameter  $v_2$  for pions( $\pi^+ + \pi^-$ ), kaons ( $K^+ + K^-$ ) phi mesons( $\phi$ ) and protons ( $p^+ + \bar{p}$ ) as a function of transverse momentum calculated from the SM version of AMPT (a) with hadronic rescattering (ART) (b) without hadronic rescattering (No ART) in 20-40% Pb-Pb collisions at  $\sqrt{s_{NN}} = 2.76$  TeV.

In Fig. 2.2 (a) and (b) we have shown the transverse momentum dependence

of elliptic flow coefficient ( $v_2(p_T)$ ) for pions, kaons,  $\phi$ -mesons and protons in 20-40% Pb-Pb collisions at  $\sqrt{s_{NN}} = 2.76$  TeV from the SM version of AMPT. The elliptic anisotropy or  $v_2$  is characterized by second order Fourier coefficient, and can be written as

$$v_2 = \langle \cos 2(\phi - \Psi) \rangle \quad (2.1)$$

where  $\phi$  is the azimuthal angle of a particle relative to the reaction plane angle ( $\Psi$ ). The angular brackets ( $\langle .. \rangle$ ) stands for average over many particles over large number of events. In the AMPT model the  $\Psi$  is always fixed at  $0^\circ$ .

Fig. 2.2(a) represents flow coefficients calculated with hadronic rescattering (ART) and Fig. 2.2(b) shows the same without hadronic rescattering (No-ART). These results show that without hadronic rescattering (Fig. 2.2(b)) the elliptic flow coefficients ( $v_2(p_T)$ ) exhibit a characteristic mass ordering, i.e,  $v_2^\pi(p_T) > v_2^K(p_T) > v_2^p(p_T) > v_2^\phi(p_T)$  for  $m_\pi < m_K < m_p < m_\phi$  at low  $p_T$  but the mass splitting is small. On the other hand, as shown in Fig. 2.2(a) mass splitting increases as hadronic rescatterings are switched-on.

The observed mass-splitting in AMPT is consistent with Hydrodynamical calculations, which predict a characteristic mass-dependent flow at low- $p_T$  ( $< 2.0$  GeV/c). This mass-ordering is interpreted as a consequence of interplay between elliptic and radial flow. Because of the collective expansion of the system, radial flow generated in the hadronic phase results in a mass-dependent depletion in the particle spectrum at low  $p_T$ . This leads to small values of  $v_2(p_T)$  for heavier particles compared to lighter ones at a given value of  $p_T$ .

However, it is interesting to note that a violation of mass ordering between protons and  $\phi$ -mesons ( $v_2^p(p_T) < v_2^\phi(p_T)$  albeit,  $m_p < m_\phi$ ) below  $p_T$  1.5 GeV/c is observed (Fig. 2.2(a)). This violation was attributed to different hadronic interaction cross-sections for protons and  $\phi$ -mesons. As the interaction cross-

section of  $\phi$ -mesons are much smaller than that of protons, they decouple from the medium earlier and hence  $\phi$ -mesons are negligibly affected by the collective expansion in the hadronic phase. In contrary, because of significant hadronic interactions,  $v_2$  for protons becomes smaller than that of the  $\phi$ -mesons which eventually leads to the breaking of hydrodynamical mass ordering. A clearer picture of this behaviour can be obtained by studying the ratio of  $v_2^\phi(p_T)$  to  $v_2^p(p_T)$  as a function transverse momentum.

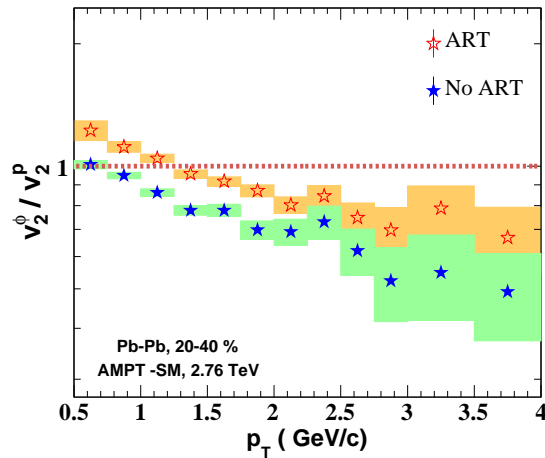


Figure 2.3: (Color online) Ratio of  $v_2^\phi(p_T)/v_2^p(p_T)$  as a function of transverse momentum calculated from the SM version of AMPT (a) with hadronic rescattering (ART) (b) without hadronic rescattering (No-ART) in 20-40% Pb-Pb collisions at  $\sqrt{s_{NN}} = 2.76$  TeV. Filled boxes represent statistical uncertainties

It is evident from Fig. 2.3 that as the time for hadronic interactions is increased from 0.6 fm/c (No-ART) to 30 fm/c (ART) (allowing more hadronic rescatterings) the ratio of  $v_2^\phi(p_T)/v_2^p(p_T)$  exceeds unity below 1.5 GeV/c, implying breakdown of mass ordering.

It is also observed that at intermediate  $p_T$  (see Fig 2.2),  $v_2$  measured for different particles tend to group into two branches according to the particle type, i.e, baryons and mesons. The bifurcation of baryon and meson  $v_2$ , best understood as a manifestation of particle production by quark-recombination,

is indeed observed in the AMPT model calculations.

But surprisingly,  $v_2$  values of  $\phi$ s deviates from the quark-recombination expected baryon-meson grouping. As shown in Fig 2.2,  $v_2$  of  $\phi$ -mesons appear to follow the protons (baryon) in presence hadronic rescattering but falls back on the meson band when hadronic interactions are turned off. A similar observation was also reported in this ALICE publication [49], where it was interpreted as a consequence of strong radial flow that boosts massive hadrons to higher  $p_T$ . As  $\phi$ -mesons and protons have similar masses, they are expected to be boosted equally.

Such observations tend to indicate that baryon-meson grouping could be due to the mass of the particles rather than the number of constituent quarks. However, re-calling that  $\phi$ -mesons do not undergo substantial hadronic rescatterings because of small interaction cross-sections and decouples prior to the build-up of additional radial flow in the hadronic phase, it seems unlikely to be an effect of radial flow alone. It was shown in [48] that the models incorporating  $\phi$ -meson production in the hadronic rescattering stage via  $K\bar{K}$  fusion predict a higher value of  $\phi$ -meson  $v_2$  relative to other mesons. It would be therefore interesting to test the effect of such processes on the elliptic flow of  $\phi$ -mesons.

To investigate, whether  $v_2$  of  $\phi$ -mesons developed at the partonic phase is modified by additional contributions from the hadronic interactions like,  $K\bar{K} \rightarrow \phi$ -meson production,  $v_2$  of  $\phi$ -meson was calculated by turning-off  $K\bar{K}$  coalescence in the hadronic phase. In Fig. 2.4 solid stars represent  $v_2$  of inclusive  $\phi$ -mesons (all  $\phi$ -mesons produced in partonic and hadronic phase) and solid squares represent  $v_2$  of  $\phi$ -mesons excluding those from the  $K\bar{K}$  fusion process (here we call it *primordial*  $\phi$ s). It is interesting to observe that at the end of hadronic rescatterings at 30 fm/c,  $v_2$  of *primordial*  $\phi$ -mesons remain un-

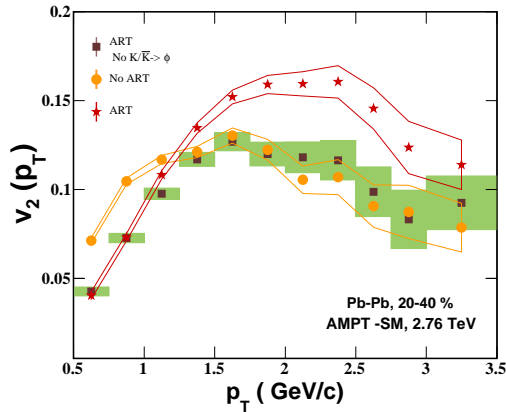


Figure 2.4: (Color online) Transverse momentum dependence  $v_2$  of  $\phi$ -mesons calculated from the SM version of AMPT with ART (solid star), without ART (solid circle) and with ART but  $K\bar{K} \rightarrow \phi$  forbidden (solid square) in 20-40% Pb-Pb collisions at  $\sqrt{s_{NN}} = 2.76$  TeV. Filled boxes and the bands represent statistical uncertainties

changed rather, its values at intermediate  $p_T > 1.5$  GeV/c coincides with the results obtained from the model calculation with hadronic re-scatterings turned-off (No-ART). Therefore it indicates that  $\phi$ -mesons regenerated hadronically by  $K\bar{K}$  fusion in the late hadronic stage may be responsible for pushing the inclusive  $\phi$ -meson  $v_2$  towards the baryon band. But *primordial*  $\phi$ -mesons which are predominantly produced in the partonic phase are least affected by hadronic interactions and follow quark-recombination expected baryon-meson ordering (see Fig. 2.2(b)). It is worth mentioning, despite mass of  $\phi$ -mesons being comparable to that of protons, similarity in the  $v_2(p_T)$  of  $\phi$  (*primordial*) and other lighter mesons ( $\pi, K$ ), as shown in Fig. 2.2(b), indicate that the elliptic flow developed in the partonic phase is inherited by the hadrons via a mechanism of quark recombination.

### 2.4.2 NCQ-scaling of $v_2(p_T)$

Model calculation based on quark recombinations suggests, if anisotropy is developed in the partonic phase,  $v_2^{hadrons}$  would be an additive of its constituent quark- $v_2$ ,  $v_2^{quarks}$ . This naturally follows from the first principle of coalescence formalism which states, the invariant yield of the final state hadrons is proportional to the product of the invariant yield of the constituent partons. Thus, in the region of quark coalescence, yields of mesons and baryons at mid rapidity obey the following relation:

$$\frac{dN^{mesons}}{d^2p_T} \approx \left[ \frac{dN^{quarks}(p_T/2)}{d^2p_T} \right]^2 \quad \frac{dN^{baryons}}{d^2p_T} \approx \left[ \frac{dN^{quarks}(p_T/3)}{d^2p_T} \right]^3 \quad (2.2)$$

In a naive coalescence scenario, assuming the anisotropic phase-space distributions of all partons is dominated by the elliptic component, i.e,  $\frac{dN^{quarks}}{d^2p_T} \sim \frac{dN^{quarks}}{p_T dp_T} [1 + 2v_2^{quarks} \cos(2\phi)]$ ,  $v_2$  of mesons and baryons are related to their respective quark- $v_2$  as:

$$v_2^{mesons}(p_T) = \frac{2v_2^{quark}(p_T/2)}{1 + 2(v_2^{quark}(p_T/2))^2} \quad (2.3)$$

$$v_2^{baryons}(p_T) = \frac{3v_2^{quark}(p_T/3) + 3(v_2^{quark}(p_T/3))^3}{1 + 6(v_2^{quark}(p_T/3))^2}$$

In the limit of small partonic- $v_2$ , i.e  $v_2^{quark} \ll 1$ , elliptic flow of mesons and baryons as obtained from Eq. 2.3 boils down to

$$v_2^{mesons}(p_T) = 2v_2^{quark}(p_T/2) \quad v_2^{baryons}(p_T) = 3v_2^{quark}(p_T/3) \quad (2.4)$$

Under these conditions,  $v_2^{hadrons}/n_q$ , interpreted as  $v_2$  of the constituent partons, tend to follow an universal scaling behaviour in which  $v_2^{baryons}(p_T/3)/3 \approx v_2^{mesons}(p_T/2)/2$ . The transverse momentum region where the aforementioned scaling is valid,  $v_2^{hadrons}/n_q$  for different particles almost merges onto a single

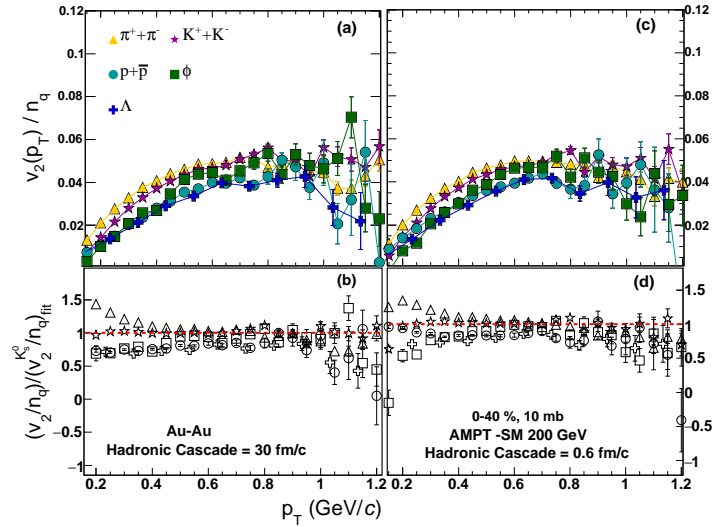


Figure 2.5: (Color online) The  $v_2$  of identified particles for different hadronic cascade time scaled by their respective quark content  $n_q$  plotted as a function of  $p_T/n_q$  for 0-40% Au-Au collisions at  $\sqrt{s_{NN}} = 200$  GeV. Bottom panel shows the ratio with respect to a fit to  $K_s^0$ - $v_2$ .

curve when plotted as a function of  $p_T/n_q$ . Additionally, higher-harmonics are also found to exhibit similar scaling behaviour when scaled by number of constituent quarks [40].

Earlier studies have shown that AMPT-SM has reasonably reproduced the NCQ-scaling of  $v_2$  in min-bias Au-Au collisions at different energies corresponding to the RHIC-BES program [41, 42, 43, 44]. AMPT model in SM condition offer a realistic tool to study the quark-number scaling of  $v_2$  as it incorporates hadron formation by parton coalescence and a relativistic transport calculation to model the dynamics at the later stages of hadronic evolution. In Fig 2.5,  $v_2/n_q$  of some selected hadrons was plotted as a function of  $p_T/n_q$  for 0-40% central Au-Au collisions at 200 GeV. A parton scattering cross-section of 10 mb was chosen to simulate Au-Au events as it was shown to have given reasonable description  $v_2$  and quark-number scaling as well [50].

To estimate the deviation from perfect scaling we have fitted  $v_2$  of  $K_s^0$  by a reco-motivated fitting function [51]:

$$f_{v_2}^{hadron}(n) = \frac{an}{1 + \exp[-(p_T/n - b)/c]} - dn \quad (2.5)$$

where  $a, b, c, d$  are free parameters in the fit-function and  $n$  is the constituent quark-number. Lower panel of Fig 2.5(c,d) shows the ratio of  $v_2/n_q$  of other hadrons to the  $K_s^0$ -fit. It is observed that AMPT calculations satisfy approximate NCQ-scaling within a limit of 10-15% in the range of  $0.4 < p_T/n_q < 0.8$  GeV/c. To investigate the effect of in-medium hadronic re-scatterings on the NCQ-scaling, similar exercise was repeated by restricting hadronic cascade to 0.6 fm/c. At top-RHIC energy, effect of hadronic rescatterings on the NCQ-scaling  $v_2(p_T)$  was observed to be negligible.

Having observed a reasonable agreement between data and AMPT calculations at top-RHIC energy, analogous measurement was carried-out at LHC-energy where a maximum deviation of 20% was reported [49]. Data generated from the string melting version of AMPT using a parton scattering cross-section of 1.5 mb was analysed to calculate NCQ-scaling of  $v_2(p_T)$  for Pb-Pb collisions at 2.76 TeV. The effect of later stage hadronic interactions on the NCQ-scaling of  $v_2(p_T)$  was studied by terminating the hadronic cascade at different times, 0.6, 10 and 30 fm/c.

Fig 2.6 shows  $v_2(p_T)/n_q$  of some selected particles for different hadronic re-scattering time. Unlike RHIC, hadronic rescattering at LHC-energy has significant effect on the NCQ-scaling of  $v_2(p_T)$ . It is evident from Fig 2.6, as the time of re-scattering is reduced from 30 fm/c to 0.6 fm/c, scaling improves. This could be due to the tampering of the  $v_2$  developed at the initial stage by the final state hadronic interactions. Recent hybrid (hydrodynamics + hadronic cascade) model calculations that explain  $v_2$  measurements at LHC, does so by

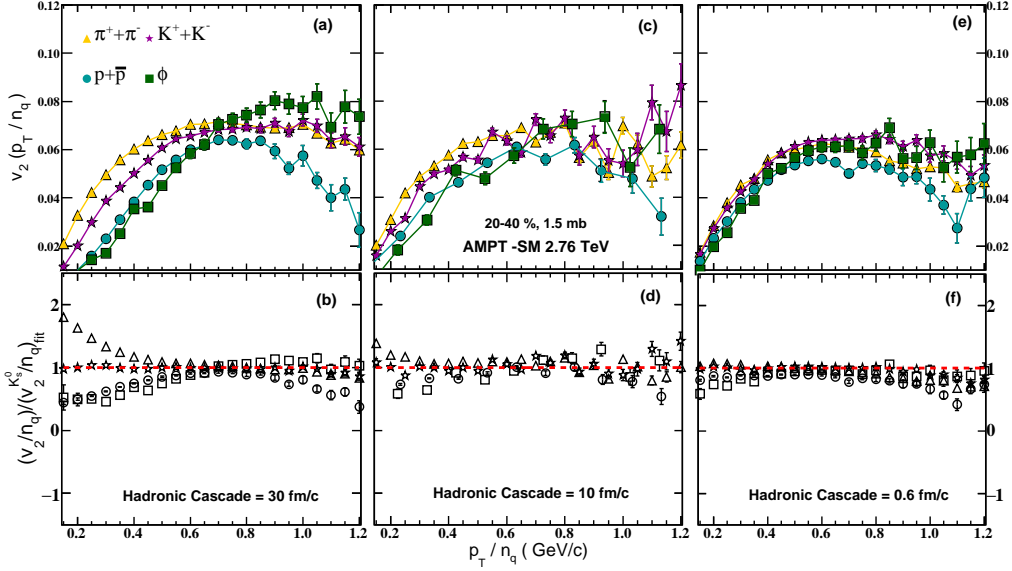


Figure 2.6: (Color online)  $v_2/n_q$  for some identified particles as a function of  $p_T/n_q$  for different hadronic cascade time ((a)30, (c)10 and (e)0.6 fm/c) in 20-40% Pb-Pb collisions at  $\sqrt{s_{NN}} = 2.76$  TeV. Bottom panel shows the ratio with respect to a fit to  $K_s^0$ - $v_2$

re-adjusting the radial and elliptic flow during the hadronic evolution. This indicates, large violation of NCQ-scaling at LHC-energy could be due to the modification of initially developed partonic  $v_2$  by hadronic interactions in the later stages of collision.

When varying the duration of hadronic cascade, it is seen that magnitude of deviation is different for different species. While the large scaling violation of pions is best understood considering the contributions from the resonance decays, little to no effect on kaons could be due to the similarity in  $K^\pm$  and  $K_0^S$   $v_2$  (re-calling  $K_0^S$ - $v_2$  is used as a reference). A large deviation for protons is rather expected because of their heavy mass and strong coupling to the hadronic medium. Whereas, a significant effect on  $\phi$ -mesons  $v_2$  may be attributed to  $\phi$ -meson regeneration from  $K/\bar{K}$ -fusion.

These results are therefore indicative of the fact that, in an ultra-dense

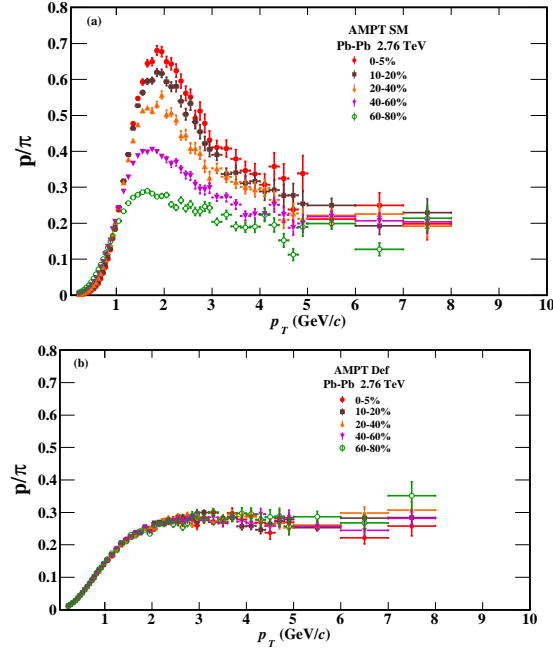


Figure 2.7: (Color online) The ratio of the yields of proton to pion from two versions of AMPT in Pb-Pb collisions at  $\sqrt{s} = 2.76$  TeV. The ratio in SM version (a) shows a clear peak around 2 GeV/c as opposed to the default version (b) which does not show any such peak.

hadronic(also partonic [52]) environment, as it is in nuclei collisions at LHC, NCQ-scaling in  $v_2$  is not a necessary condition for quark coalescence

### 2.4.3 Baryon enhancement and $\Delta\eta - \Delta\phi$ correlations at intermediate $p_T$

Having observed that AMPT-SM reasonably reproduces the basic features of a coalescence model, we now calculate baryon-to-meson ratio and identified trigger particle correlations at intermediate values of  $p_T$  - the main focus of this study.

In Fig. 2.7, We find a clear centrality dependence in  $p/\pi$  enhancement from the SM version of AMPT. Enhancement is found to reach maximum in 0-5% most central collisions at  $\approx 2$  GeV/c. In contrast, the default version shows an initial rise followed by a flat distribution of the ratio.

Having established the best-known feature of the coalescence in AMPT SM model, we obtain two-particle correlations taking leading hadrons as  $\pi$  and  $p/\bar{p}$  in the region where  $p/\pi$  excess has been observed ( $1.8 \leq p_T \leq 3.0$  GeV/ $c$ ). We have extracted the two-particle correlation in  $\Delta\eta$ - $\Delta\phi$  for 5 centrality classes selecting trigger and associated particles in the range  $1.8 \leq p_T \leq 3.0$  GeV/ $c$  and  $1.0 \leq p_T \leq 1.8$  GeV/ $c$  respectively. Fig. 2.8 shows the 2D  $\Delta\eta$ - $\Delta\phi$  correlations for (anti-)proton and pion as triggers. The per-trigger correlation functions

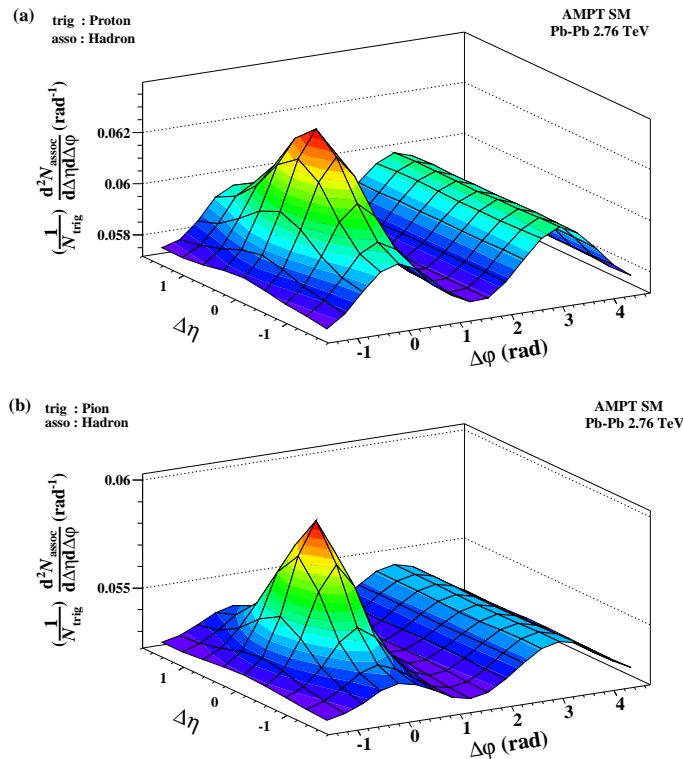


Figure 2.8: (Color online)  $\Delta\eta$ - $\Delta\phi$  correlation function in 40-60 % centrality of Pb-Pb collisions at  $\sqrt{s} = 2.76$  TeV from AMPT SM with proton (a) and pion (b) as trigger particles.

show features typical to the presence of several effects like jet-peaks, harmonic coefficients among others [39]. Near-side jet-like yield associated with pion and (anti-)proton triggered correlation is calculated from the  $\Delta\phi$  projection of background subtracted correlation function in the region  $|\Delta\phi| \leq \pi/2$ . Details of background determination and subtraction have been discussed in the previous

section.

Fig. 2.9 shows the near-side per trigger yields as a function of centrality characterized by the number of participating nucleons ( $N_{part}$ ) from the default and the SM versions. The values from the default version are multiplied by 1.5 for sake of visibility. Yields in the default version are found to be independent of particle species and centrality. In contrast, in AMPT SM, pion triggered yields are systematically higher than yields from (anti-)proton triggers over the entire centrality classes. Interestingly both pion and proton triggered near-side yields exhibit initial rise with centrality till  $N_{part} < 200$ . Beyond that, per trigger yield for pion seems to attain saturation but corresponding yields for (anti-)protons undergo suppression. In Fig. 2.10 the ratio of the yields associated with (anti-)proton and pion triggers ( $Y^{p/\bar{p}}/Y^\pi$ ) as a function  $N_{part}$  have been presented for two different transverse momentum regions. In high  $p_T$  region ( $3.0 \leq p_T \leq 8.0$  GeV/ $c$ ), ratios of yields are consistent with unity and independent of centrality. However, in the  $p_T$  region  $1.8 \leq p_T \leq 3.0$  GeV/ $c$ , ratio dips showing the anticipated dilution. Similar analysis on events generated by the SM version of AMPT for Au-Au collisions at 200 GeV and comparison with results from correlation measurements by the PHENIX Collaboration is represented in Fig. 2.11 It is clearly seen that the model explains dilution trend of the data qualitatively.

## 2.5 Discussion

Having ensured best-known features of coalescence in AMPT model (baryon enhancement and NCQ-scaling), we have measured per-trigger yield of jet-like correlations associated with pion and proton triggers at mid-rapidity over a wide range of centrality in Pb-Pb and Au-Au collisions at  $\sqrt{s}_{NN} = 2760$  GeV and 200

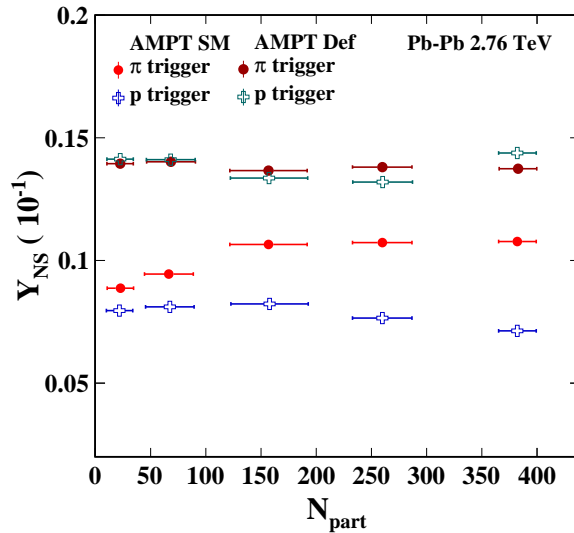


Figure 2.9: (Color online) Centrality dependence of the near side yield from the background subtracted correlation function. The yields from default version of AMPT have been multiplied by 1.5 for better visualisation.

GeV respectively, in the momentum range where baryons are generated in excess of mesons. We have observed a significant enhancement in the jet-like yield associated with leading pions compared to protons. In central A-A collisions, pion trigger yield is much higher than peripheral, while the proton trigger yield exhibits a suppression. The relative enhancement in pion triggered yield could be from the energy dissipation of mini-jet partons and its re-distribution via parton cascade resulting in copious production of softer hadrons aligned to the jet-direction.

However, suppression in proton triggered yield may be attributed to the combined effect of competing processes that involve parton energy loss and quark recombination. If protons are produced dominantly from the recombination of thermal quarks, suppression in proton triggered yield could be naturally expected since hadrons created by recombination of thermal partons are unlikely

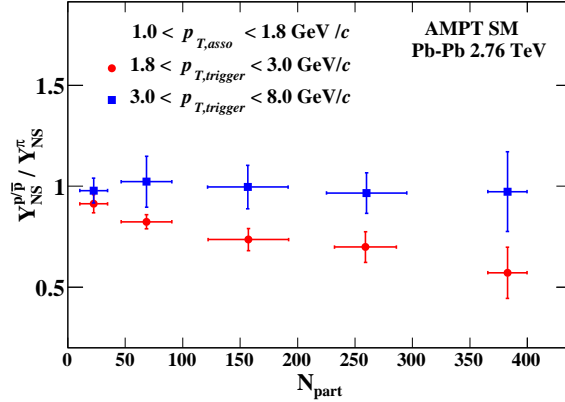


Figure 2.10: (Color online) Ratio of proton trigger yield to pion trigger yield ( $Y^p/Y^\pi$ ) at high and intermediate  $p_{T,trigger}$  regions as indicated in the figure

to have correlated partners in small angular region. This would cause a suppression of proton trigger correlation as function of centrality as baryon generation at intermediate  $p_T$  range is enhanced due to larger contribution thermal quark recombination from peripheral to central collisions.

The ratio of yields in Fig. 2.10 shows a clear dilution in proton triggered correlation from peripheral to central events when trigger particles are chosen from the  $p_T$  region where inclusive  $p/\pi$  ratio has shown enhancement, but no such effect has been observed when trigger particles are chosen from higher  $p_T$  region indicating that contributions from thermal recombination fall off rapidly at larger  $p_T$ .

It is interesting to note that jet-like yield calculated from the default version of AMPT has no or negligible dependence on the choice of trigger species and almost remain unchanged with centrality. A possible reason could be that the initial partonic density in default operation is much less than that in SM version as strings are kept intact. Thus the mini-jet partons during partonic evolution suffers less interaction resulting in negligible energy dissipation. Lack of any significant energy loss may possibly lead to no additional increase in jet-like yield.

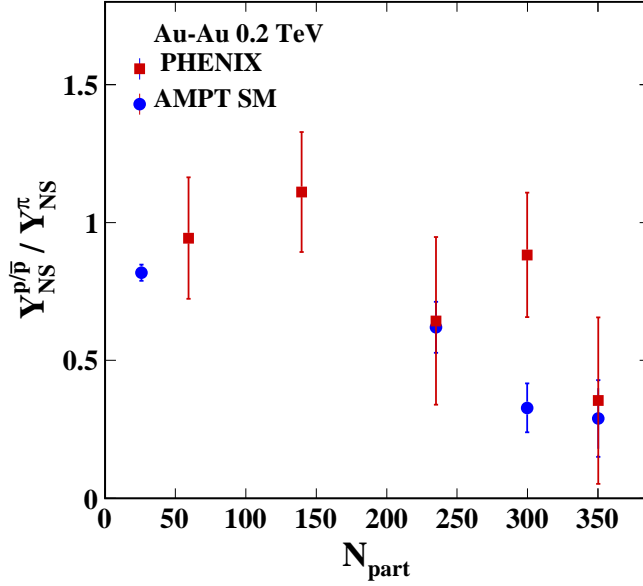


Figure 2.11: (Color online) Ratio of proton trigger yield to pion trigger yield ( $Y^p/Y^\pi$ ) for Au+Au collisions at  $\sqrt{s} = 200$  AGeV, results from PHENIX ([22] superposed).

Our study therefore indicates that the difference in jet yield of baryon-hadron and meson-hadron correlation is an effect of competition between jet-medium interplay and dilution of jet-like yield due to quark recombination. Comparison of our result with data would be interesting as inelastic processes of energy loss are still missing in AMPT.

# Bibliography

- [1] A. Adare et al. (PHENIX Collaboration), Phys. Rev. Lett. 104, 132301 (2010).
- [2] M. Wilde (ALICE Collaboration), Nucl. Phys. A 904-905, 573c (2013) .
- [3] F. Karsch, Nucl. Phys. A 698, 199 (2002) .
- [4] M. Kliemant, et al.: Global Properties of Nuclues-Nuclues Collisions. Lect Notes Phys.(2010) 785, 23-103, and references therein.
- [5] J.L. Klay et al. (STAR Collaboration), Nucl. Phys. A, 715-733 (2003).
- [6] S.S. Adler et al. (PHENIX Collaboration), Phys. Rev. C 69, 034909 (2004).
- [7] B. Ablev et al. (ALICE Collaboration), Phys. Rev. C 88, 044910 (2013).
- [8] S. A. Bass and A. Dumitru, Phys. Rev. C 61, 064909 (2000) .
- [9] D. Teaney, J. Lauret and E. V. Shuryak, Phys. Rev. Lett. 86, 4783 (2001).
- [10] T. Hirano et al. Phys. Rev. C 77, 044909 (2008).
- [11] F. Arleo, Eur. Phys. J. C 61, 603-627 (2009).
- [12] D. d' Enterria and B. Betz, High- $p_T$  Hadron Suppression and Jet Quenching. Lect. Notes. Phys. 785, 285-339 (2010).
- [13] A. Adare et al., Phys. Rev. Lett. 98, 162301 (2007).

- [14] R. Fries, B. Muller, C. Nonaka, and S. Bass, Phys. Rev. Lett. 90, 202303 (2003).
- [15] R. J. Fries, B. Muller, C. Nonaka and S. A. Bass , Phys. Rev. C 68, 044902 (2003).
- [16] R. J. Fries, S. A. Bass and B. Muller, Phys. Rev. Lett. 94., 122301 (2005) .
- [17] V. Greco, C. Ko, and P. Levai, Phys. Rev. Lett. 90, 202302 (2003).
- [18] R. Hwa and C. B. Yang, Phys. Rev. C 70, 024904 (2004).
- [19] C. Adler et al. (PHENIX Collaboration) Phys. Rev. Lett. 90, 082302 (2003).
- [20] K. Aamodt et al. (ALICE Collaboration) Phys. Rev. Lett. 108, 092301 (2012).
- [21] S. Sapeta and U. A. Wiedemann, Eur. Phys. J. C 55, 293-302 (2008).
- [22] S.S. Adler et. al (PHENIX Collaboration) Phys. Rev. C 71, 051902 (2005).
- [23] N. M. Abdelwahab et. al (STAR Collaboration) arXiv:1410.3524 [nucl-ex].
- [24] C. B. Chiu, R. C. Hwa, and C. B. Yang, Phys. Rev. C 78, 044903 (2008).
- [25] J. Adams et. al (STAR Collaboration) Phys. Rev. Lett. 95, 152301 (2005).
- [26] Zi-Wei Lin et. al , Phys. Rev.C 72, 064901 (2005).
- [27] Z. W. Lin and C. M. Ko , Phys. Rev. C. 65, 034904 (2002).
- [28] X. N. Wang and M. Gyulassy, Phys. Rev. D 44, 3501 (1991).
- [29] B. Zhang, Comput. Phys. Commun. 109 (1998) 193 .
- [30] T. Sjostrand, Comput. Phys. Commun. 82, 74 (1994) .
- [31] B. A. Li and C. M. Ko, Phys. Rev. C 52, 2037 (1995).

- [32] B. A. Li, A. T. Sustich, B. Zhang and C. M. Ko, *Int. Jour. Phys. E* 10, 267-352 (2001).
- [33] S. A. Voloshin, *Nucl.Phys. A* 715, 379-388 (2003).
- [34] Subrata Pal and Marcus Bleicher, *Phys. Lett. B* 709, 82-86 (2012).
- [35] E. Abbas et. al (ALICE Collaboration), *Phys. Lett. B* 726, 610-622 (2013).
- [36] J. Xu and C .M. Ko , *Phys. Rev. C* 83, 034904 (2011).
- [37] B. Abelev (ALICE Collaboration) *Physics Letters B* 741, 3850 (2015).
- [38] X. Zhu ( ALICE Collaboration ), arXiv:1311.2394 [hep-ex].
- [39] G.L. Ma et. al, *Phys. Lett. B* 641, 362-367 (2006).
- [40] A. Adare et al., (PHENIX Collaboration) arXiv:1412.1038 [nucl-ex].
- [41] B. Mohanty and N. Xu, *J. Phys. G* 36, 064022 (2009).
- [42] P. P. Bhaduri and S. Chattopadhyay *Phys. Rev. C* 81, 034906 (2010).
- [43] J. H. Chen et al., *Phys. Rev. C* 74, 064902 (2006).
- [44] S. Singha and Md. Nasim, *Phys. Rev. C* 93, 034908 (2016).
- [45] X. Dong, S. Esumi, P. Sorensen, N. Xu, and Z. Xu, *Phys. Lett. B* 597, 328-332 (2004).
- [46] D. Molnar, arXiv:nucl-th/0408044.
- [47] H. Li, L. He, Z.-W. Lin, D. Molnar, F. Wang, and W. Xie, *Phys. Rev. C* 93, 051901(R), (2016).
- [48] B. Mohanty and N. Xu, *J. Phys. G* 36, 064022 (2009).
- [49] B. Abelev et al.,(ALICE Collaboration), *JHEP* 06 190, (2015).

- [50] J. H. Chen et al., Phys. Rev. C 74, 064902 (2006).
- [51] X. Dong, S. Esumi, P. Sorensen, N. Xu, and Z. Xu, Phys. Lett. B 597, 328-332 (2004).
- [52] S. Singha and Md. Nasim, Phys. Rev. C 93, 034908 (2016).

## Chapter 3

# A Large Ion Collider Experiment at LHC

The advent in the accelerator technology over the past several decades has immensely benefited the high energy heavy-ion research across the globe. Around 1986, first attempt was made to pursue research with light-ions in Alternate Gradient Synchrotron (AGS) at Brookhaven National Lab (BNL) and CERN's Super Proton Synchrotron (SPS). The heavy-ion experiments in those era were performed by impinging an accelerated beam of ions on a fixed target. In spite of limitations at the energy frontier, fixed target experiments at CERN SPS had furnished evidences strongly indicating the formation of a new state of matter most likely to comprise of quarks and gluons in a de-confined state. Such initial indications from CERN's SPS provided an impetus to shift from fixed-target to the collider based experiments.

The Relativistic Heavy Ion Collider (RHIC) at BNL was one of the first endeavor to carry out heavy-ion collisions at ultra-relativistic energies. RHIC has been one of the most versatile machine with the ability to collide particles having mass number unity  $A = 1$  (i.e Protons) to mass number  $A = 238$  (i.e Uranium) over a wide range of centre of momentum energy from 7.7 to 200 GeV. A wealth of data acquired during the last 15 years of operation at RHIC, has not only consolidated the claim on the formation of a new state of matter but also

characterised it as a strongly coupled nearly perfect fluid [ref] of quarks and gluons, commonly referred to as sQGP. In September 2008, the Large Hadron Collider (LHC) at CERN became operational, a 10-fold increase in the energy available in the center-of-mass frame was achieved.

This chapter presents a brief overview on different accelerating components at LHC, followed by a detailed discussions of the ALICE detectors, with emphasis on the sub-detectors which are extensively used in this analysis.



Figure 3.1: (Color online) Aerial view of the LHC complex

### 3.1 The Large Hadron Collider (LHC)

Till date, LHC [1, 2] is the largest and the most powerful particle accelerator ever built in the history of mankind. Built with the most sophisticated technologies, the machine itself is an exhibition of engineering marvel. The accelerator complex at CERN houses a series of machines designed to deliver an increasingly higher energy beams. As of today LHC is the final part of this sequence.

The LHC was installed in a tunnel of circumference 27 Km at mean depth of 100 m (varying from 50-175 m), previously used by the Large Electron Positron Collider (LEP). It consist of two hadron synchrotrons capable of accelerating counter-rotating protons or ions and collide them at 4 intersection points, shown

in Fig. 3.1. As per the design, it can collide proton beams at  $\sqrt{s_{NN}} = 14$  TeV and Lead nuclei at  $\sqrt{s_{NN}} = 5.5$  TeV. However, the maximum available energy in center-of-mass frame, as of now, are  $\sqrt{s_{NN}} = 13$  TeV and 5.02 TeV for p-p and Pb-Pb collisions respectively. Detailed scheme of accelerating protons and Pb-ions are discussed in the subsequent sections.

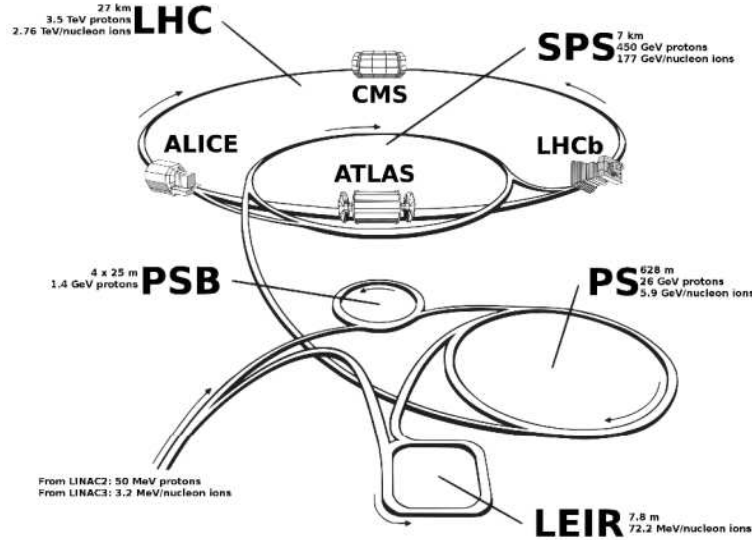


Figure 3.2: (Color online) LHC acceleration and collision schemes [3]

### 3.1.1 Accelerating protons

By stripping orbiting electrons from the hydrogen atoms, protons are extracted and injected into a linear accelerator called LINAC2, where it is accelerated to 50 MeV. The beam is then injected into the Proton Synchrotron Boosters (PSB), that boosts the energy to 1.4 GeV. From the PSB, proton beam is extracted and fed to the the Proton Synchrotron(PS), which accelerates the beam to 25 GeV, followed by its injection into the Super Proton Synchrotron (SPS). At SPS, protons are accelerated to 450 GeV and transferred to the LHC beam lines where it is finally accelerated to a pre-set collision energy.

### 3.1.2 Pb<sup>82+</sup> Source and its acceleration

Acceleration of the Pb-ions starts with the extraction of Pb<sup>29+</sup>-ions from a highly-pure vaporized sample of Lead and accelerating them to 4.2 MeV/nucleon by passing through a linear accelerator called LINAC3. These ions are then passed through a series of carbon foils, where most of them are stripped to Pb<sup>54+</sup>. The bunch of Pb<sup>54+</sup>-ions are then accumulated and accelerated to 72 MeV per nucleon in Low Energy Ion Ring (LEIR). After acceleration in LIER, beam bunches are injected into the PS, where it is further accelerated to 5.9 GeV/nucleon and passed to the SPS. Prior to the acceleration in SPS, Pb<sup>54+</sup>-ions are finally stripped to Pb<sup>82+</sup>. At SPS, ion beams are further accelerated to 177 GeV/nucleon and then sent to LHC for final acceleration.

### 3.1.3 Beam parameters

Besides energy, event or reaction rate of a process strongly depends on the instantaneous luminosity,  $\mathcal{L}$ , the constant of proportionality between event rate( $R$ ) and interaction cross-section ( $\sigma_{int}$ ) of a particular process.

$$R = \sigma_{int} \times \mathcal{L} \tag{3.1}$$

The instantaneous luminosity at the interaction point further depends on several others parameters of the colliding beams like bunch size, bunch spacings and etc. These parameters are however, optimized as per the constrains imposed by the participating experiments to ensure its most efficient performance. At LHC, upto 2808 bunches can be accomodated and accelerated in one beam with bunch spacing of 7 m or 25 nano-seconds. The bunch size may not remain constant over the entire ring. To increase the collision probability, bunch size is squeezed to 16  $\mu\text{m}$  near the collision point and may be stretched

upto 1 mm away from the interaction zone. Given the bunch separation of 25 nano-seconds, the average bunch crossing rate at LHC is 40MHz, although the achieved rate so far is only 31.6 MHz. However, ALICE because of its technical and physics constrains operates at 300 KHz for p-p and 10 KHz for Pb-Pb collisions, respectively. The designed luminosity for p-p collisions is of the order of  $10^{34} \text{ cm}^{-2}\text{s}^{-1}$  but ALICE operates around  $10^{30} \text{ cm}^{-2}\text{s}^{-1}$ . While running with Pb-ions, achieved luminosity was measured to be  $10^{25} \text{ cm}^{-2}\text{s}^{-1}$  in 2010 and  $10^{26} \text{ cm}^{-2}\text{s}^{-1}$  in 2011.

## 3.2 The ALICE Experiment

A Large Ion Collider Experiment (ALICE) [4] at the CERN's Large Hadron Collider (LHC) is an apparatus designed to study and characterize the matter formed in the ultra-relativistic heavy ion collisions. QCD suggests that the energy density achieved in such collisions recreate the situation that had prevailed few  $\mu\text{s}$  after the Big-Bang ,i.e, a deconfined state of quarks and gluons. To gain clear in-sight on the dynamics of the underlying processes involved in such collisions, results from heavy ion collisions are compared and contrasted with p-p and p-A collisions. These control experiments (p-p and p-A collisions) are indeed useful to single-out the signals associated with the formation of Quark-Gluon-Plasma (QGP) from the cold-nuclear matter effects.

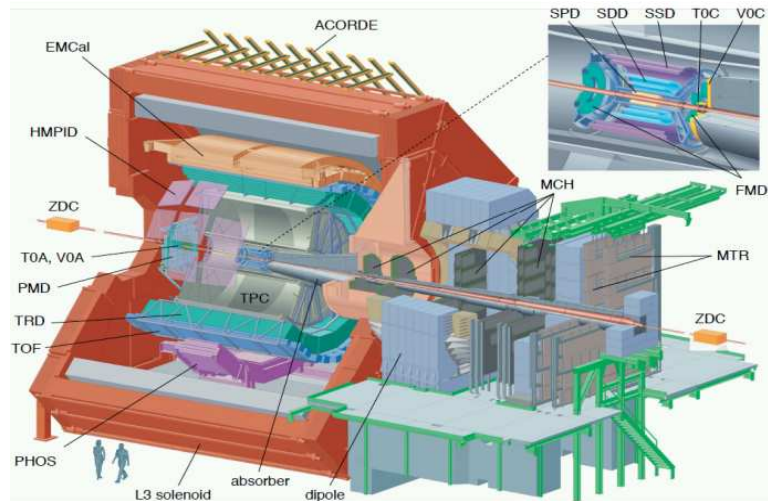


Figure 3.3: (Color online) A schematic view of ALICE detector system. The central-barrel detectors are ITS, TPC, TRD, TOF, PHOS, EMCal, and HMPID. The forward detectors are PMD, FMD, V0 (often called VZERO in the text), T0, ZDC, and the MUON-spectrometers. Photo Courtesy: CERN Document Server (ALICE-PHO-GEN-2012-001-12).

The ALICE apparatus, shown in Fig 3.3, weighs almost 10k tonnes having dimensions of  $16 \times 16 \times 26 \text{ m}^3$ . It has 17 sub-detectors categorized into three parts: central-barrel detectors, forward-detectors and the Muon Spectrometer. The ALICE detectors were designed to sustain high particle multiplicity at the central events without any degradation in performance. With ALICE detectors, it is possible to measure transverse momentum over a large range, from 0.15 GeV/c upto 100 GeV/c and particle identification upto 20 GeV/c. In the sections to follow, over-view on these three categories of the ALICE detectors will be presented.

### 3.2.1 The Central Barrel Detectors

The central barrel detectors of ALICE include the Inner Tracking System (ITS), Time Projection Chamber (TPC), Transition Radiation Detector (TRD), Time-of-Flight (TOF), Photon Spectrometers (PHOS), Electromagnetic Calorimeters (EMCal) and High Momentum Particle Identification Detectors (HMPID)- en-

closed by the L3 solenoidal magnet of magnetic field density (B) 0.5 Tesla. The first four detectors have full  $2\pi$  azimuthal coverage in the mid-rapidity ( $|\eta| < 0.9$ ) but later three are limited in azimuthal acceptance. During the course of running, several modules of PHOS, EMCal and HMPID were added to ensure increased coverage.

The ITS and TPC are the main central barrel detectors responsible for vertex determination, charged particle tracking and particle identification. The six-layered ITS comprises, two layers each of Silicon Pixel Detectors (SPD), Silicon Drift Detector (SDD), and Silicon Strip Detectors (SSD). ITS is followed by TPC, which is a gaseous tracking detector and has a gigantic drift volume of  $90 \text{ m}^3$  filled with a gas mixture of  $\text{Ne}_2\text{-CO}_2\text{-N}_2$ . Just outside TPC is the Transition Radiation Detectors or TRD. TRD is primarily responsible for high  $p_T$  electron-pion discrimination. Electron identification without pion contaminations improve the signal-to-background ratio for heavy vector meson reconstructions ( $J/\Psi, \Upsilon$ , etc) through di-electron decay channels at the central rapidity. TRD being a fast detector, also finds application in the triggering schemes. TRD is immediately followed by the TOF detector, which utilises the excellent timing resolutions of the Multigap Resistive Plate Chambers (MRPC) for particle identification between  $0.6 < p_T < 4 \text{ GeV}/c$ . The EMCal and PHOS is located just behind the cylindrical volume of the TOF diametrically opposite to each other at a radial distance of 4.60 m from the interaction point. EMCal is a Pb-Scintillator sampling calorimeter that has coverage of 0.7 units in  $\eta$  and  $170^\circ$  in azimuth. EMCal enables measurements on jet properties by triggering and full jet-reconstruction. Additionally, it also allows high momentum photon and electron identification. PHOS is an electro-magnetic calorimeter of high-resolution and granularity. Made of fast scintillating  $\text{PbWO}_4$  crystals, it is capable of identifying low- $p_t$  direct photons. Exploiting the granularity of

the detector, high- $p_T$   $\pi^0$ -jet and  $\gamma$ -jet correlations could be measured. Based on Ring Imaging Cherenkov (RICH) counters, HMPID is designed to extend track-by-track basis particle identification of kaons up to 3 GeV/c and of protons upto 5 GeV/c. However, its geometrical acceptance is only 5% of TPC.

### Inner Tracking System -ITS

Due its strategic location close to the beam pipe, the Inner Tracking System (ITS) [5] is primarily responsible for the determination of the primary interaction vertex. Along with precise vertex measurement, ITS is also used for the tracking and particle identification of low momentum tracks that fail to reach TPC. Consisting of six concentric layers of silicon detectors around the beam-pipe, it cover 0.9 units in pseudorapidity and  $2\pi$  in azimuth. As shown in the Fig. 3.4, moving radially outward from the interaction point, the six layered ITS has 2 layers each of SPD, SSD and SDD respectively. Considering high track surface density of  $90 \text{ cm}^{-2}$  in central heavy ion collisions, making detectors with high granularity was the main design requirement. As these detectors are placed in an immediate vicinity of the beam-pipe, they should also be robust and radiation hard.

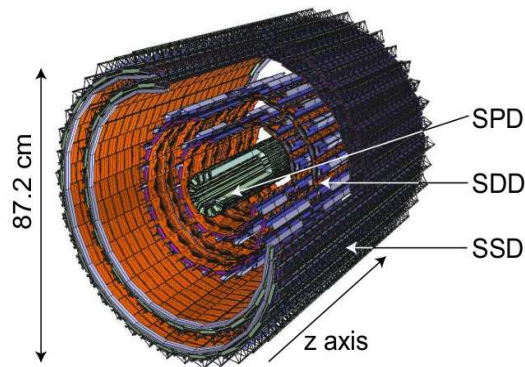


Figure 3.4: (Color online) A schematic view of ALICE-Inner Tracking Chamber. Also shown different sub-layers: SPD, SDD and SSD.

**Silicon Pixel Detector :** The two inner-most layers of ITS consist pixel based silicon detectors, the SPD. Made of 2-dimensional array of  $256 \times 160$  finely segmented silicon pixels, SPD is positioned at radii  $r = 3.9$  cm and  $r = 7.6$  cm. Fine granularity of SPD detectors allow them to localize tracks with maximum spatial resolution of  $12 \mu\text{m}$  in  $r\phi$  and  $100 \mu\text{m}$  in the z-direction. SPD contributes significantly towards precise vertex measurement and impact-parameter measurement of daughter tracks from the weak decay of  $V^0$ , D/B-mesons etc.

**Silicon Drift Detector:** The two intermediate layers of the ITS are SDDs, located at radial distances of  $r=15.0$  cm and  $23.9$  cm from the beam pipe, are particularly used for particle identification using specific energy loss ( $dE/dx$ ) of the tracks passing through the active volume of the detectors. These are finely granulated in one direction and coarse along the other. The position of the track hits in the transverse direction is obtained from the drift-time of electrons to the electrode with respect trigger-time and the z-position of the hits are determined from the centroid of the charge accumulated in the anodes. This offers a hit position resolution of  $38 \mu\text{m}$  in  $r\phi$  and  $28 \mu\text{m}$  in  $Z$ . A precise knowledge of drift-time is extremely necessary for the accurate reconstruction of the tracks in SDD. Given a significant dependence of drift-time on the temperature and humidity across the drift volume in SDD, frequent calibrations are performed to record time-to-time variation in the drift-speed.

**Silicon Strip Detectors:** The last two (fifth and sixth) layers of ITS are made of double-sided silicon strips placed at a radial distance of  $r= 38$  cm and  $43$  cm respectively. These detectors allow hit reconstruction with a spatial resolution of  $20 \mu\text{m}$  in  $r\phi$  and  $830 \mu\text{m}$  in  $Z$ . Like SDD, SPDs are also used for low momentum particle identification exploiting the energy loss ( $dE/dx$ ) information in the detector volume. The outer two layer are also crucial for

ITS-TPC track matching.

Overall, ITS can improve tracking and angular resolution of the tracks. Most of the low momentum tracks (tracklets) that fail to reach TPC are reconstructed in ITS thereby allowing physics measurements at low  $p_T$  below 200 MeV. Use of silicon based detectors also facilitates maintaining a low material budget. The total material budget of ITS is 7.18% of a radiation length.

### **Time Projection Chamber -TPC**

The Time Projection Chamber or TPC [6] is at the heart of the ALICE central-barrel detectors, dedicated towards tracking and particle identification. Placed coaxially with beam-pipe and ITS, TPC active volume has its inner radius located at 80 cm and the outer radius at approx 250 cm from the beam pipe. The length of the chamber is about 510 cm along the beam pipe. The TPC covers a phase space of  $|\eta| < 0.9$  and full range of azimuth. 90 m<sup>3</sup> drift tube of TPC was filled with Ne/CO<sub>2</sub>/N<sub>2</sub> (85.7%/9.5%/4.8%) gas mixture till 2010. In 2011, new gas-mixture (Ne:CO<sub>2</sub> :: 90%:10%) was introduced to decrease the gas-gain and prevent frequent detector-breakdown during high luminosity runs targeted at that period. Extensive investigation has resulted in the choice of the gas mixture that has been optimised further to render low electron diffusion, small space charge effect and low material budget in order to ensure good momentum resolution, high rate handling capacity, minimal re-scattering and secondary particle generation. The material contained in the field cage and the drift gas contributes to material budget equivalent to 3% of a radiation length at the mid-rapidity and 4% towards edges.

A central electrode charged to 100 KV, shown in Fig. 3.5, separates the TPC-drift volume into two segments and provide an axial uniform electric field

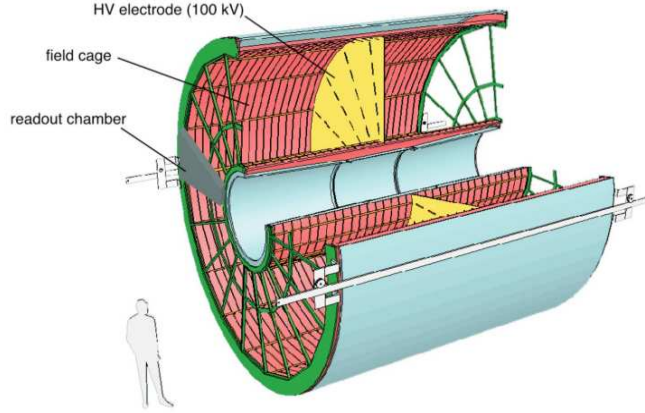


Figure 3.5: (Color online) Schematics of ALICE-TPC [7]

of 400 V/cm. The charged particles traversing through the detector active volume ionises the gas. Electrons liberated in the process of ionisation drift towards the end-plates over a distance of 250 cm at an average drift velocity of 2.7 cm/s. The end-plates are equipped with segmented anode read-out pads placed in MWPCs to collect the electrons. The x-y positions of the tracks can be directly obtained from the hit points on the anode-pads at the end plates. The z-coordinates of the trajectory (along the beam-axis) are reconstructed based on the arrival time of the signal at the anode plane relative to some external reference say collision time of the beams from the LHC-clock. The position resolution of the detector is about 800-1100  $\mu\text{m}$  in the transverse plane and 1100-1250  $\mu\text{m}$  along the z-direction.

The specific energy loss of the particles ( $dE/dx$ ) in the detector active volume can be measured from the charge collected in TPC read-out pads. There are 159 read-out pads thus, the maximum number of charged clusters for a track within the TPC active volume can go upto 159. Knowing the particle momentum,  $\langle dE/dx \rangle$  information can be used to trace the mass of the particles from the Bethe-Block formula [8, 9].

$$\langle dE/dx \rangle = \frac{C_1}{\beta^2} [\ln(C_2 \beta^2 \gamma^2) - \beta^2 + C_3] \quad (3.2)$$

Parameters in the equations have their usual meanings. A typical momentum dependence of  $\langle dE/dx \rangle$  spectrum has different bands that correspond to particles with different masses as shown in left panel of Fig 3.6. The number-of-sigma ( $n\sigma^i$ ) deviation of the  $\langle dE/dx \rangle$  response of each particles from the standard Bethe-Block curve of a particular mass hypothesis is used for particle discrimination.

$$n\sigma^i = \frac{\frac{dE}{dx} - \langle \frac{dE^i}{dx} \rangle}{\sigma^i}, i = \pi, k, p/\bar{p}. \quad (3.3)$$

TPC-alone can reconstruct tracks from  $p_T$  100 MeV/c to 100 GeV/c with a momentum resolution varying from 2% to 20%. Coupled with other sub-detectors of ALICE (ITS and TRD), TPC can offer a better momentum resolution (upto 10%) for charged tracks up to 100 GeV/c. Additionally, a good dE/dx resolution assists particle identification down to 0.3 GeV/c in  $p_T$ . MC simulations with proper implementation of geometrical-acceptance, gas-gain, etc indicate that reconstruction efficiency of stand-alone TPC can be as good as 90 % even in the most central collisions. However, a large drift time of 90  $\mu$ s restricts ALICE from participating in high-luminosity runs.

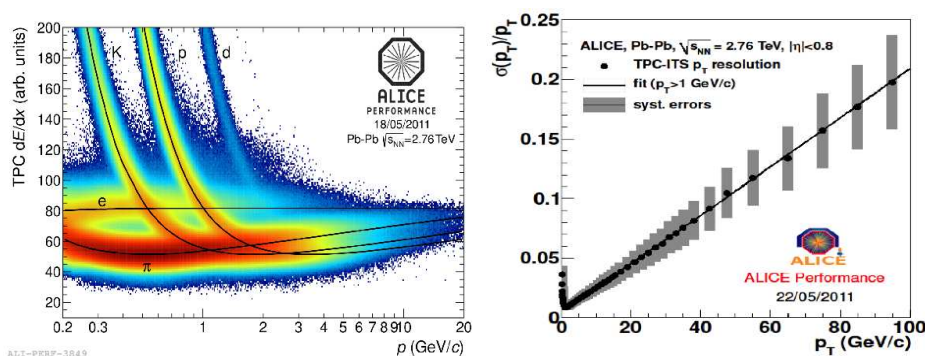


Figure 3.6: (Color online) **Left:** Energy-loss,  $\frac{dE}{dx}$  versus momentum ( $p$ ) in the TPC active volume. For each particle there is a distinctly separated band below  $p_T < 1$  GeV/c which merges at higher  $p_T$ . **Right:** Transverse momentum resolution of the tracks upto 100 GeV/c for ITS-TPC combined tracks [10].

### Time of Flight -TOF

Identification of particles over a wide momentum range is essential to address various physics processes associated with the formation QGP. To extend particle identification with better separation at moderate  $p_T$ , ALICE uses the technique of time-of-flight measurement [11, 12]. The time-of-flight, as the name suggests, it involves measurement of time ( $t$ ) taken by a particle to traverse a known trajectory of length  $L$ . For a given track length and momentum, mass of the particle can be calculated using the relation:

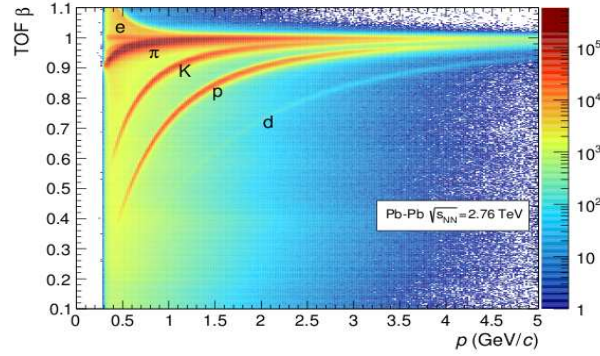


Figure 3.7: (Color online) TOF  $\beta = v/c = L/tc$  distribution as measured by ALICE-TOF detector as a function of momentum in Pb-Pb collisions at  $\sqrt{s_{NN}} = 2.76$  TeV

$$m = \sqrt{\frac{p^2}{c^2} \left( \frac{c^2 t^2}{L^2} - 1 \right)} = \sqrt{\frac{p^2}{c^2} (1/\beta^2 - 1)} \quad (3.4)$$

Therefore two particles of unequal masses ( $m_1$  and  $m_2$ ) but same momentum ( $p$ ) will cover the same length  $L$  in a time difference of:

$$t_2 - t_1 = \frac{L}{2c} \left( \frac{m_1^2 c^2 - m_2^2 c^2}{p^2} \right) \quad (3.5)$$

This difference in the time-of-flight is exploited to discriminate particles with different masses. The capability of TOF detectors to separate particles appreciably depend on the time difference ( $t_2 - t_1$ ) and the intrinsic time resolutions

( $\delta t$ ) of the detectors as:

$$\frac{t_2 - t_1}{\delta t} = n\sigma \quad (3.6)$$

The number-of-standard deviations( $n\sigma$ ) in the time-of-flight difference between two particles is used as a parameter for particle identification. Fig 3.7 illustrates the separation among the particles as a function of momentum.

Detectors with good time resolution, less than 100ps, are required to ensure a  $3\sigma$   $\pi/K$  and  $K/p$  separation upto 2.5 GeV/c and 4 GeV/c respectively. The Multi Gap Resistive Plate Chambers (MRPC), offering a time resolution of 80ps, are found to be the most suitable detector to serve the purpose within the affordable cost .

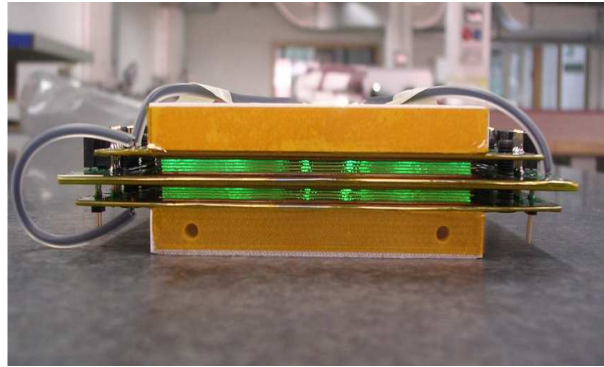


Figure 3.8: (Color online) Photograph of 10-gap glass-MRPC used to fabricate ALICE-TOF [13].

120 cm long 10-gap glass MRPC strips are the basic constituents of the ALICE-TOF detector. Designed in a cylindrical form, inner and outer radii are located at 370 cm and 399 cm from the beam axis respectively and covers a full azimuth in the central rapidity with a polar acceptance of 0.9 unit in  $|\eta|$ . The radial stretch of the ALICE-TOF amounts to almost 29.5% of a radiation length.

To cope with the high multiplicity environment in central collisions, detectors are highly segmented to have low occupancy around 12%. The active area of the detector is filled with a gas mixture: 90% Freon, 5% SF<sub>6</sub> and 5% Iso-butane. Results from the test beam with 6 GeV/c pions show that MRPCs achieve an efficiency of 99.9% and time resolution better than 40 ps at an voltage of  $\pm 6$  KV across the gas-gap. However, the over-all resolution of the TOF detectors also includes the jitter in the initial time ( $t_0$ ) information available from the T0 detector. Thus the overall time resolution of ALICE-TOF is given by:  $\sigma_{TOF} = \sqrt{\sigma_{intrinsic}^2 + \sigma_{t0}^2}$

In Pb-Pb collisions,  $\sigma_{TOF}$  was found to be 86 ps. Hence a maximum separation of  $2\sigma$  between protons and kaons could be reached even at a momentum of 5 GeV/c. Combined with TPC and ITS, TOF can facilitate event by event identification of pure samples of  $\pi^\pm$ , K and protons upto a momentum range of 4 GeV/c [14].

### 3.2.2 The Forward Detectors

The Forward detectors in ALICE comprise of pre-shower Photon Multiplicity Detector (PMD), silicon-based Forward Multiplicity Detector (FMD) quartz Cherenkov detector T0, plastic scintillator based V0 and Zero Degree Calorimeter (ZDC).

The main objective of the ALICE Forward Multiplicity Detector or FMD [16] is to allow determination of charged particle multiplicity at forward rapidity. The FMD consists of 5 rings of silicon strip detectors placed around the beam-pipe. 3 inner rings (FMD1i, FMD2i and FMD3i) contain 10 hexagonal silicon cells while, 2 outer rings (FMD2o and FMD3o) have 20 such silicon sensors segmented into 2 sectors. Each sector is further cut into strips at constant

radius. Beside extending multiplicity measurement at large forward rapidity, it also caters the need for independent and reliable measurement of event plane inclination. The pseudorapidity coverage of the detector on either side of the interaction point is  $-3.4 \leq \eta \leq -1.7$  and  $-1.7 \leq \eta \leq 5.0$ , respectively. Combination of FMD and ITS allow charged particle counting over an extraordinarily large pseudorapidity range ( $-3.4 \leq \eta \leq 5.0$ ).

The Photon Multiplicity Detector or PMD [18, 19] was installed with an aim to measure photons at the forward rapidity. Located at 3.67 m from the interaction point towards the A side of the ALICE it covers pseudo-rapidity  $2.3 < \eta < 3.9$  and full azimuth. It consists of two planes, Charged Particle Veto (CPV) and Pre-Shower (PRE). A Pb-converter is sandwiched between these two planes. The thickness of the Pb-converter has been optimised to deliver high photon-conversion efficiency but low transverse shower spread. The working principle of the detector is similar to a proportional counter. The active volume of the detector is filled with Ar-CO<sub>2</sub> gas mixture in a proportion of 70:30 by weight. Each PMD plane has 24 modules and each module has 4608 honeycomb cells.

The T0 [16] detector consists of two arrays (T0A and T0C) of Cherenkov counter placed assymmetrically with respect to the interaction point (IP). The T0A is positioned 3.75 m from the IP on the A-side of the ALICE and T0C is located 7.27 m from the IP towards the C-side of the ALICE. T0 detectors provide the start time of the collision with a precision of 25 ps. This time is also used as a start time by the TOF detector for the time-of-flight measurement of the particles.

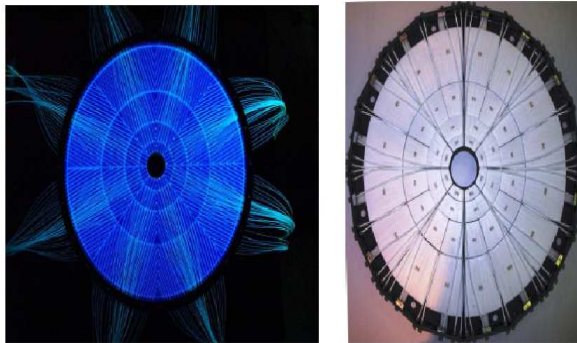


Figure 3.9: (Color online) V0 detector modules [17]

### VZERO (V0)

Similar to T0, plastic scintillator based two arrays of VZERO(V0) detectors (V0A and V0C) [23, 16] (see Fig. 3.9) are also placed asymmetrically on the either side of the IP. Located at a distance of 340 cm towards the A side of the IP, V0A measures the charged particles in the pseudo-rapidity window of  $2.8 \leq \eta \leq 5.1$ . The V0C is located on the other side of IP at a distance of 90 cm and measures charged particle multiplicity in  $-3.7 \leq \eta \leq -1.7$ . Each detector has 4 rings and each ring is segmented into 8 sectors, making an overall 32 segmented counters. The information from this detector is particularly used for triggering, centrality estimation and backgrounds rejection. Triggering logics are designed using the timing information from V0A and V0C detectors to reject backgrounds originating from the interactions other than beam-beam. Furthermore, the energy deposited in the V0 scintillators can be used to extract charged particle multiplicity in the detector coverage. The calibrated V0 signal amplitudes (V0A + V0C) has been used for centrality estimation. It allows centrality estimation with a resolution of  $\approx 0.5\%$  and  $2\%$  [15] in most central and peripheral event classes, respectively. A comparison of centrality resolutions for different centrality estimators are shown in Fig. 3.10 as a function of the centrality percentile. V0 is used as a default centrality estimator in ALICE as

it allows most precise centrality measurement over the entire range. Moderate granularity in the azimuthal direction ( $45^\circ$ ) also allows experimental estimation of event plane inclination using the V0 detectors.

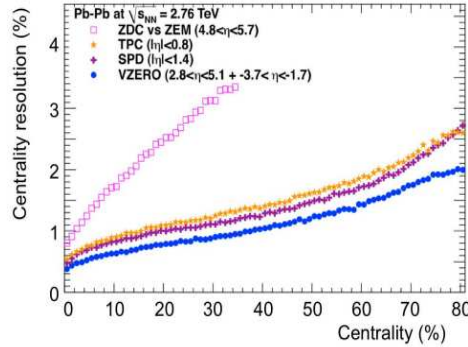


Figure 3.10: (Color online) Comparison of centrality percentile resolutions as a function of centrality for different centrality estimators used in ALICE [15]

Last but not the least the Zero Degree Calorimeter (ZDC) [20], located at 114m on either side of the interaction point IP, measures the energy deposited by the spectator nucleons. Amount of energy deposited in ZDCs is directly related to the spectator nucleon number which are not involved in the interaction. This information can also be utilized for centrality estimation in nuclear collisions [15]. The ZDC in ALICE consist of a hadronic and an electromagnetic calorimeter. The hadronic ZDC comprises two tungsten-quartz neutron calorimeter (ZN) and two brass-quartz proton calorimeter (ZP). Since the spectator protons are deflected by the magnetic elements along the beam-line, ZP is placed outside the beam-line on the side where positive particles are deflected.

### 3.2.3 The Muon Spectrometers

The purpose of the MUON spectrometer is to measure all states of quarkonia and  $\phi$ -mesons in forward rapidity. The spectrometer is located on the C side of the IP and designed to track muons in the pseudorapidity range  $-4 < \eta < -2.5$

with full azimuthal acceptance. The tracking stations allow hit reconstruction with a spatial resolution of  $100 \mu\text{m}$ . The major components of the spectrometer schematically represented in Fig. 3.11, are discussed below:

- A conical shaped front end absorber made of carbon, concrete and steel to stop hadrons and photons and allow muon with momentum  $> 4 \text{ GeV}/c$  to pass through.
- A large dipole magnet (magnetic field of  $3\text{Tm}$ ) installed perpendicular to beam-pipe outside the L3 magnet, that allows tracking and momentum reconstruction of the muon candidates.
- Highly granular 5 tracking stations: two in front of the dipole magnet, one at its center and two behind it.
- A 1.2 m iron wall acts as an additional muon filtering.
- Four planes of trigger chamber made of Resistive Plate Chamber.
- An additional shielding of dense absorber material, covering the entire spectrometer, protects it from particles and secondaries at forward rapidity.

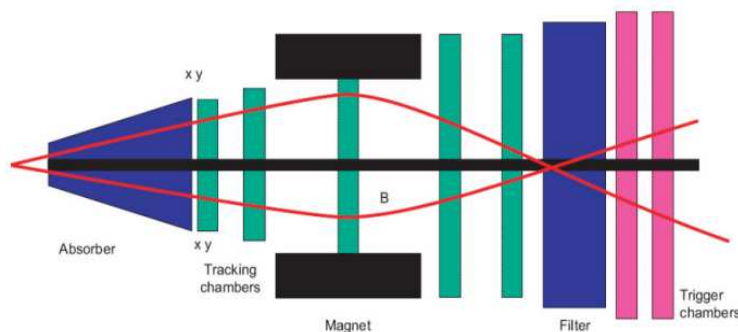


Figure 3.11: (Color online) A schematic diagram of Muon Spectrometer [21, 22]

### 3.2.4 Data Reconstruction

Particles produced in a collision leave their “foot-prints” in the detector active volume in terms of series of electrical signals. These signals are further digitized and each collision event is registered as a sequence of numerous digital information. Several peta-bytes of data are generated annually at LHC and it is a real challenge to manage this colossal amount of data. Thus the experiments adopt different schemes for data compression which includes triggering, background-rejection, on-line/off-line reconstruction and curtailing the storage of redundant information. Among these, background suppression and triggering are crucial steps in data acquisition as it can eliminate several events which are not of “physics interest”. Thus it allows most efficient usage of the computing resources and prevents wastage of computing time. In this section, we will discuss about the ALICE trigger system, background-rejection, event reconstructions (tracking and vertexing) and finally the ALICE computing system.

#### ALICE Online Trigger

The process of isolating events of particular interest without recording huge amount of unnecessary data is known as triggering. The Central Trigger Processor (CTP) [24] of ALICE is responsible for generating trigger decisions based on the inputs from trigger-detectors and bunch filling schemes of LHC. The ALICE CTP has been designed to operate between 8 KHz and 300 KHz depending on the luminosity and size of colliding elements (A-A or p-p). A three-level trigger system has been implemented in ALICE called as Level 0 (L0), Level 1 (L1) and Level 2 (L2), respectively. The L0 triggers are generated  $\approx 0.9 \mu\text{s}$  after the collision using V0, T0, EMCal, PHOS and MTR. The decision based on L0 trigger is sent to the participating detectors asking them to initiate the readout

process. The Level 1 (L1) trigger decisions are realized  $6.5 \mu\text{s}$  after L0 which opens-up the gates for buffering the data to the detector Front End Electronics (FEE). The delay between L1 and L0 is caused due to difference in the response time of trigger detectors coupled with the busy time of the detectors that receives the trigger. L2 decisions are made almost  $\approx 90 \mu\text{s}$  after the collision, which corresponds to drift-time in TPC. It initiates parallel data transmission to DAQ and HLT, and may also be used for rejecting pile-up events. Since CTP is based on clusters (group of detectors), busy time of the slowest detector limits the busy time of the cluster. ALICE trigger electronics is built-on ALTERA Cyclone Field Programmable Logic Arrays (FPGAs), which allows additional flexibility to modify trigger logics whenever needed.

### **Background Rejection**

Events recorded after being allowed by the trigger conditions may be contaminated by some fake events that do not originate from beam-beam interactions. A major source of such background is the inelastic beam-gas interactions near the IP. Even with sophisticated vacuum techniques, it is not possible to drain out all gas molecules from the beam pipe. As a result, interaction of Pb-beam and residual gas molecules may occur close to IP which may be recorded as a real event. It may be noted that this source of background increases with beam-luminosity and strongly depends on the residual gas content in the beam pipe. Another source of background may arise out of the interactions between beam and the mechanical structure of the accelerators. All these background can be singled-out using the timing information from the V0 detectors [23] as shown in Fig 3.12.

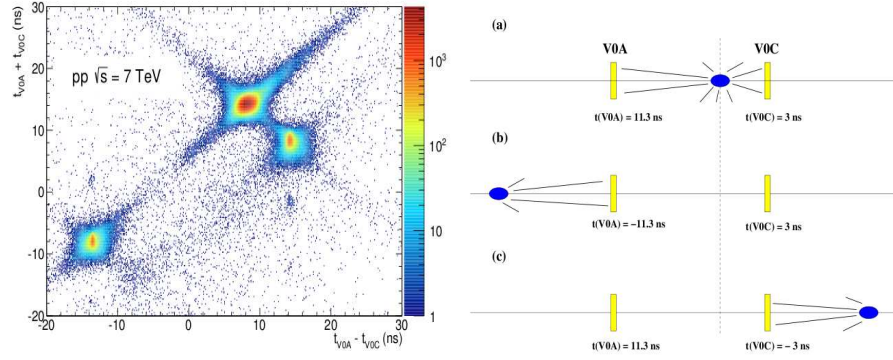


Figure 3.12: (Color online) **Left**: Three distinct event classes can be characterized using correlations between sum and difference of signal time information available from V0A and V0C : **a**) collision at IP (8.3 ns, 14.3 ns), **b**) beam background behind V0A (-14.3 ns, -8.3 ns) and **c**) beam background V0C (14.3 ns, 8.3 ns). **Right**: A schematic diagram showing arrival time of particles from different locations of beam induced interactions to the V0 detectors [25].

### Event Reconstruction - Tracking and Vertexing

An event may be thought as a collection of hits or clusters left by the particles traversing through the detector active volume. Tracking is a process or technique of connecting these disjoint points in order to reconstruct the trajectory of the particles and extract its kinematics as well. An accurate tracking is of great importance as it affects determination of the momentum of the particles and extrapolation to far-away detectors which could provide information on the particle identification. This section focuses on the track finding strategy in the ALICE central barrel.

The first step in tracking starts with clustering of the in each of the detectors. Each cluster is loaded with information regarding its spatial location with respect to a pre-defined origin, signal strength, signal time and their corresponding errors. The clusters from first two layer in ITS are used to determine the location of preliminary primary vertex followed by tracking in TPC using *Kalman Filter* [26] technique and track-matching with other central-barrel detectors.

- **Vertex Determination** The primary vertex determination in ALICE is performed by using the cluster information from first two layers in ITS (SPD). Each tracklet, ( pair of space points in first two layers are connected by a line) is propagated to the nominal interaction point (IP) and made to converge. A primary vertex is defined as a point close to IP where most of the tracklets converge. In case of pile-up, this process is repeated and at each iteration, clusters which have been already assigned to a vertex are discarded. However, for final vertexing, global tracks from ITS and TPC after final reconstruction instead of tracklets are extrapolated and made to converge around the IP.
- **Tracking** A three stage tracking strategy has been adopted by ALICE known as inward-outward-inward scheme [27, 28]. Tracking starts from the two outer-layers of TPC and the parameters from the outer most space-points are considered as *seeds* for the track-finding algorithm. *Seeds* are now propagated in-ward and at each step, nearest clusters are assigned depending on their proximity with the previous *seed* prolonged to the recent layer. Whenever such clusters are found track parameters and covariance matrices are updated. Tracks with less than 20 space-points (clusters) or which miss more that 50% of the total clusters expected at its location are rejected. Accepted tracks are then propagated to the inner radius of TPC. Tracks reconstructed in the TPC are then extrapolated to the outer layer of the ITS which tries to extend the tracks close to the primary vertex. Once the track reconstruction in TPC-ITS is performed, a stand-alone track reconstruction in the ITS is carried out for those tracks (tracklets) which fail to reach TPC.

In the second tracking stage, tracks are refitted using Kalmann Filter in the outward direction (vertex to TPC) taking the clusters obtained in the

previous stage. At this stage, track-length integrals and expected flight-time of different particles are calculated and updated for particle identification with TOF. Tracks that could reach TOF are matched with TOF-clusters and propagated further for track matching in EMCAL, PHOS and HMPID.

At the final stage, again KF fitting is done in outward-inward approach, starting from the TRD. Position, direction, track-curvature and their respective covariance matrices are re-evaluated and updated. For kinematical variables, parameters obtained from the track-fitting not beyond the outer radius of TPC is only taken into account.

### **ALICE Offline Analysis**

Reconstructed events are stored as Event Summary Data (ESD) which contain all information about an event both at event and track level like: trigger type, vertex information, centrality/multiplicity and track by track preliminary PID from various detectors. However, ESD files are bulky and not efficient to handle. The data files can be compressed to Analysis Object Data (AOD). AODs are derived from ESD through re-filtering. Tracks satisfying some pre-defined sets of cuts are kept, rest are deleted. AOD may contain some advanced level information like reconstructed jets from different algorithms. Thus, running on AODs reduce the I/O overhead. Analysis can be performed on both AODs and ESDs, while ESDs are flexible, AODs are computationally efficient.

Analyses are generally performed on a distributed computing facility called GRID. The ALICE environment software AliEn acts as an interface with the GRID. The job scheduler in AliEn divides a job into multiple sub-jobs and process them parallelly in short time. ALICE has also developed Light weight Environment for Grid Operation (LEGO) framework which allows simultaneous

execution of jobs from different users intending to run their analyses on same sets of events. Thus data from the storage devices are read just once. This increases CPU efficiency as multiple users can run their jobs using the same computing resources. Additionally, end users are not exposed to grid complexity and hassles of job submission, resubmission, end-of run report, as these are done automatically and designated support personnels handle issues related to bug fixing of the grid environment.

# Bibliography

- [1] The CERN Large Hadron Collider : Accelerator and Experiments, Volume 1, Breskin, Amos (ed.) and Voss, Rudiger (ed.) (CERN), 2009.
- [2] The CERN Large Hadron Collider : Accelerator and Experiments, Volume 2, Breskin, Amos (ed.) and Voss, Rudiger (ed.) (CERN), 2009.
- [3] J. J. Goodson and R. McCarthy, *Search for Supersymmetry in States with Large Missing Transverse Momentum and Three Leptons including a Z-Boson*. PhD thesis, Stony Brook U., May, 2012. Presented 17 Apr 2012.
- [4] The ALICE experiment at the CERN LHC, K. Aamodt et al., [ALICE Col- laboration], J. Instrum. 3, S08002 (2008).
- [5] ALICE Inner Tracking System (ITS): Technical Design Report, CERN-LHCC-99-012, <http://edms.cern.ch/file/398932/1>.
- [6] ALICE Time Projection Chamber: Technical Design Report, CERN-LHCC-2000-001, <http://cdsweb.cern.ch/record/451098>.
- [7] Saikat Biswas (for the ALICE Collaboration), arXiv:1511.04988, 2015.
- [8] H. Bethe. Zur Theorie des Durchgangs schneller Korpuskularstrahlen durch Materie. Annalen der Physik, 397(3):325400, (1930).
- [9] F. Bloch. Zur Bremsung rasch bewegter Teilchen beim Durchgang durch Ma- terie. Annalen der Physik, 408(3):285320, (1933).

- [10] ALICE Collaboration: "Performance of the ALICE Experiment at the CERN LHC" *Int. J. Mod. Phys. A* 29, 1430044 (2014) .
- [11] ALICE Time-Of-Flight system (TOF): Technical Design Report, CERN-LHCC-2000-012, <http://cdsweb.cern.ch/record/430132>.
- [12] ALICE Time-Of-Flight system (TOF): addendum to the technical design report, CERN-LHCC- 2002-016, <http://cdsweb.cern.ch/record/545834>.
- [13] Roberto Preghenella thesis, CERN-THESIS-2009-206.
- [14] C. Lippmann, *Nuclear Instruments and Methods in Physics Research A* 666, 148172 (2012).
- [15] B. Abelev et al. (ALICE Collaboration), *Phys. Rev. C* 88, 044909 (2013).
- [16] ALICE forward detectors: FMD, T0 and V0: Technical Design Report, CERN-LHCC-2004-025, <http://cdsweb.cern.ch/record/781854>.
- [17] Chiara Bianchin thesis, CERN-THESIS-2012-033.
- [18] ALICE Photon Multiplicity Detector (PMD): Technical Design Report, CERN-LHCC-99-032, <http://cdsweb.cern.ch/record/451099>.
- [19] ALICE Photon Multiplicity Detector (PMD): addendum to the technical design report, CERN-LHCC-2003-038, <http://cdsweb.cern.ch/record/642177>.
- [20] ALICE Zero-Degree Calorimeter (ZDC): Technical Design Report, CERN-LHCC-99-005, <http://cdsweb.cern.ch/record/381433>.
- [21] ALICE dimuon forward spectrometer: Technical Design Report, CERN-LHCC-99-022, <http://cdsweb.cern.ch/record/401974>.

- [22] ALICE dimuon forward spectrometer: addendum to the Technical Design Report, CERN-LHCC- 2000-046, <http://cdsweb.cern.ch/record/494265>
- [23] E. Abbas et al. (ALICE Collaboration), JINST 8, P10016 (2013), arXiv:1306.3130.
- [24] CTP Preliminary Design Review, <http://www.ep.ph.bham.ac.uk/user/pedja/alice>.
- [25] J. Conrad , J. G. Contreras, and C. E. Jørgensen, Minimum Bias Triggers in ProtonProton Collisions with the VZERO and Silicon Pixel Detectors ALICE-INT-2005-025 version 1.0.
- [26] R. Frühwirth, Nucl. Instrum. Meth. A 262, 444–450 (1987).
- [27] M. Ivanov, I. Belikov, P. Hristov, T. Kuhr and K. Safarik, Nucl. Instr. and Meth. A 566, 70 (2006).
- [28] Y. Belikov, M. Ivanov, K. Safarik and J. Bracinik, eConf C0303241, TULT011 (2003), arXiv:physics/0306108.

# Chapter 4

## Dihadron Correlation Measurements

This chapter discusses the details of the dihadron correlation measurements for charged particles produced in Pb-Pb collisions at center-of-mass energy ( $\sqrt{s_{NN}}$ ) of 2.76 TeV, as a function of collision centrality over a wide kinematic range in *trigger* and *associated* particle transverse momentum ( $p_T$ ). The data and track selection criteria, used in this analysis are discussed in Section 4.1., followed by discussions about the construction of two particle angular correlations as function of  $\Delta\eta$ - $\Delta\phi$  in Section 4.2. In Section 4.3, effects of detector in-efficiencies on the correlation function and the associated corrections are described. A Monte Carlo closure test performed, to check the reliability of these correction factors is also described here. Section 4.3 discusses the extraction of near side (NS) jet yield from the corrected correlation function. Finally, the results on the centrality dependence of associated near side jet-like yields in a variety of *trigger* and *associated* particles  $p_T$  ( $p_{T,trig}, p_{T,asso}$ ) bins are presented in sections 4.4 and 4.5, respectively.

## 4.1 Data sample and Event Selection

The angular correlation measurements are performed on Pb-Pb dataset recorded during the low luminosity heavy ion runs in November-December 2010 at  $\sqrt{s_{\text{NN}}} = 2.76$  TeV with the ALICE detector. The minimum bias pass2 LHC10h-AOD086 Pb-Pb events are chosen from run numbers flagged as **good runs** in the ALICE Run Condition Table (RCT) [1]. Additional offline event filtering is applied by requiring the location of the reconstructed primary vertex ( $|V_z|$ ) within 10 cm from the nominal interaction point along the beam line. If the interaction points are located far away from the center of the detector, many particles will be produced outside the normal detector acceptance. Thus, the restriction imposed on the z-vertex position of the events, ensure an uniform pseudorapidity coverage of the tracks within the TPC active volume ( $|\eta| < 0.8$ ) and also optimally rejects the beam-induced background events. Fig.4.1 shows the z-position distribution of the reconstructed primary vertex for all minimum biased Pb-Pb events.

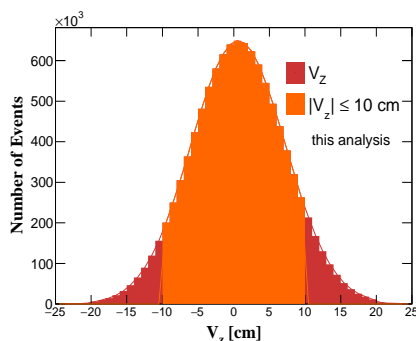


Figure 4.1: (Color online) The Z-vertex position distribution of all minimum biased events, and those selected for this analysis are shown in different colors

In heavy ion collisions, it is customary to segregate events in centrality classes based on the number of charged particles produced in a collision. In ALICE, event centrality is estimated using the Glauber model fit to the mul-

tiplicity distributions in the VZERO (V0) scintillator detectors (V0A+V0C). Events collected after the pile-up rejection and Z-vertex cuts are further analyzed to determine outliers in the multiplicity correlation between several pairs of detectors (like, SPD and V0, TPC and V0, etc). The events lying outside the respective correlation bands may be rejected as an additional process of cleaning. Rest of the good quality events are then classified in centrality percentiles, starting at 100% with most peripheral collision to 0% as most central. The V0 detectors are used as primary centrality estimator in the ALICE, which allows centrality determination over a range of 0% to 100% with a resolution upto 2%.

Number of events survived after each of these selection-cuts are graphically represented in Fig. 4.2. As the beam luminosity was low over the entire data-taking period, the event pile-up rate was measured to be less than  $10^{-4}$ . Almost 8.5 million good events, satisfying all relevant event selection criteria have been analyzed.

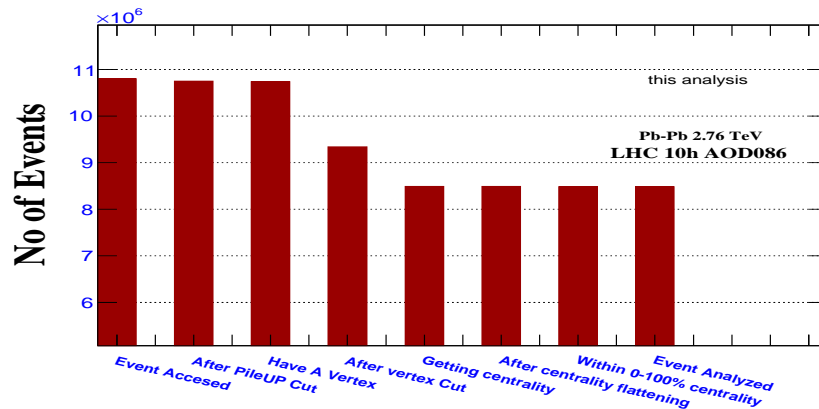


Figure 4.2: (Color online) An event statistics bar-chart: showing number of events collected after each selection cuts

### 4.1.1 Track Selection

For each event, a set of selection criteria has been imposed to eliminate tracks of poor-quality and to select primary charged particles not originating from weak decays or other secondary interactions. Beside rejecting the poor quality tracks, the cut values have been optimized to achieve best momentum resolution and efficient particle identification. The track selection criteria used in this analysis are enlisted below: This set of cuts values are used for track reconstruction

Track parameters	Cut values
Transverse momentum	$p_T > 0.15 \text{ GeV}/c$
$ \eta $	$< 0.8$
Number of TPC clusters	$> 70$ (out-of 159)
$\chi^2$ per clusters in TPC	$< 4$
$\chi^2$ per clusters in ITS	$< 36$
Reject kink daughters	Yes
Distance of closest approach (dca) with respect to a primary vertex $dca_{xy}$ ( $dca_z$ )	$< 2.4 \text{ cm}$ (3.2 cm).
Constrained to SPD vertex	$(\frac{\Delta_{xy}}{d_{xy}})^2 + (\frac{\Delta_{xy}}{d_{xy}})^2 < 1$
ITS refit	Yes
TPC refit	Yes

Table 4.1: Summary of hybrid track cuts

in ITS and TPC. In case a track could not be reconstructed in both ITS and TPC because of dead area or sector gaps in the former, standalone TPC tracks are used instead. Since several sectors of ITS (mainly SPD) were not functional during the data taking period, this approach of track selection has been improvised to mitigate the in-efficiency, whenever a common tracking in both ITS and TPC is required.

Tracks, satisfying the selection criteria mentioned in the table 4.1 are known as *hybrid tracks* [2], as different types of tracks are combined in a way to ensure flat  $\eta, \phi$  distributions (see Fig. 4.4). Since correlation analyses are shown to

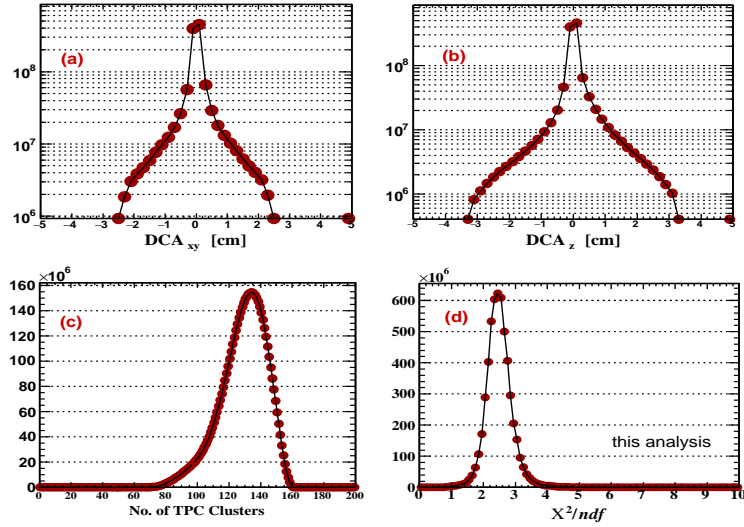


Figure 4.3: (Color online) Parameters after filtering through hybrid track cuts: a)  $DCA_{xy}$  distribution, b)  $DCA_z$  distribution, c) number of TPC clusters and, d) TPC  $\chi^2$  /per cluster distribution. Y-axis of all plots represents counts in arbitrary unit (a.u.)

have benefited from the uniform  $\eta, \phi$ -acceptance [3, 4], the hybrid track cuts are chosen as a default track selection criteria for correlation analyses in ALICE.

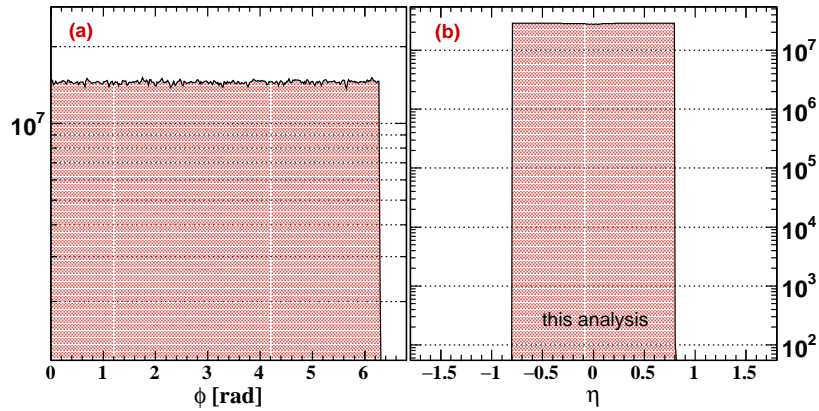


Figure 4.4: (Color online)  $\eta, \phi$  distributions of hybrid tracks

## 4.2 Making of Correlation Function

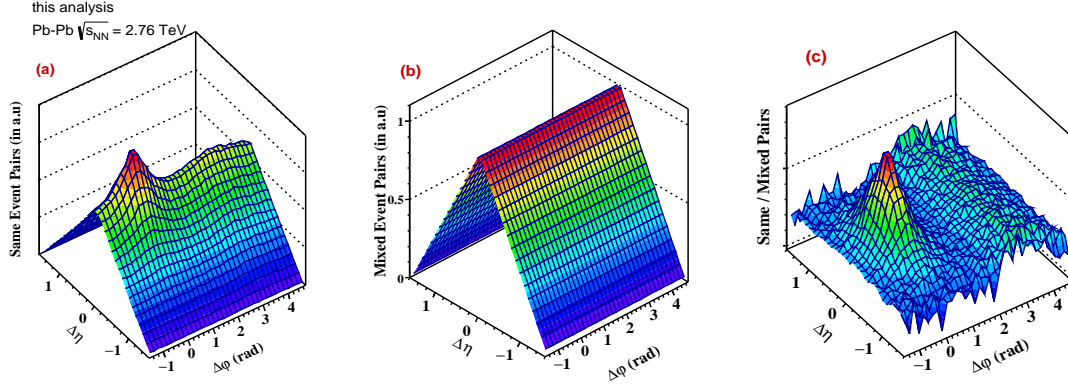


Figure 4.5: (Color online) (a) Same event pairs ( $S(\Delta\eta, \Delta\phi)$ ), (b) mixed event pairs ( $B(\Delta\eta, \Delta\phi)$ ) and (c) ratio of same event over mixed event pairs

Tracks satisfying the selection criteria are classified as *trigger* and *associated* particles. In a given centrality, two-particle angular correlation between pairs of trigger and associated charged particles are measured as a function of their azimuthal ( $\Delta\phi = \phi_{trig} - \phi_{asso}$ ) and pseudorapidity ( $\Delta\eta = \eta_{trig} - \eta_{asso}$ ) differences in the species range of  $p_{T,trig}$  and  $p_{T,asso}$ . The differential yield of associated particles, per-trigger-particle is defined as:

$$\frac{1}{N_{trig}} \frac{d^2 N^{asso}}{d\Delta\eta d\Delta\phi} = \frac{S(\Delta\eta, \Delta\phi)}{B(\Delta\eta, \Delta\phi)} \quad (4.1)$$

where  $N^{asso}$  represents the number of hadron pairs associated to the total number of trigger particles,  $N_{trig}$ . The function  $S(\Delta\eta, \Delta\phi)$ , shown in Fig. 4.5(a), is the differential measure of per-trigger-particle distribution of associated hadrons in the same event, i.e:

$$S(\Delta\eta, \Delta\phi) = \frac{1}{N_{trig}} \frac{d^2 N^{same}}{d\Delta\eta, d\Delta\phi} \quad (4.2)$$

This quantity is calculated in a specified range of  $p_{T,trig}$ ,  $p_{T,asso}$  and centrality ( $C$ ) by looping over all pairs of particles, and filling in two multidimensional

histograms:

$$N^{pair}(\Delta\eta, \Delta\phi, p_{T,trig}, p_{T,asso}, C, Z_{vtx}) \text{ and } N^{trig}(p_{T,trig}, C, Z_{vtx}). \quad (4.3)$$

While  $N^{pair}$  stores the  $\Delta\eta, \Delta\phi$  distribution of each pairs as a function of  $p_{T,trig}$ ,  $p_{T,asso}$ ,  $C$  and  $Z_{vtx}$ ; the transverse momentum distribution of trigger particles are kept as a function centrality ( $C$ ) and Z-vertex position ( $Z_{vtx}$ ) in  $N^{trig}$ . Before computing the ratio in Eqn. 4.2, number of trigger particles and  $\Delta\eta, \Delta\phi$  distribution of particle-pairs are projected onto  $Z_{vtx}$  bins, over a given range  $p_{T,trig}, p_{T,asso}$  and  $C$  in the following way:

$$N^{*pair}(\Delta\eta, \Delta\phi, Z_{vtx}) = \int dp_{T,trig} \int dp_{T,asso} \int dC N^{pair} \quad (4.4)$$

$$N^{*trig}(Z_{vtx}) = \int dp_{T,trig} \int dC N^{trig} \quad (4.5)$$

To correct for pair-acceptance and pair-efficiency, a mixed event technique is employed. In this process, a background distribution:

$$B(\Delta\eta, \Delta\phi) = \alpha \frac{d^2 N^{mixed}}{d\Delta\phi d\Delta\eta} \quad (4.6)$$

is constructed by pairing the trigger and associated particles from different events, where  $N^{mixed}$  denotes the number of such mixed event pairs. In absence of any physical correlations, this mixed event distribution as shown in Fig. 4.5(b), should reflect the effects of random combinatorics and finite geometric acceptance of the track pairs.

An *On the fly* event mixing technique is adopted in this analysis, which requires an event pool where tracks from the previous events are cached in bins of centrality (the centrality bin width varies from 1% to 10% between central and peripheral events respectively) and Z-vertex position (2 cm width). The mixed event correlations are constructed by pairing tracks from two different

events belonging to same centrality class and within the same Z-vertex interval of 2 cm. The mixing of events are started when there are at least 5 events in a bin.

The factor  $\alpha$  in Eq. 4.5 is used to normalize the background distribution, such that  $B(\Delta\eta, \Delta\phi)$  is unity at  $\Delta\eta, \Delta\phi \approx 0$ . This condition is imposed because both particles in the pair have same geometric acceptance as they are travelling in the same direction.

Like same event, mixed event pairs are also calculated following the same process as illustrated in the Eq. 4.3 and 4.4, respectively. The correlation functions are then calculated for each Z-vertex bin as:

$$\frac{d^2 N^{*raw}}{d\Delta\phi d\Delta\eta} = \frac{1}{N_{trig}^*(Z)} \frac{N^{*same}(\Delta\eta, \Delta\phi, Z_{vtx})}{N^{*mixed}(\Delta\eta, \Delta\phi, Z_{vtx})} \quad (4.7)$$

Finally, the acceptance corrected correlation function (see Fig.4.5(c)) is derived by weighted average of raw correlation functions over all bins of Z-vertex position as given below:

$$\frac{d^2 N^{*asso}}{d\Delta\phi d\Delta\eta} = \frac{1}{\sum_z N_{trig}^*(Z)} \sum N_{trig}^*(Z) \frac{d^2 N^{*raw}}{d\Delta\phi d\Delta\eta}(\Delta\eta, \Delta\phi, Z_{vtx}) \quad (4.8)$$

here the number of trigger particles in each  $Z_{vtx}$  bin,  $N_{trig}^*(Z)$ , is the weight factor.

### 4.3 Corrections

Although the mixed event technique corrects for the pair acceptance, but only partially corrects for detector effects due to finite reconstruction efficiency. A combined single-particle efficiency  $\varepsilon(p_T, \eta, Z_{vtx})$  is calculated as a function of transverse momentum, pseudorapidity and Z-vertex position from the HIJING Monte Carlo (MC) simulations implementing the most realistic ALICE detector

set-up using GEANT3. When filling the same and mixed distributions, both particles in a pair are weighted by their respective correction factors.

### 4.3.1 Efficiency correction

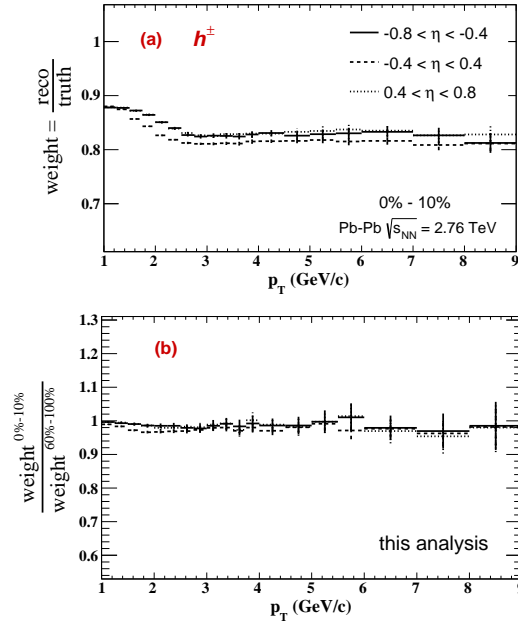


Figure 4.6: (Color online) **(a)** The transverse momentum dependence of single particle efficiency in 0%-10% central events. **(b)** the ratio of the same in central and peripheral events, for Pb-Pb collisions at 2.76 TeV

In upper panel of Fig. 4.6,  $p_T$  dependence of single particle tracking efficiency of primary charged particles for 0%-10% most central collisions are plotted in different  $\eta$  intervals. The single particle efficiency ( $\varepsilon(p_T)$ ) is defined as the ratio of number of reconstructed primary tracks to the total number of primary tracks at the generator level. The tracking efficiency increases sharply upto 1 GeV/c (not shown in Fig. 4.6), followed by a drop until it reaches a value of 82%-83% around 3 GeV/c. The efficiency was measured to be marginally lower in the central region of the detector ( $|\eta| < 0.4$ ) compared to its outer edges ( $|\eta| > 0.4$ ). This is because of shorter track length or smaller number of TPC

cluster, number of tracks satisfying the selection criteria is relatively less in the central region than the outer edges of the detector. However, the correction factors do not exhibit any significant multiplicity dependence as represented in the ratio of weight factors between central (0%-10%) and peripheral (60%-100%) in 4.6(b). The contamination factors are also calculated and found to be  $< 4\%$  for  $p_T > 2-3$  GeV/c.

The correction factors, thus obtained, are applied as weight to each particles. Therefore, each hadron pair is weighted by the product of combined correction factors for two particles, that is,  $N_{pair}^{corrected} = N_{pair}^{raw} \times \frac{1}{\epsilon^{trig} \times \epsilon^{asso}}$ .

### 4.3.2 Two-Track Efficiency

If two tracks have angular separation less than the spatial resolution of the TPC, each of them may not be reconstructed as two distinct tracks because of significant sharing of TPC clusters. This is called track merging effect, which reduces the number of pairs observed at small opening angles and resulting in an artificial dip in the correlation function at  $\Delta\eta, \Delta\phi=(0,0)$ . This generally happens when TPC track pairs are having very small momentum difference or for very high  $p_T$  track pairs which punches through the detector without bending.

This detector in-efficiency is corrected by applying a two-track efficiency cut, that removes track pairs potentially affected by two-track resolution effect. This cut is applied on both same and mixed event distributions, and therefore in the ratio of same over mixed event, two-track effects are eliminated (see Fig. 4.9).

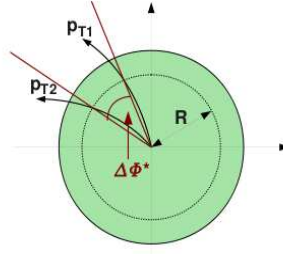


Figure 4.7: (Color online) Two track separation in the transverse plane

The method of designing this cut is based on the angular separation between two tracks within the TPC's active volume, shown in Fig. 4.7. The angular difference is calculated from track parameters using the relation given below:

$$\Delta\phi^* = \Delta\phi + \arcsin\frac{z_1 e B_z r}{2p_{T,1}} - \arcsin\frac{z_1 e B_z r}{2p_{T,1}} \quad (4.9)$$

where  $e$  is the elementary charge,  $B_z$  the magnetic field in  $z$  direction,  $z$  the sign of the particle, and  $r$  the radius in the TPC. For the magnetic field of 0.5 T,  $r$  is in metre and  $p_T$  is in GeV/c,  $B_z e = 0.075$ . The two  $\arcsin$  terms accounts for the curvature in the magnetic field. Thus  $\Delta\phi^*$  is the angular separation in  $\phi$  at the radius  $r$ . The cut is imposed on the  $\Delta\phi_{min}^*$ , the minimum azimuthal distance between two tracks at the same radius after considering the bending in the magnetic field. When constructing the same-event and mixed-event pairs, the trigger and associated particles having separation in  $|\Delta\phi_{min}^*| < 0.02$  and  $|\Delta\eta| < 0.02$  are rejected. Fig. 4.8 shows the 2-D  $\Delta\eta, \Delta\phi$  distributions of same and mixed event pairs with (**bottom**) and without (**top**) applying the two-track cut.

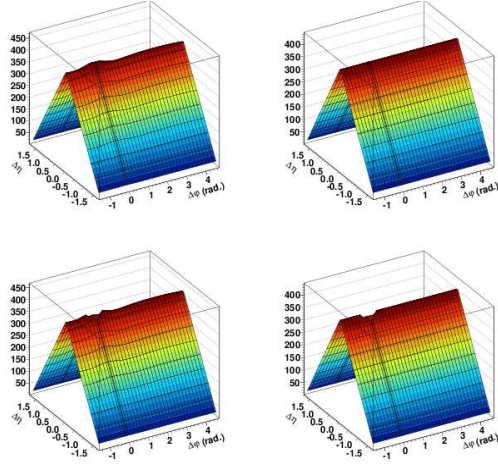


Figure 4.8: (Color online) Same and mixed event distributions **top**: without and **bottom**: with applying the two-track efficiency cut [21].

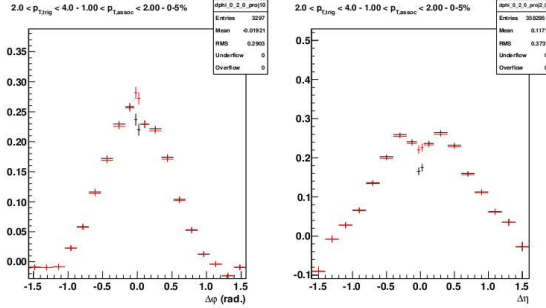


Figure 4.9: (Color online) 1-D  $\Delta\phi$  ( $\Delta\eta$ ) projections without (**black**) and with (**red**) applying the two-track efficiency cut [21].

Also shown in Fig. 4.9 is the 1-D  $\Delta\phi$  ( $\Delta\eta$ ) distributions the correlation function before and after the pair resolution effects are corrected. The peak shape is seen to recover after the two-track resolution cuts are applied. However, it must be noted, when two-track cuts are applied, mixed event normalization at  $\Delta\eta, \Delta\phi=(0,0)$  need to be modified. In this case, the normalization const  $\alpha$  is determined by averaging over the flat  $\Delta\phi$  distribution at  $\Delta\eta = 0$  by excluding the bin content at  $\Delta\eta, \Delta\phi=(0,0)$ .

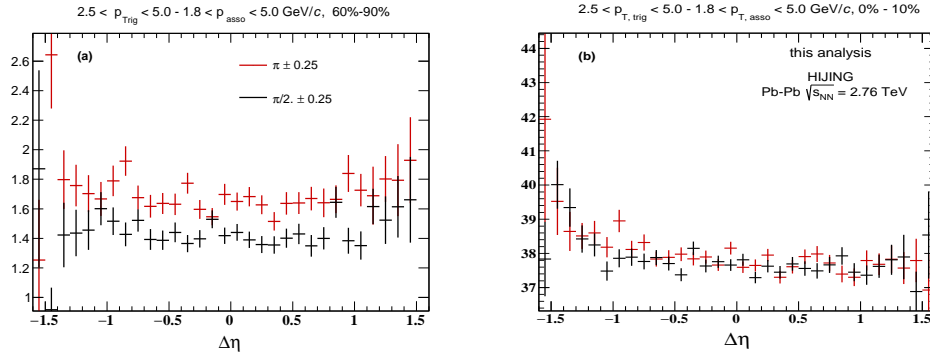


Figure 4.10: (Color online) 1-D  $\Delta\eta$  projections of the correlation function at  $\Delta\phi = \pi \pm 0.25$  (red) and  $\Delta\phi = \pi/2 \pm 0.25$  (black) in different  $p_{T,trig}$ ,  $p_{T,asso}$ , and centrality classes ((a) 60%-90% and (b) 0%-10%), obtained from MC HIJING simulations. Plot shows *wing*-like structures at large  $\Delta\eta$

### 4.3.3 Wing Effect

The mixed-event corrected correlation function exhibits a systematic increase or decrease at large  $|\Delta\eta|$ . This curving away of correlation structure towards the large  $|\Delta\eta|$  as shown in the Fig. 4.10 is referred to as the *Wing effect*. Previous studies have shown that such structures might appear if events are mixed in the wide bins of centrality or Z-vertex. To minimise this wing effect, it was suggested to perform the mixed event correlations in a narrow centrality and Z-vertex bin, as used in this analysis.

However, the bin sizes are still finite and residual effect persists. Fig. 4.10 shows  $\Delta\eta$  projection of 2D correlation function at  $\Delta\phi = \pi \pm 0.25$  and  $\Delta\phi = \pi/2 \pm 0.25$  for two centrality bins (0%-10% and 60%-90%) from the HIJING MC simulations. In principle, the correlation structures are expected to be flat in these regions, but we observe a symmetric or asymmetric rise of correlation functions towards the larger values of  $\Delta\eta$ .

Considering no physics effects are responsible for the origin of wings, a force full flattening of the correlation structure has been done at  $\Delta\phi = \pi/2$  using

a weight factor estimated from the ratio of the correlation functions at  $\Delta\phi = \pi/2 \pm 0.25$  and a constant. The same correlation function, shown in Fig 4.11, is flat over  $\Delta\eta$  after the residual wing effect corrections are implemented.

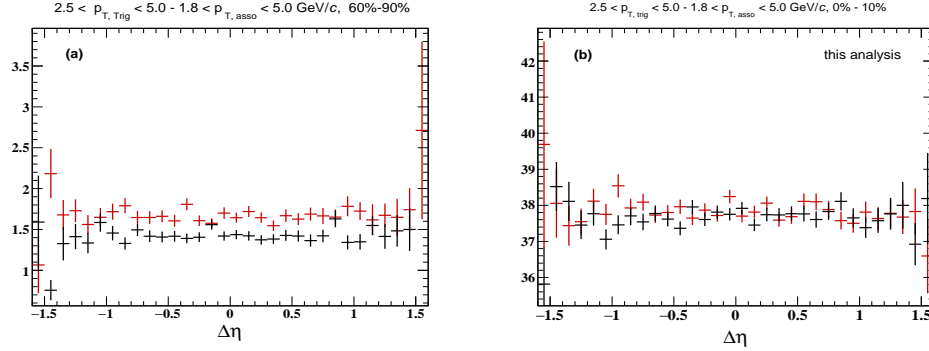


Figure 4.11: (Color online) 1-D  $\Delta\eta$  projections of the correlation function at  $\Delta\phi = \pi \pm 0.25$  (red) and  $\Delta\phi = \pi/2 \pm 0.25$  (black) in different  $p_{T,trig}$ ,  $p_{T,asso}$ , and centrality classes ((a) 60%-90% and (b) 0%-10%), obtained from MC HIJING simulations, after *wing* corrections.

The wing effect is found to be rather more pronounced in data (see Fig Fig. 4.12). Nevertheless, it could be reasonably corrected (flattened) invoking the above mentioned correction strategy.

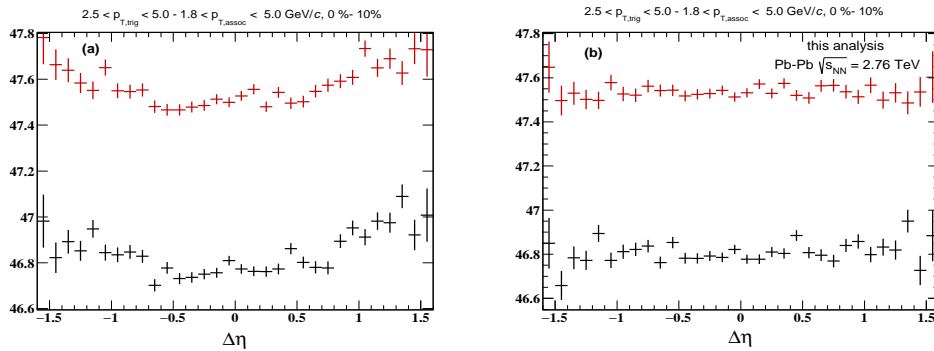


Figure 4.12: (Color online) 1-D  $\Delta\eta$  projections of the correlation function at  $\Delta\phi = \pi \pm 0.25$  (red) and  $\Delta\phi = \pi/2 \pm 0.25$  (black) in different  $p_{T,trig}$ ,  $p_{T,asso}$ , and centrality classes, obtained from data at 2.76 TeV Pb-Pb collisions, (a) before *wing* corrections and (b) after *wing* corrections.

### 4.3.4 Resonance Decays

The contribution from resonance decays also results in a near side peak-like structures in the 2D  $\Delta\eta$ - $\Delta\phi$  correlation function. The yield under the jet peak may be affected from this fake correlations, and should be removed prior to the yield calculation. In this analysis, particle pairs which might have originated from resonance decays are removed by applying cuts on the invariant mass distribution of the pairs.

Assuming pion or proton mass hypothesis for particles in a pair, the invariant mass of each pair is calculated, and removed if it is  $\pm 0.02$  GeV/c around the PDG masses of  $K_s^0$ ,  $\Lambda$  and  $\rho^0$ . However, previous studies have shown that the effect of resonance decays on the jet yield is  $< 2\%$ .

### 4.3.5 Validation of Correction Factors: Monte Carlo Closure Test

To validate the reliability of the weight factors and the correction procedure, same correction exercise is repeated on the reconstructed MC events and compared with the results calculated at the generator level without incorporating any detector effect or reconstruction algorithms. If the correction scheme is appropriate and weight factors are properly extracted, correlation functions derived from the reconstructed MC after corrections, and generated MC should have a perfect agreement. The ratio of two are shown in Fig 4.13(c) is consistent with unity, except at the large  $\Delta\eta$  values where a marginal deviation of 1%-2% is observed.

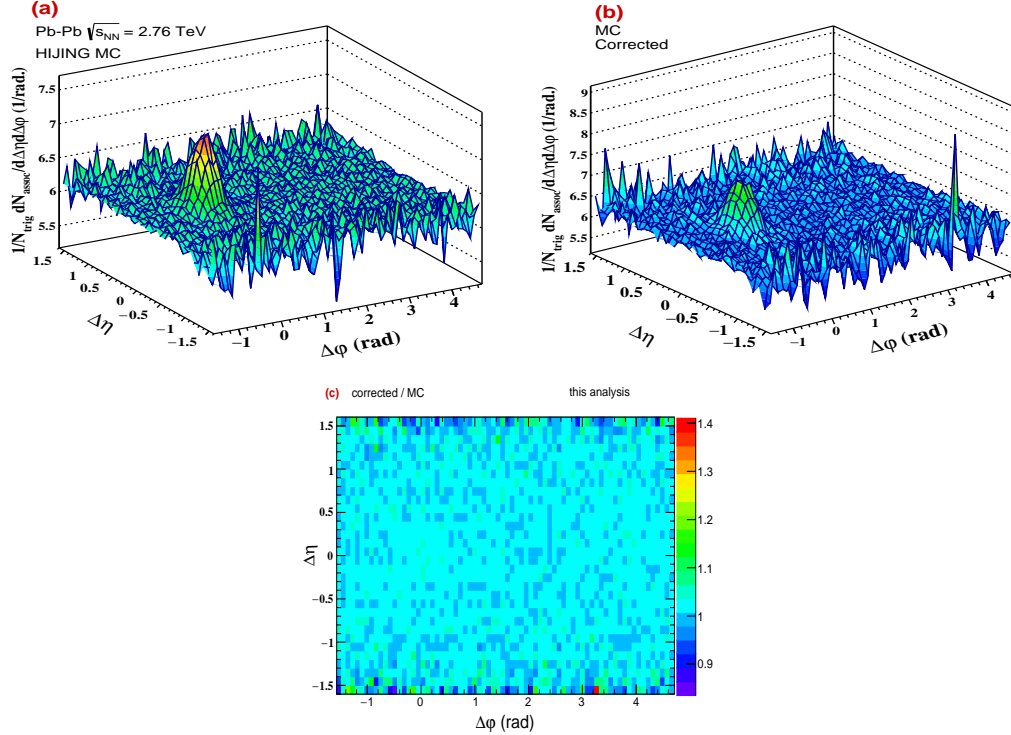


Figure 4.13: (Color online) Steps of closure test: (a) 2-D correlation at generator level, (b) 2-D correlation at reconstruction level but corrected for detector inefficiencies and (c) ratio  $\frac{\text{corrected reconstructed (b)}}{\text{MC generated (a)}}$ . The ratio is found to be at unity except at large  $\Delta\eta$

## 4.4 Yield Extraction

The main focus of this analysis is to extract per-trigger jetlike yield in different intervals of  $p_{T,trig}$ ,  $p_{T,asso}$  and centrality. To quantify the yield under the near side jet peak, contributions from the anisotropic flow modulations need to be subtracted. The zero yield at minimum or ZYAM [8] is a traditional way of background subtraction, developed, and successfully implemented at the RHIC era. However, this method is feasible provided near and away-side peaks are distinguishably separated by a “signal free” zone. At LHC, both near and away side peak shapes are broadened causing an overlap between the two. Consequently, ZYAM estimation is either biased or improper, leading to an erroneous

yield determination.

#### 4.4.1 Flow Subtraction by $\eta$ -gap Method

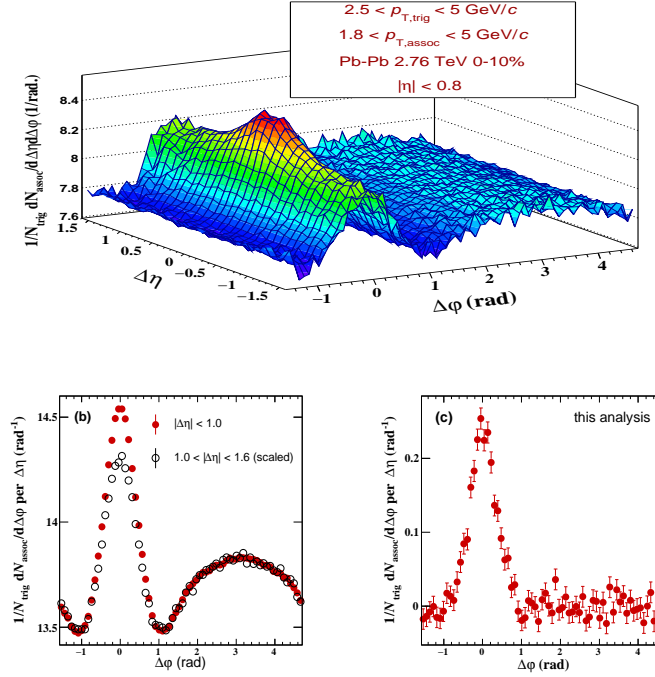


Figure 4.14: (Color online) **a**) 2D  $C(\Delta\eta, \Delta\phi)$  correlation function **b**) projections on  $\Delta\phi$  for  $|\Delta\eta| < 1$  (red) and  $|\Delta\eta| > 1$  (black); **c**) subtracted near side per-trigger-particle jet like yield

Alternatively, flow subtraction is done by the  $\eta$ -gap method, where the yield at long range ( $1 < |\Delta\eta| < 1.6$ ) is subtracted from the short range correlations ( $0 < |\Delta\eta| < 1$ ) as:

$$\frac{d^2 N^{\text{jet}}}{d\Delta\eta d\Delta\phi} = \int_{0 < |\Delta\eta| < 1} \frac{d^2 N^{\text{asso}}}{d\Delta\eta d\Delta\phi} - \int_{1 < |\Delta\eta| < 1.6} \frac{d^2 N^{\text{asso}}}{d\Delta\eta d\Delta\phi} \quad (4.10)$$

This method of flow subtraction however, relies on the assumption that the contributions from the collective flow modulations are independent of  $\Delta\eta$  over the range of measurement, and the near side jet peak is limited to  $|\Delta\eta| < 1$ .

Beside subtracting the collective contributions, this process also removes the pedestal caused by uncorrelated combinatorial background.

The subtraction procedure illustrated in Fig. 4.14, shows a prominent near side jet peak sitting on the so-called “ridge” like structure, extended over large  $\Delta\eta$ . The per-trigger yield of the near side jet peak is determined by subtracting the flow contributions, estimated from the long-range correlations ( $|\Delta\eta| > 1$ ). The results of projections to  $\Delta\phi$  axis in the short-range (red) ( $|\Delta\eta| < 1$ ) and long-range (black) ( $|\Delta\eta| > 1$ ) regions are shown in Fig. 4.14(b). Finally, the per-trigger jet-like yield is calculated from the difference between the two, shown in Fig. 4.14(c).

#### 4.4.2 Extraction of Near Side Jetlike Yield

The near side jetlike yields are calculated from the flow-subtracted  $\Delta\eta, \Delta\phi$  correlation functions projected onto the  $\Delta\phi$  axis. This is done by integrating the correlation function above baseline in the range  $|\Delta\phi| < \pi/2$ . For consistency check, yields are also determined by fitting the one dimensional (1-D)  $\Delta\phi$  projected correlation functions using the following functional forms:

- 1 dimensional  $\Delta\phi$  fitting with two Gaussian functions,

$$\frac{A_1}{\sqrt{2\pi}\sigma_1} e^{(\frac{-\Delta\phi}{2\sigma_1})^2} + \frac{A_2}{\sqrt{2\pi}\sigma_2} e^{(\frac{-\Delta\phi}{2\sigma_2})^2} \quad (4.11)$$

- Generalized Gaussian function

$$A \times \frac{\beta}{2\sigma\Gamma(\frac{1}{\beta})} e^{-|\frac{\Delta\phi}{2\sigma}|^\beta} \quad (4.12)$$

Fig. 4.15 shows a sample 1-D  $\Delta\phi$  correlation function fitted with Eq.4.11 and 4.12. We have observed, that a single Gaussian function could not capture the tail and the peak of the distribution simultaneously. Thus a second Gaussian function was introduced to describe the tail of the correlation function by constraining its standard deviation,  $\sigma$ , to a larger value, i.e,  $\sigma_2 > \sigma_1$ . How-

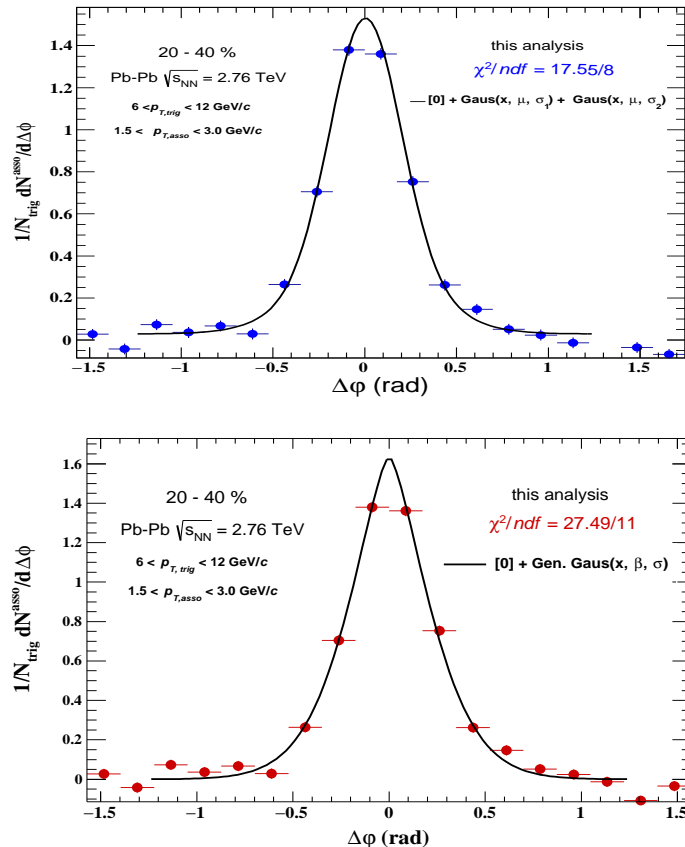


Figure 4.15: (Color online) 1-D  $\Delta\phi$  correlation function fitted with **(top)** double Gaussian and **(bottom)** generalized Gaussian. Respective  $\chi^2/ndf$  values are also mentioned in the figures

ever, un-controlled fitting in some cases resulted in a very high  $\chi^2/ndf$  values. Therefore a generalized Gaussian fit to the correlation function was tried.

In the generalized Gaussian function (Eq. 4.12), the  $\beta$  or the shape parameter is the measure of *peaked-ness* of the distribution function. The physical values of  $\beta$  parameter varies between,  $1 \leq \beta \leq 2$ , corresponds to an exponential and the Gaussian function at  $\beta = 1$  and 2 respectively. While fitting, the lower bound of the  $\beta$  parameter is fixed at unity, as the standard deviation of the distribution ( $\sigma = \frac{\alpha^2 \Gamma(3/\beta)}{\Gamma(1/\beta)}$ ) diverges or becomes undefined for  $\beta < 1$ . The generalized Gaussian fit gives a better description of the correlation function globally, and therefore its parameters are used to quantify the strength of the

correlation function or per-trigger yield of the associated hadrons.

## 4.5 Results

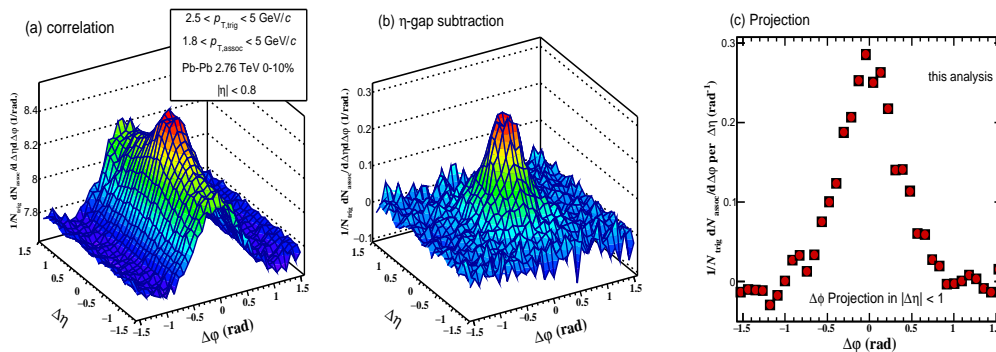


Figure 4.16: (Color online) Two-dimensional (2-D) per-trigger-particle yield of associated charged hadrons are shown as function of  $\Delta\eta$  and  $\Delta\phi$  for  $2.5 < p_{T,trig} < 5$  GeV/c and  $1.8 < p_{T,asso} < 5$  GeV/c, for 0%-10% most central Pb–Pb collisions at 2.76 TeV. **a)** The near-side region is zoomed-in, **b)** after  $\eta$ -gap subtraction, **c)** projection of the same on  $\Delta\phi$  for  $|\Delta\eta| < 1$ .

The 2-D per-trigger-particle distribution of associated charged hadrons is measured as a function of  $\Delta\eta$  and  $\Delta\phi$  in different ranges of  $p_{T,trig}$ ,  $p_{T,asso}$  and centrality classes of Pb–Pb collisions at 2.76 TeV. An example 2-D correlation function in  $\Delta\eta, \Delta\phi$  is shown in Fig. 4.16(a) for trigger particles with  $2.5 < p_{T,trig} < 5.0$  and associated particles with  $1.8 < p_{T,trig} < 5.0$ , in 0%-10% most central collision. The near side region of the correlation function (Fig. 4.16(b)) is zoomed-in for better visualization of the surrounding structures. The main features of correlation structure are a narrow jet fragmentation peak at  $(\Delta\eta, \Delta\phi) \approx (0,0)$  and a flat ridge like structure, symmetrically extended over the large  $|\Delta\eta|$ .

The strong positive correlations at large  $\Delta\eta$  is believed to be a manifestation of an anisotropic modulation in the azimuthal distributions of charged particles with respect to the reaction plane. It is generally perceived, in heavy ion collisions, this anisotropy is driven by the hydrodynamic response to the initial

spatial anisotropy in the overlap region of the collision zone. In non-central events, these correlations are dominated by the second-order component in the Fourier expansion of the  $\Delta\phi$  distribution, familiar as elliptic flow or  $v_2$ .

A similar 2-D correlation plot, shown in Fig. 4.17, shows that the near side ridge structure is drastically reduced when trigger particles are chosen from a higher values of transverse momentum ( $6 < p_{T, trig} < 12$  GeV/c). This observation is consistent with the expectation that the long-range correlations originate from the anisotropic collective emission of the charged particles, dominated by second Fourier coefficient or elliptic flow. Since the elliptic flow values are largely diminished at high  $p_T$  [6], the suppression in the near-side ridge structure is therefore justified.

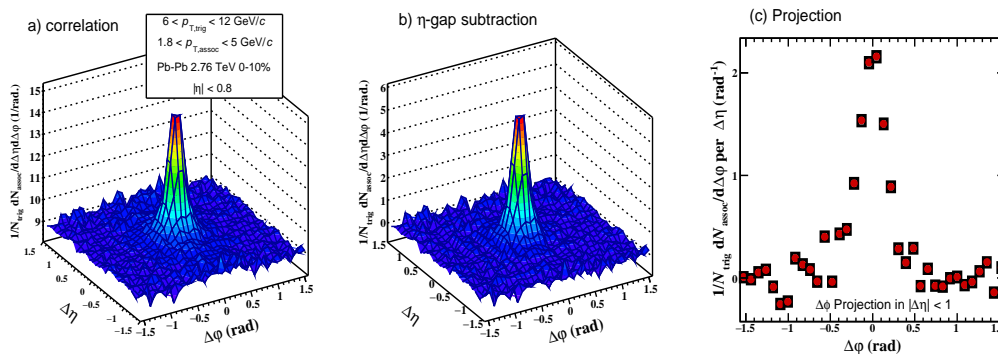


Figure 4.17: (Color online) Two-dimensional (2D) per-trigger-particle yield of associated charged hadrons are shown as function of  $\Delta\eta$  and  $\Delta\phi$  for  $6 < p_{T, trig} < 12$  GeV/c and  $1.8 < p_{T, asso} < 5$  GeV/c, for 0%-10% most central Pb–Pb collisions at 2.76 TeV. **a)** The near-side region is zoomed-in, **b)** after  $\eta$ -gap subtraction, **c)** projection of the same for  $|\Delta\eta| < 1$ .

The flow-subtracted 2-D correlation functions and their projections on the  $\Delta\phi$  axis for  $|\Delta\eta| < 1$  are also shown in the Fig.4.16 and 4.17. On comparing the  $\Delta\phi$  projections between the two, a relative peak shape broadening observed, for intermediate trigger particle momentum, is interpreted as an effect of jet-medium interactions [7].

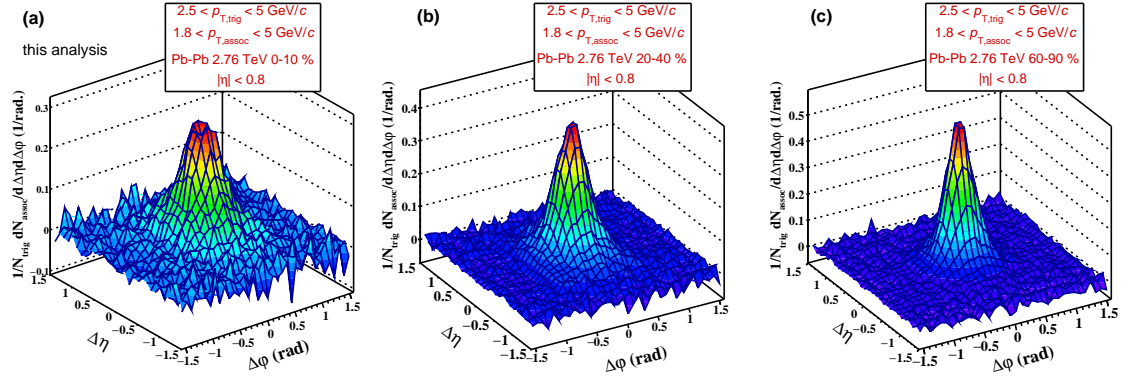


Figure 4.18: (Color online) Two-dimensional (2-D) flow-subtracted per-trigger-particle associated yield of charged hadrons as a function of  $\Delta\eta$  and  $\Delta\phi$  for  $2.5 < p_{T,trig} < 5$  GeV/c and  $1.8 < p_{T,assoc} < 5$  GeV/c, in (a) 0%-10% , (b) 20%-40% and (c) 60%-90% centrality classes of Pb-Pb collisions at 2.76 TeV. Near side zoomed-in for better clarity

To further investigate the effect of jet-medium interplay, centrality evolution of this distributions are compared for intermediate (Fig. 4.18) and high  $p_T$  (Fig. 4.19) trigger particles. A centrality dependent modification in the near side peak shape is evident from the Fig. 4.18, when both trigger and associated particles are from low or intermediate  $p_T$  regions. Whereas, for high- $p_T$  trigger particles (Fig. 4.19) no or negligible peak shape modification is observed, when studied as a function of the collision centrality. These observations are consistent with the expectation, that high- $p_T$  particles, predominantly arising from the surface of the medium (surface bias) immediately fragments in vacuum without any significant interactions with the bulk partonic matter.

#### 4.5.1 $\Delta\phi$ Distributions of Associated Particle Yield

To quantify the features of near side jet peak region, 1-D  $\Delta\phi$  distributions of the correlation functions are calculated by averaging the 2-D flow-subtracted distribution over a limited region of  $\Delta\eta$ .

$$\frac{1}{N_{trig}} \frac{dN^{pair}}{d\Delta\phi} = \frac{1}{\Delta\eta_{max} - \Delta\eta_{min}} \int_{\Delta\eta_{min}}^{\Delta\eta_{max}} \frac{1}{N_{trig}} \frac{d^2 N^{same}}{d\Delta\phi d\Delta\eta} d\Delta\eta \quad (4.13)$$

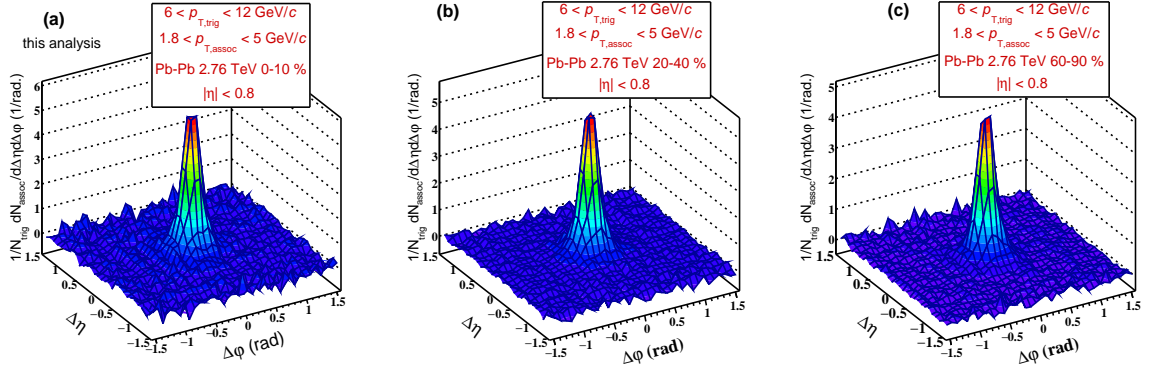


Figure 4.19: (Color online) Two-dimensional (2-D) flow-subtracted per-trigger particle associated yield of charged hadrons as a function of  $\Delta\eta$  and  $\Delta\phi$  for  $6 < p_{T,trig} < 12$  GeV/c and  $1.8 < p_{T,trig} < 5$  GeV/c, in (a) 0%-10% , (b) 20%-40% and (c) 60%-90% centrality classes of Pb-Pb collisions at 2.76 TeV.

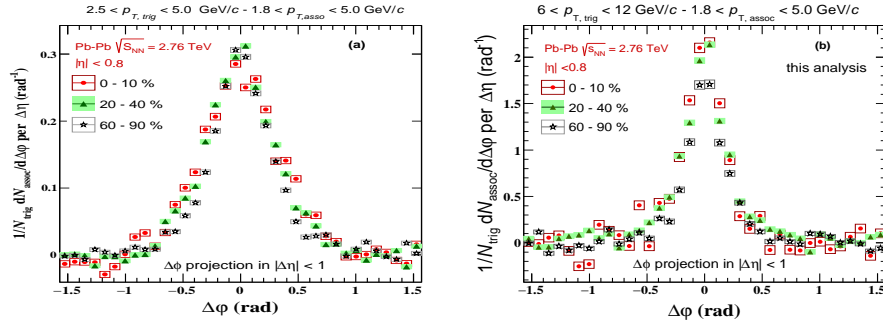


Figure 4.20: (Color online) 1-D  $\Delta\phi$  correlation (a): for  $2.5 < p_{T,trig} < 6$  GeV/c and  $1.8 < p_{T,trig} < 5$  GeV/c, and, (b): for  $6 < p_{T,trig} < 12$  GeV/c and  $1.8 < p_{T,trig} < 5$  GeV/c, in 0%-10%, 20%-40% and 60%-90% centrality classes of Pb-Pb collisions at 2.76 TeV.

The 1-D  $\Delta\phi$  correlation functions extracted by averaging over  $|\Delta\eta| < 1$ , for trigger particle  $p_T$  ranges of  $2.5 < p_{T,trig} < 5.0$  GeV/c and  $6.0 < p_{T,trig} < 12.0$ , and associated particle  $p_T$  range of  $1.8 < p_{T,asso} < 5.0$  GeV/c, in different centrality classes of Pb–Pb collisions at 2.76 TeV are shown in Fig. 4.20. The near side peak at  $\Delta\phi \approx 0$  represents the correlations from jet fragmentation.

A comparison to the peripheral and central collisions for several different  $p_{T,trig}$  and  $p_{T,asso}$  combinations, at same energy, are shown in Fig. 4.21 and Fig. 4.22.

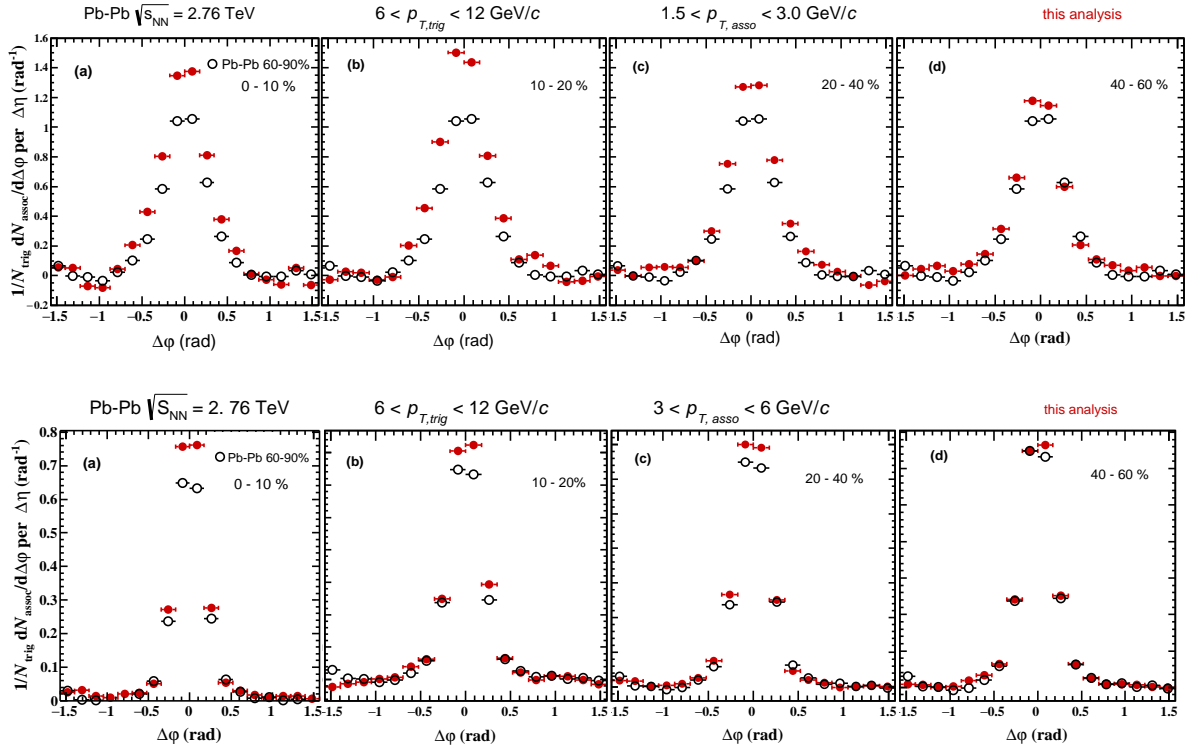


Figure 4.21: (Color online) Per-trigger-particle associated yields of charged hadrons as a function of  $\Delta\phi$  **Top**: for  $6 < p_{T,trig} < 12$  GeV/c and  $1.5 < p_{T,asso} < 3$  GeV/c, and, **Bottom**: for  $6 < p_{T,trig} < 12$  GeV/c and  $3 < p_{T,asso} < 6$  GeV/c are shown for 4 centrality event class of Pb-Pb collisions at 2.76 TeV. For reference, results from most peripheral 60%-90% event classes are superimposed.

In the upper and lower panel of Fig. 4.21, 1-D  $\Delta\phi$  correlation functions in central collisions are compared with 60%-90% most peripheral events for  $6 < p_{T,trig} < 12$  GeV/c and lower values of  $p_{T,asso}$  ( $< 6$  GeV/c). This comparison reveals, though the spread in the  $\Delta\phi$  distributions are visibly similar over all centrality classes, but the magnitude of near side peak is significantly enhanced in central collisions when compared to peripheral ones. However, the magnitude of enhancement is found to depend on the associated particles transverse momentum range. For higher value of  $p_{T,asso}$ , the increase in the amplitude of the near side peak is rather small.

Fig. 4.22 shows the same, but for intermediate  $p_T$  trigger particles, that is,

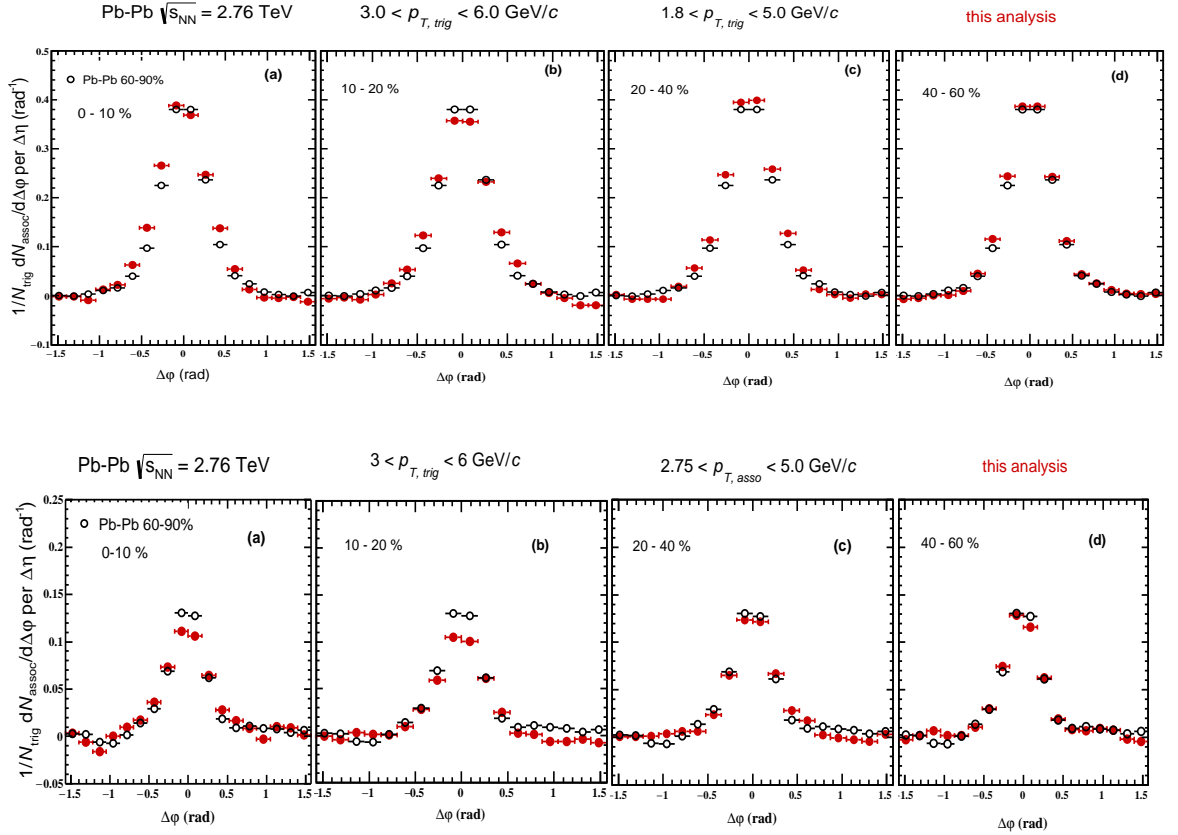


Figure 4.22: (Color online) Per-trigger-particle associated yields of charged hadrons as a function of  $\Delta\phi$  **Top**:for  $3 < p_{T,trig} < 6$  GeV/c and  $1.8 < p_{T,asso} < 5$  GeV/c , and, **Bottom**:for  $3 < p_{T,trig} < 6$  GeV/c and  $2.75 < p_{T,asso} < 5$  GeV/c are shown for 4 centrality event class of Pb-Pb collisions at 2.76 TeV. For reference, results from most peripheral 60%-90% event classes are superimposed.

$3 < p_{T,trig} < 6$  GeV/c. It is interesting to note, that there is almost no change in the near side jet peak amplitude between central and peripheral events over all centrality classes (**Top** panel of Fig 4.22) . The correlation strength is found to be rather diminished in central collisions, compared to peripheral, when the lower bound of  $p_{T,asso}$  is shifted to high  $p_T$  (**Bottom** panel of Fig. 4.22).

This observation seems to suggests, that energy lost by high- $p_T$  partons propagating through the dense QCD matter results in a copious production of low  $p_T$  particles below  $p_T = 2-2.5$  GeV/c.

## 4.5.2 Integrated Associated Yield

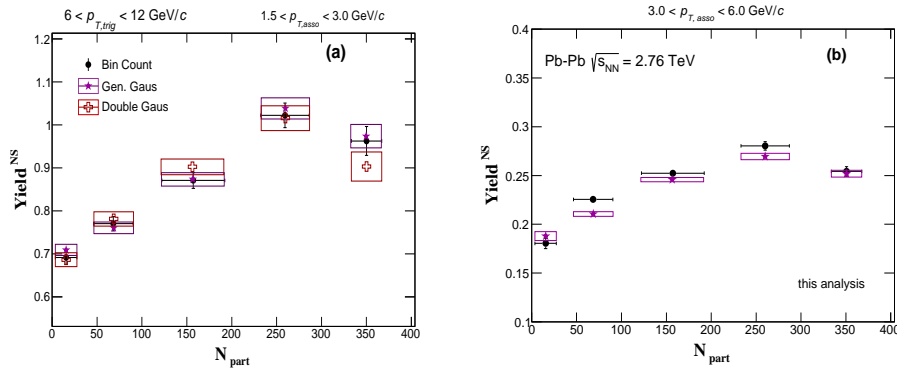


Figure 4.23: (Color online) Integrated per-trigger-particle near side jetlike yield, for  $6 < p_{T,trig} < 12$  GeV/c and  $p_{T,asso}$  intervals of **(a)**  $1.5 < p_{T,asso} < 3.0$  GeV/c and **(b)**  $3.0 < p_{T,asso} < 6.0$  GeV/c are shown as a function of  $N_{part}$  in Pb–Pb collisions at 2.76 TeV. Yield calculated from double Gaussian and generalized Gaussian fit to 1D  $\Delta\phi$  correlation functions are also shown in different markers

In order to extract the yields in near jet peak and compare in different  $p_{T,trig}, p_{T,asso}$  and centrality ranges, 1D correlation function is averaged over over  $-\pi/2 < \Delta\phi < \pi/2$ . Fig. 4.23 shows the integrated yield under the near side jet-peak as a function of number of participating nucleons ( $N_{part}$ ), estimated from the Glauber model fit to the charged particle multiplicity distributions in VZERO detectors.

The yield of the near-side peak, shown in Fig. 4.23, increases while going from the very peripheral 60%–90% to the most central 0%–10% Pb–Pb events, for the  $p_{T,asso}$  interval of 1.5–3.0 GeV/c. This enhancement may be expected based on the principle of energy conservation. The energy lost by high- $p_T$  partons get converted into associated particles, predominantly at low- $p_T$ . This could be a possible indication that the near side partons are also subjected to the medium modification. The enhancement in the near side yield may also be understood from the perspective of the change in the quark to gluon jet ratios in the final state. As gluons are known to couple with the medium strongly, the expected

energy loss for gluon jets are likely to be larger than the quarks. Thus, with the increased fraction of gluon jets at LHC, this enhancement of near side jet yield seems to be consistent. As  $p_{T,asso}$  increases, the centrality dependent increase in the near side yields becomes less prominent. This suggest that the enhancement of the associated yields are limited to low- $p_T$  particles [9]. Yields calculated from the double Gaussian and Generalized Gaussian fit to the 1D  $\Delta\phi$  correlation functions are also superposed in the same plot. The per-trigger jet yield calculated from all three procedures are found to have a reasonable agreement.

Furthermore, for trigger  $p_T$  range of 3-6 GeV/c and associated  $p_T$  interval of 1.8-5.0 GeV/c, the associated particle yield exhibit no significant centrality dependence rather, yields are found to remain constant as a function of  $N_{part}$ , after an initial rise (See Fig. 4.24). Interestingly, for  $p_{T,asso}$  interval of 2.75 to 5.0 GeV/c, correlation strength is found to be suppressed as a function of centrality. This might happen if the majority of the correlated soft particles are below 2 GeV/c. The lack of enhancement in the near side peak yield when triggered by particles at intermediate  $p_T$  may also be attributed to the loss of correlated hadron pairs at small angle because of a phenomena called *trigger dilution* [10], which will be elaborated in the next chapter.

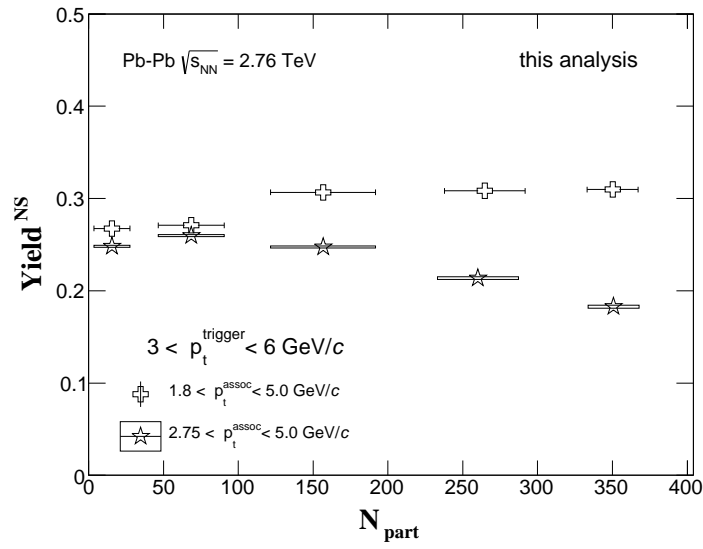


Figure 4.24: (Color online) Integrated per-trigger-particle near side jet-like yield, for  $3 < p_{T,\text{trig}} < 6$  GeV/c and two different intervals of  $p_{T,\text{asso}}$  are shown as a function of  $N_{\text{part}}$  in Pb–Pb collisions at 2.76 TeV. Per-trigger yield for the  $p_{T,\text{asso}}$  interval 2.75–5.0 GeV/c is scaled for better display

# Bibliography

- [1] <https://alimonitor.cern.ch/production/raw.jsp>
- [2] <https://twiki.cern.ch/twiki/bin/view/ALICE/HybridTracks>.
- [3] Lingshan Xu, Chin-Hao Chen, and Fuqiang Wang, Phys. Rev. C 88, 064907 (2013).
- [4] Shantam Ravan, Prabhat Pujahari, Sidharth Prasad, and Claude A. Pruneau, Phys. Rev. C 89, 024906 (2014).
- [5] ANA-56 <https://aliceinfo.cern.ch/Notes/node/33>.
- [6] B. Abelev et. al (ALICE Collaboration), Phys. Lett. B 719, 18 (2013).
- [7] Jan Fiete Grosse-Oetringhaus, for the ALICE collaboration, <https://arxiv.org/abs/1208.1445>.
- [8] J. Adams et al. (STAR Collaboration), Phys. Rev. Lett. 91, 172302 (2003).
- [9] S. Chatrchyan et al. (CMS Collaboration), Eur. Phys. C 72, 10052 (2012).
- [10] L. Adamczyk et al. (STAR Collaboration), Phys. Lett. B 751, 233 (2015).

# Chapter 5

## Dihadron Correlations with Identified Trigger Particles at Intermediate- $p_T$

### 5.1 Introduction

Recently, there is a renewed interest on studies related to intermediate- $p_T$  particle production in heavy ion collisions, using quark coalescence or recombination as a model of hadronization [1]. These studies were largely initiated by two remarkable observations at RHIC, namely, the anomalous baryon enhancement [2] and the constituent quark-number scaling of hadron  $v_2$  [3]. Both phenomena were explicable provided the hadronization of a thermally equilibrated and collectively flowing bulk partonic matter is realized through the mechanism of quark coalescence or recombinations.

At LHC, similar baryon-to-meson enhancement is observed at intermediate ranges of  $p_T$  both in the strange and light flavor sector [4, 5]. However, at LHC, the enhancement in the inclusive baryon-over-meson ratio seems to be an effect of radial flow, that pushes high-mass particles to a relatively higher values of  $p_T$ . Further observations like violation of NCQ-scaling (by an order of 20%) and the equivalence between  $\phi$ -meson and proton  $v_2$  [6], possibly

indicate that the inclusive yields of particles as function of  $p_T$  are determined by their masses rather than the quark numbers [7]. It is also observed that MC event generators, like EPOS [22], that implements hydrodynamics to model the evolution of the bulk partonic matter could reproduce the centrality dependence of  $p/\pi$  enhancement. These observations at LHC were regarded as an evidence to rule out the significance of quark coalescence as a relevant mechanism of particle production at intermediate- $p_T$  [7, 8].

However, in one of the recent publications [9] it was shown, if the phase-space density of constituent quarks is very high, as it is for Pb-Pb collisions at LHC, the NCQ-scaling of  $v_2$  is not a necessary requirement for particle production by quark recombination. Thus, it calls for more differential measurements which could possibly disentangle whether the baryon-meson effect at intermediate- $p_T$  is a natural consequence of radial flow or a manifestation of particle production by quark recombination.

Previous studies on the angular correlation measurements for Au-Au collisions at top-RHIC energy have shown, that intermediate- $p_T$  baryons also exhibit small angle azimuthal correlations- a characteristic feature of jet-like particle production [10, 11, 12, 13]. Moreover, the similar magnitude of baryon and meson triggered correlations with other charged hadrons, except at most central collisions, were indicative of the fact that the baryon excess at the intermediate  $p_T$  region might be associated with the hard scatterings of partons. Since gluons are more likely to fragment into leading baryons [14], a considerable increase in the mid-rapidity gluon density from SPS to RHIC might lead to an enhancement in the baryon production. Additionally, some jet-quenching models predict, that softening of the fragmentation functions due to jet-medium interactions in heavy ion collision might increase the hadrochemical  $p/\pi$  ratio among the sub-leading particles [15, 16]. But such propositions could not be

tested at RHIC because baryon measurements were of limited significance due to small  $p_T$  range and large experimental uncertainties.

The impressive particle identification capability of the ALICE detector has allowed measurements of statistically significant sample of protons upto a momentum of 20 GeV/c over all centrality classes of Pb-Pb collisions at 2.76 TeV and also in the minimum bias pp collisions at the same energy. These measurements have enabled computation of the nuclear modification factor or  $R_{AA}$  of high- $p_T$  protons in different centrality classes of Pb-Pb collisions at 2.76 TeV [7]. Results from these measurements show that at high- $p_T (> 6 \text{ GeV/c})$  the magnitude of suppression is independent of the mass or the constituent quark numbers of the particles. This suggests that jet quenching is not responsible for the modification of the particle species composition at intermediate- $p_T$ . The direct measurements of the Fragmentation Functions (FFs) for these quenched jets have also revealed that for charged tracks with  $p_T > 4 \text{ GeV/c}$ , FFs are similar to those measured in pp collisions for sub-leading jets with  $p_{T,jet} > 50 \text{ GeV/c}$  [17]. This rules out the scope of explaining the intermediate- $p_T$  baryon enhancement as a consequence of biases in the fragmentation of the quenched jets that results in the emission of more intermediate or high- $p_T$  baryons compared to mesons.

From these results it may be inferred that baryon excess at intermediate- $p_T$  is of soft origin and not due to the modification of the jet-fragmentation. The soft processes could be either radial flow or the hadron production via recombination. However, the jet-like correlation of baryons at the intermediate- $p_T$  range, a typical of hard processes, seems to be incompatible with hydrodynamical models. On the other hand, jet-like correlations could be preserved within the recombination approach if hadronization occurs via recombination between jet fragments and quarks from the thermalized medium.

There are two classes of models where attempt is being made to address the origin of jet-like peak in the baryon-triggered correlation within the framework of the recombination model. The model of Hwa and Yang [18] considers recombination between shower partons from the hard scattering process and the thermal quarks from the medium in the immediate vicinity of the jet fragments. The model of Fries et al., [19] in contrary, allows high- $p_T$  partons to fragment independently into hadrons. But, the fast moving partons while propagating through the medium lose energy, creating a region around its trajectory with a slightly increased temperature and with additional momentum boost along its direction. Partons from this region are then recombined into hadrons. The kinematic focussing of the recombining partons along the jet-direction endow the detected hadrons at this  $p_T$ -range with a jet-like correlation.

To further explore the jet-like structure in region of baryon excess, triggered two particle correlations measurements are performed where the trigger particle is identified as a meson ( $\pi$ ) or baryon ( $p/\bar{p}$ ) at intermediate- $p_T$  ( $2.5 < p_{T, trig} < 5.0$  GeV/c). Associated particles are lower  $p_T$  charged hadrons in the momentum range of 1.8-5.0 GeV/c. This study is performed on the data taken by the ALICE experiment at CERN for Pb-Pb collisions at  $\sqrt{s_{NN}} = 2.76$  TeV. In the trigger  $p_T$  range, track-by-track particle identification is done, based on the combined TPC and TOF responses.

Details of particle identification scheme, construction and correction of the 2-D ( $\Delta\eta, \Delta\phi$ ) correlation function with identified trigger particles, yield extraction and, finally the results are discussed and compared with the MC event generators in the subsequent sections of this chapter, respectively.

## 5.2 Particle Identification in ALICE

The ALICE experiment at CERN is equipped with a variety of detectors which complement each other in their ability to identify particles in different intervals of transverse momentum. The particle identification (PID) in ALICE is performed, based on the PID information available from the detectors like: ITS, TPC, TOF, TRD and HMPID. Each of these detectors generates a certain raw signal which may be used independently or conjointly when performing the particle identification. Combining the PID information from these detectors, a track-by-track identification of particle is made possible at low and intermediate  $p_T$  range ( $< 4\text{-}5$  GeV/c). In this analysis, PID information from TPC and TOF is used to perform particle identification over the momentum range of 2.5-5.0 GeV/c on a track-by-track basis.

The TPC is the main central barrel detector of ALICE, where particle identification is done by measuring the fractional energy loss  $\frac{dE}{dx}$  in the detector gas volume. The  $\frac{dE}{dx}$  is calculated in a truncated mean approach by averaging over the energy deposited by a track in each of the ionisation clusters. In the ALICE TPC, the number of clusters may go upto 159 which correspond to the number of pad rows on the readout plane. So, the per-unit length energy loss of the whole track is:

$$\frac{dE}{dx} = \frac{1}{m} \sum_{i=1}^m \left( \frac{\Delta E}{\Delta x} \right)_i \quad (5.1)$$

where  $\left( \frac{\Delta E}{\Delta x} \right)_i$  is the per unit length energy loss recorded in cluster  $i$  and,  $m$  is an integer that runs over the first 60% lowest cluster energy values. This is done to remove the large Landau-tail contributions from the underlying cluster charge distribution which otherwise leads to large track-to-track fluctuation in the average  $\frac{dE}{dx}$  values. The per-track  $\frac{dE}{dx}$  values determined from the truncated mean method results in a Gaussian distribution when measured in slices of

momentum. The  $\frac{dE}{dx}$  resolution was found to vary between 5-8%, depending on the number of associated clusters per-track, track inclination angle, drift distance, energy loss itself, and the detector occupancy.

The TOF detector measures the flight times of particles with a resolution of  $\sim 80$ -85 ps, allowing particle identification at higher values of transverse momentum. The overall time resolution depends on the intrinsic resolution of the detector along with its associated electronics, tracking, and the resolution of the collision time measurement.

### 5.2.1 Particle Identification using TPC-TOF

The detector responses are represented in terms of raw signal,  $\chi$ , which may include time-of-flight information from the TOF,  $t_{TOF}$  or the specific energy loss,  $\frac{dE}{dx}$  measured by the TPC. The particle identification is generally done by formulating a PID discriminating variable, that makes use of these detector response(s). The preferred discriminating variable for PID is the so-called  $n\sigma$ , defined as the deviation of the measured signal from that of the expected signal for a species  $i$  ( $\pi, k, p$ ), in terms of the detector resolution ( $\sigma$ ):

$$n\sigma^i = \frac{\chi_{measured}^i - \chi_{expected}^i}{\sigma^i} \quad (5.2)$$

Where the resolution parameter,  $\sigma$  depend on the track properties like: track-length, momentum, and other parameters used in the reconstruction algorithm.

The PID discriminating variable in TPC is defined as:

$$n\sigma_{TPC}^i = \frac{\frac{dE}{dx}_{measured}^i - \frac{dE}{dx}_{expected}^i}{\sigma_{\frac{dE}{dx}}^i} \quad (5.3)$$

Whereas, the same quantity for the TOF is defined as:

$$n\sigma_{TOF}^i = \frac{t_{measured}^i - t_{expected}^i}{\sigma_{TOF}^i} \quad (5.4)$$

Based on the combined TPC-TOF response, a track-by-track particle identification is performed by calculating  $n\sigma_{PID}^2 = n\sigma_{TPC}^2 + n\sigma_{TOF}^2$ . For a given species, tracks within the  $3\sigma$  circular cut in the 2-D  $n\sigma_{TPC}$ - $n\sigma_{TOF}$  plane are assigned with an identity of that particular species. An example of this is illustrated in Fig. 5.1, which shows the combined PID signals of pions, kaons and protons in a 2-D plot in different intervals of  $p_T$ . Clearly, the separation is seen to decrease with the increase in  $p_T$  range. To minimise the contamination due to mis-identification, strict cuts are imposed at higher values of  $p_T$ , where two species have overlapping areas.

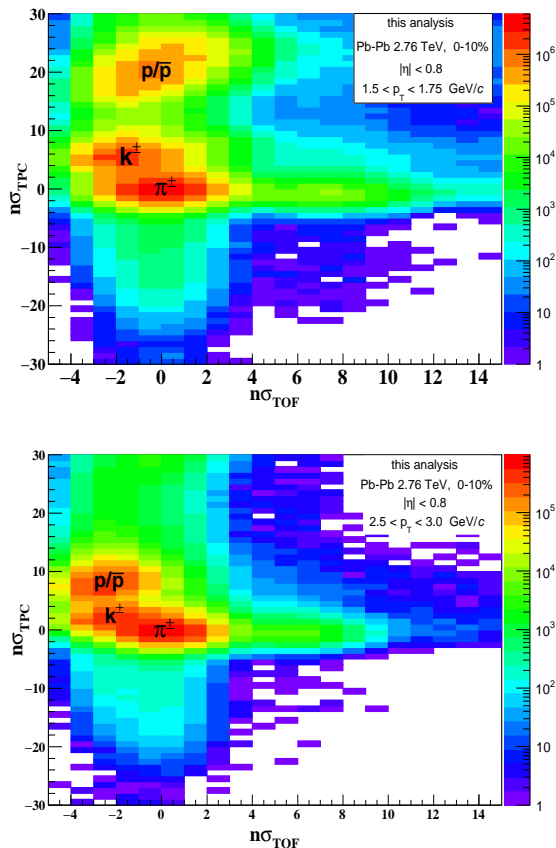


Figure 5.1: (Color online) The combined PID signal of TPC-TOF is shown in 2-D plots for the  $p_T$  range of **(top)**  $1.5 < p_T < 1.75$  GeV/c and **(bottom)**  $2.5 < p_T < 3.0$  GeV/c. The PID signals are expressed in terms of the number-of-standard deviation ( $n\sigma$ ) from the expected response for pions in each detector

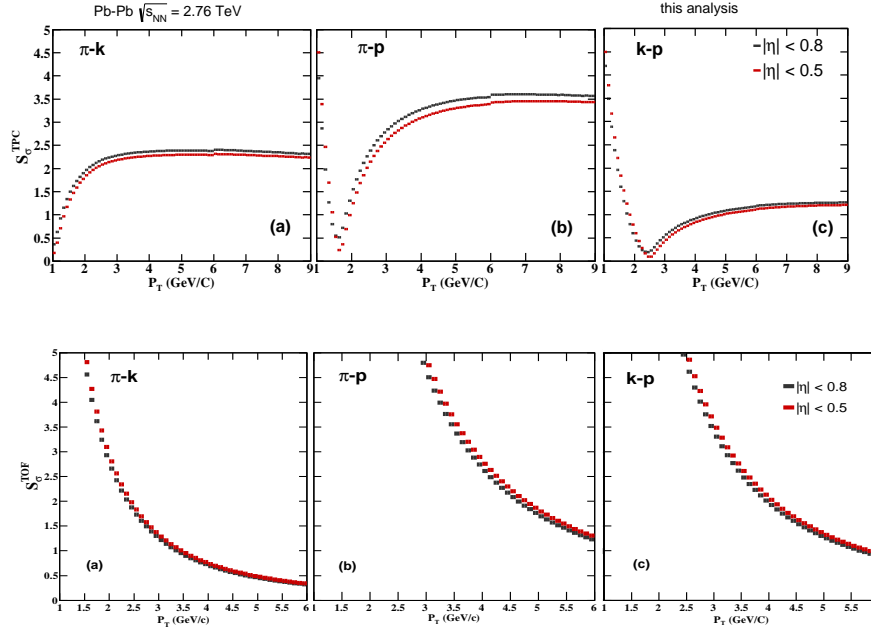


Figure 5.2: (Color online) The separation power  $S_\sigma$  as a function of  $p_T$  : (**top panels**) for TPC and (**bottom panels**) for TOF. Results are shown for Pb-Pb collisions, averaging over all centrality classes between 0%-90%. Since the detector responses could be track-length dependent, separation power is also calculated in a small  $\eta$ -interval. The red and black lines represent separation power in  $|\eta| < 0.5$  and  $0.8$ , respectively

An initial guess on the cut values can be made by computing separation power a detector between two particle species. For example, separation between pions and kaons in terms of number of standard deviation ( $S_\sigma$ ) in TPC is calculated as follows:

$$S_\sigma^{TPC} = \frac{\langle \frac{dE}{dx} \pi^\pm \rangle - \langle \frac{dE}{dx} k^\pm \rangle}{0.5(\sigma_{\pi^\pm} + \sigma_{k^\pm})} \quad (5.5)$$

The  $S_\sigma^{TOF}$  can also be calculated following the similar approach. Fig. 5.2 shows the separation power between particle species in TPC (**top panel**) and TOF (**bottom panel**). The separation power in TPC falls off sharply below 2 GeV/c, followed by a rise and finally stabilizes beyond 4-5 GeV/c. The increase in separation power between 2-4 GeV/c is because of the relativistic rise of the  $\frac{dE}{dx}$  response. However, for  $p_T > \sim 5$  GeV/c, the energy loss approaches a constant value known as the Fermi plateau. This is reflected by the flattening of the

separation power at very high- $p_T$ . Because the TPC response is sensitive to the track-length, the separation power of tracks at mid pseudorapidities (red lines) are slightly reduced. The separation power is also calculated for the TOF detector, which exhibit sharp and monotonic decrease with  $p_T$ .

In the TPC-TOF analysis, the cut values are optimised to ensure selection of highly pure but statistically significant sample. However, depending on the separation power ( $S_{\sigma}^{TPC/TOF}$ ) of a detector, a track may be assigned to more than one species and therefore counted doubly. In this analysis, an exclusive identification scheme is adopted, where tracks with multiple identities are rejected straightaway. The cut values are also tightened at high- $p_T$ , so that the purity of the sample is not compromised. Cuts on the  $n\sigma_{PID}$  are tabulated in Table. 5.1. These cut values are varied to study PID related systematic uncertainty.

$p_T$ interval in GeV/c	$n\sigma_{PID}$
$2 \leq p_T \leq 3.5$	$\leq 3$
$3.5 < p_T \leq 4.5$	$\leq 2$
$4.5 < p_T \leq 6.0$	$\leq 2$

Table 5.1: Summary of cut values

Fig.5.3 and 5.4 show the  $n\sigma_{PID}$  distributions for pions as a function of  $p_T$  and its projection in different  $p_T$  intervals before and after the PID-cut. It is evident from the projection plots in the Fig. 5.4 that Gaussian peaks centered at higher values of  $n\sigma$ , as observed in Fig.5.3, representing the contributions from the other particle species, are removed when the selection cuts are applied. Thus, pure samples of pions are obtained once this selection cuts are applied but its exact purity can not be quantified unless the sources of contaminations are identified and their contributions are accurately estimated. This is discussed in the next section.

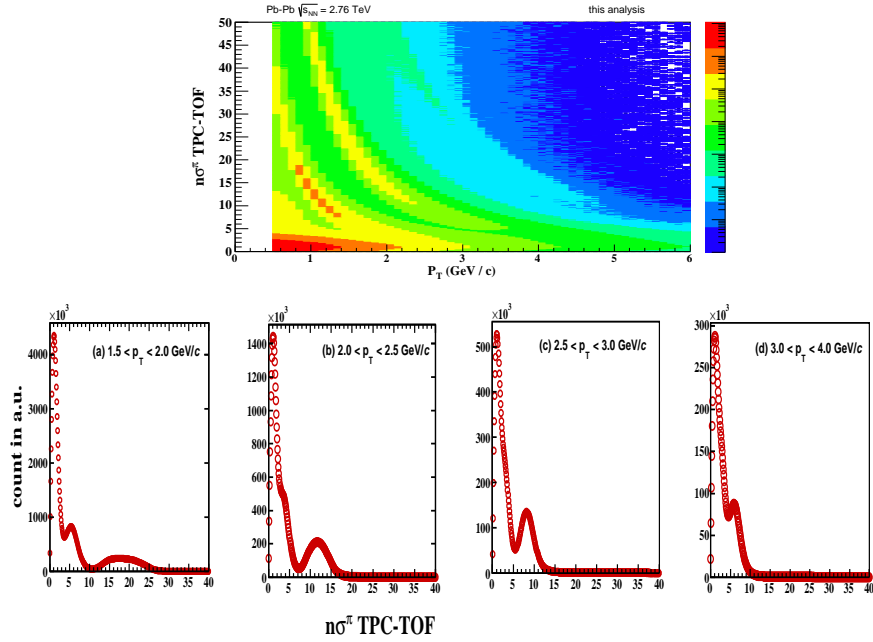


Figure 5.3: (Color online) The  $n\sigma_{PID}$  distributions for pions as function of  $p_T$  (top panel) and its projections in different  $p_T$  bins (bottom panel), before PID cuts.

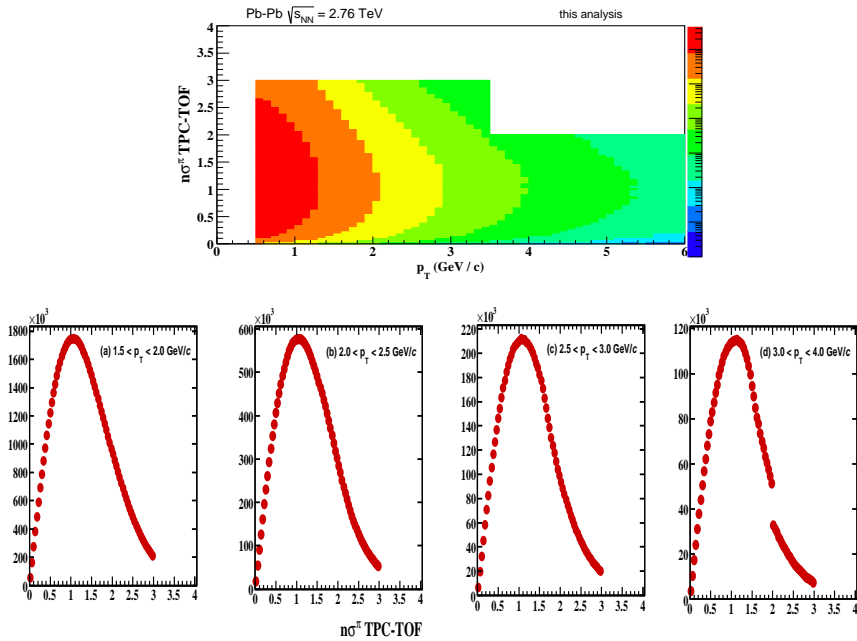


Figure 5.4: (Color online) The  $n\sigma_{PID}$  distributions for pions as function of  $p_T$  (top panel) and its projections in different  $p_T$  bins (bottom panel), after PID cuts.

## 5.2.2 Evaluation of PID efficiency and Misidentification Fractions

In order to obtain quantities of physical interest, signals extracted immediately after the selection cuts are corrected for the relevant inefficiencies due to the selection criteria applied to retrieve proper PID information and the PID strategy itself. Both quantities are estimated from Monte Carlo (MC) simulations, customized to reproduce accurate description of the signals present in the data. Since some features of real data are absent in MC simulations, data-driven parameterisations (*PID Response Tuned-on-data*) are used to minimize the discrepancies of detector responses between the two.

Considering only pions, kaons, and protons, a  $3 \times 3$  PID matrix is defined, each element of this matrix represents the probability of identifying a species  $i$  as a species  $j$ , that is:

$$\begin{pmatrix} \varepsilon_{\pi\pi} & \varepsilon_{\pi k} & \varepsilon_{\pi p} \\ \varepsilon_{k\pi} & \varepsilon_{kk} & \varepsilon_{kp} \\ \varepsilon_{p\pi} & \varepsilon_{pk} & \varepsilon_{pp} \end{pmatrix}$$

The diagonal elements,  $\varepsilon_{ii}$  of the PID matrix represent the detection efficiency of a species  $i$  which is defined as the ratio of correctly identified particles belonging to species  $i$  over the total number of particles of type  $i$ :

$$\varepsilon_{ii} = \frac{N_{i \text{ identified } i}}{N_{i \text{ all}}} \quad (5.6)$$

Whereas, the off-diagonal elements,  $\varepsilon_{ij}$  represent the misidentification probability of a species  $i$  as a different species  $j$ :

$$\varepsilon_{ij} = \frac{N_{i \text{ misidentified } j}}{N_{j \text{ all}}} \quad (5.7)$$

The misidentification probabilities are different from contamination factors, where former is independent of relative abundances of particles in data and MC, but the later strongly depends on the particle ratios in data. Since the estimation of the contamination factors are sensitive to the relative abundances of the particles in data, it is determined with a data-driven method using the following relation:

$$C_{ij} = \varepsilon_{ji} \times \left(\frac{Y_j}{Y_i}\right)_{data} \quad (5.8)$$

where  $C_{ij}$  is the contamination of the species  $i$  due to a different species  $j$ .

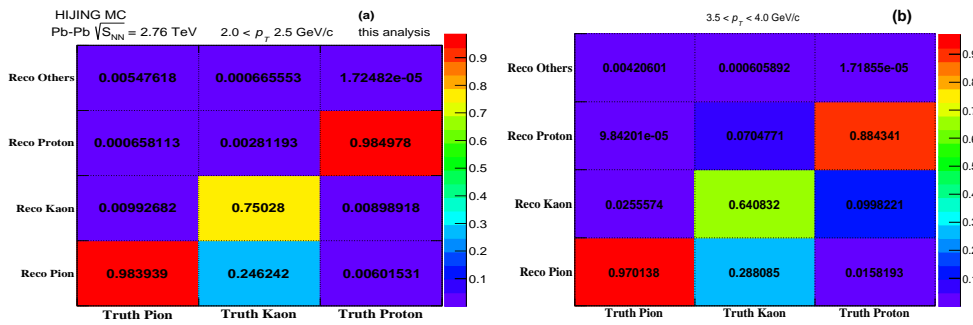


Figure 5.5: (Color online) The PID efficiency matrix for (a)  $2.0 < p_T < 2.5$  GeV/c and (b)  $3.5 < p_T < 4.0$  GeV/c

The PID efficiency matrices for the  $p_T$ -interval of 2.0-2.5 GeV/c and 3.5-4 GeV/c are reported in Fig 5.5. The values on diagonal element of matrices are the PID efficiencies, that represent the correctly identified fraction of particles of a particular species. Whereas the fraction of wrongly identified particles or the misidentification fraction (say pions reconstructed as kaons) are represented by the off-diagonal terms.

All these values are obtained from the MC HIJING simulations, once the detector responses in MC productions are tuned in accordance with the real-data. The reconstructed MC sample do not reproduce all features of the true detector response because of the fluctuations and stochastic changes of the gas gain,

abrupt variations in the detector occupancies, sudden noises in the front-end electronics and other uncontrollable and unprecedented random effects which could not be manipulated at the simulation level. This discrepancy between data and MC productions could be reduced by using the *Tune-On-Data* option in the PIDResponse task-an official framework for PID-based analysis in ALICE, where the expected detector responses are derived from the data itself instead of using MC signal. Additional corrections are also implemented that take care-off the acceptance and multiplicity dependence of the detector response. Like, for a better TPC PID, it is highly recommended to use  $\eta$  and multiplicity corrections of the TPC signals.

### 5.3 Analysis and Correction Procedure

The two-particle correlations in  $\Delta\eta$  and  $\Delta\phi$ , with identified trigger particles at intermediate  $p_T$  ( $2.5 < p_{T,trig} < 5.0$ ), are studied as a function of collision centrality for Pb–Pb collisions at 2.76 TeV. Apart from the particle identification, the analysis technique and the correction procedures are exactly similar to one described in previous chapter. Recalling, that each pair of trigger and associated particle is weighted by a correction factor that accounts for detector acceptance, reconstruction efficiency and contamination due to secondary particles; for the identified trigger particle correlations, these correction factors also include, the TOF matching efficiency and the efficiencies related to the particle identification. The correction factors, defined as the ratio of number of reconstructed MC tracks of a particular species ( $\pi, K, p$ ) to the total number of generated primary particles of the same species, are extracted from the MC simulations using the following the relation:

$$\omega = \frac{N^{i=\pi,K,p} \text{ reconstructed and matched with MC PID}}{N^{i=\pi,K,p} \text{ generated}} \quad (5.9)$$

Additionally, a matching is required between the reconstructed identity and the PDG values (e.g. pion=211) of the tracks at generator level and, wrongly identified tracks (pions reconstructed as kaons) are discarded when calculating the weight factor in Eq. 5.9.

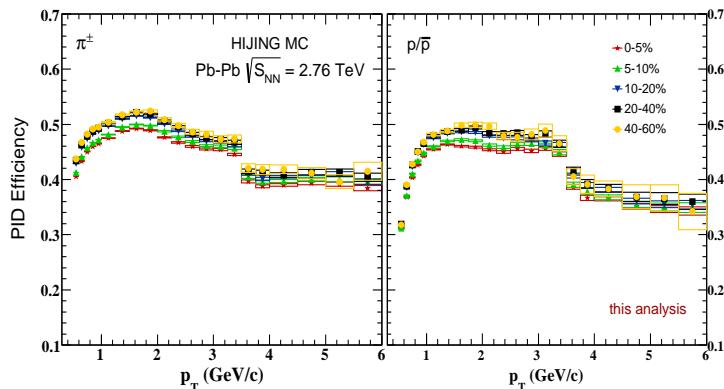


Figure 5.6: (Color online) Identification efficiency or the weight factor obtained from Eq. 5.9 as a function of  $p_T$  for **(Left)**  $\pi$  and **(Right)**  $p/\bar{p}$  in different intervals of centrality.

In Fig.5.6, the particle identification efficiency or the weight factor defined in Eqn. 5.9 is reported as a function of  $p_T$  for  $\pi$  and  $p/\bar{p}$  in different centrality classes of Pb–Pb collisions at 2.76 TeV. This figure suggests that the weight factors have negligible multiplicity dependence. The same weight factor, calculated in different pseudorapidity intervals of 0%-10% most central collision is reported in Fig. 5.7 for hadrons, pions and protons. Also shown, their respective ratios between the central and peripheral collisions (60%-90%) in the bottom panel of the same plot. The large difference between the hadrons and the identified particle weight factors are attributed to the efficiency losses due to the TOF matching and the particle identification scheme.

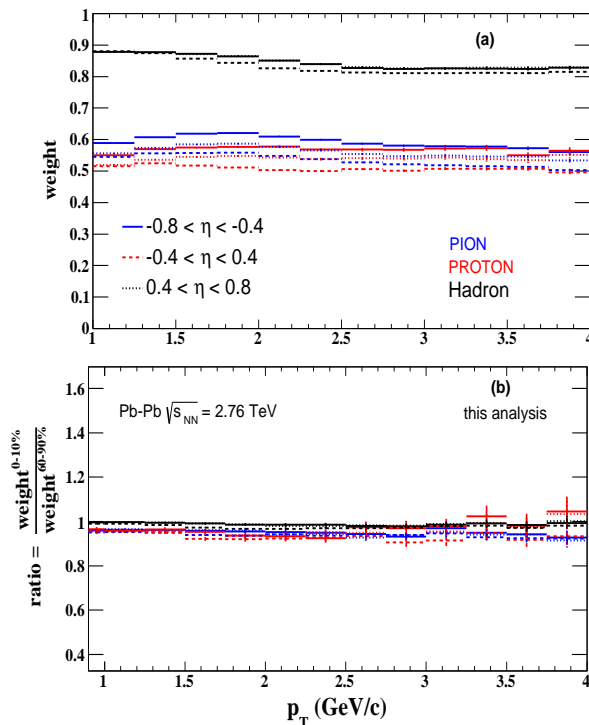


Figure 5.7: (Color online) Weight factors in Eq. 5.9 for different particle species in different intervals of  $\eta$  are presented as a function of  $p_T$  (a). The ratio of the weight factors between central (0%-10%) and peripheral (60%-90%) are shown in (b).

## 5.4 Yield Extraction, Results and Discussions

The efficiency corrected ( $\Delta\eta, \Delta\phi$ ) distributions of pion-charged hadron and proton-charged hadron two particle correlations are presented in Fig. 5.8 and Fig. 5.9, for five centrality classes of Pb–Pb collisions at 2.76 TeV, respectively. The correlation functions are constructed by pairing identified trigger particles (protons/ pions) at intermediate  $p_T$  ( $2.5 < p_{T, trig} < 5$ ) with unidentified charged hadrons in the transverse momentum range of 1.8-5.0 GeV/c.

The resulting correlation functions, shown in Fig. 5.8 and 5.9, exhibit a prominent trigger species dependence both in the jet and the ridge region. While the ridge amplitude is significantly enhanced for the proton triggered correla-

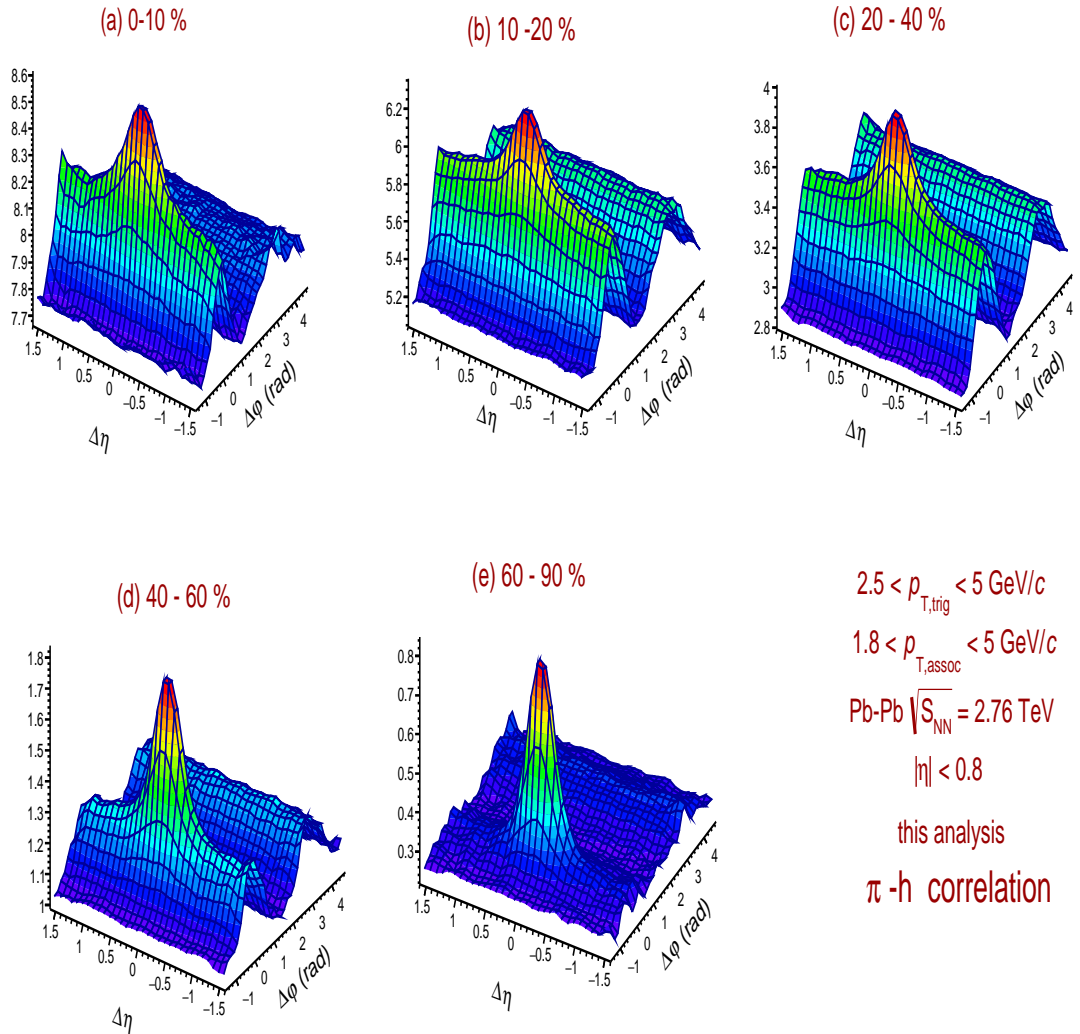


Figure 5.8: (Color online) Two-dimensional  $\Delta\eta$ ,  $\Delta\phi$  correlation functions for pion triggers for different centrality classes of Pb-Pb at 200 GeV. All trigger and associated charged hadrons are selected in the respective  $p_T$  ranges  $2.5 < p_{T,trig} < 5 \text{ GeV}/c$  and  $1.8 < p_{T,asso} < 5 \text{ GeV}/c$ . The z-axis for all plots in this figure represent associated per-trigger yield expressed by  $\frac{1}{N_{trig}} \frac{d^2 N_{asso}}{d\Delta\eta d\Delta\phi} (rad^{-1})$ .

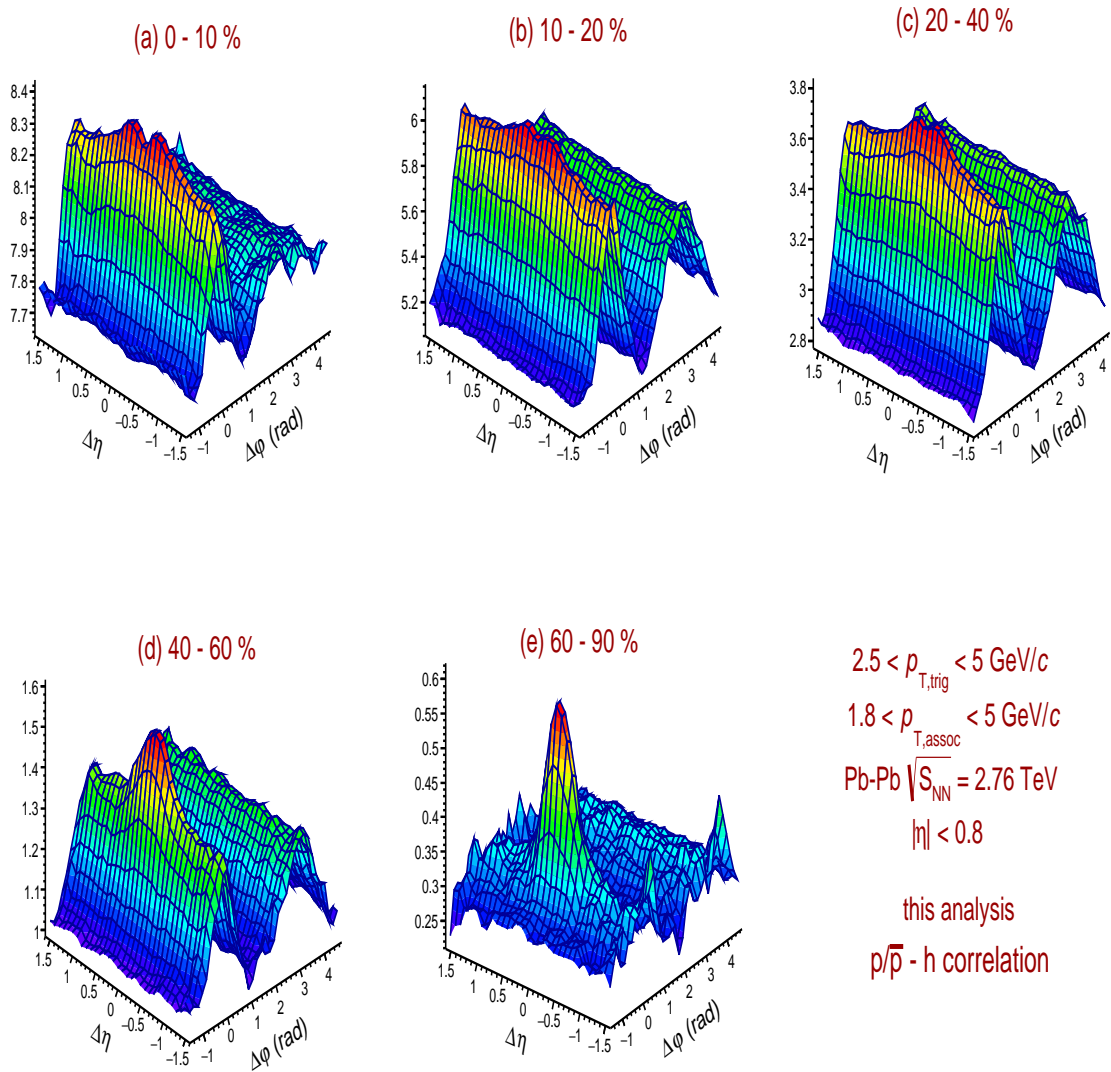


Figure 5.9: (Color online) Two-dimensional  $\Delta\eta, \Delta\phi$  correlation functions for proton triggers for different centrality classes of Pb-Pb at 200 GeV. All trigger and associated charged hadrons are selected in the respective  $p_T$  ranges  $2.5 < p_{T, \text{trig}} < 5 \text{ GeV}/c$  and  $1.8 < p_{T, \text{asso}} < 5 \text{ GeV}/c$ . The z-axis for all plots in this figure represent associated per-trigger yield expressed by  $\frac{1}{N_{\text{trig}}} \frac{d^2 N_{\text{asso}}}{d\Delta\eta d\Delta\phi} (\text{rad}^{-1})$ .

tions, the pion triggered correlations, on the other hand, feature a pronounced near side jet peak over the so-called ridge structure extended to large  $\Delta\eta$ . However, the proton triggered correlations exhibits a striking difference, showing a depletion in the associated charged particle distributions around  $(\Delta\eta, \Delta\phi) = (0,0)$ . This depletion shows a significant centrality dependence, and the peak shape is gradually recovered when moving from central to peripheral collisions.

It is known by now, that the artificial depletion in the correlation structures are the consequences of track reconstruction effects, particularly known as track splitting and track merging. These effects, reduce the number of same event pairs formed out of the tracks with similar momentum and small angular separations. On the other hand, background constructed by pairing tracks from different events (mixed event pairs) are not affected by such reconstruction inefficiencies. As a result, when same event distributions are divided by the mixed event background (without two-track cut), a narrow hole of severely depleted yield is punched through the correlation function, centered at  $(\Delta\eta, \Delta\phi) = (0,0)$ . A detailed investigation on the the origin of the dip structure is performed by varying the criteria of rejecting the track-pairs, potentially affected by the two-track resolution effect.

### 5.4.1 Track Splitting and Merging effects

The track splitting and track merging causes an artificial depletion in the correlation structure around  $(\Delta\eta, \Delta\phi) = (0,0)$ , but, the location of the dip in  $\Delta\phi$  depend on the relative bending of the trigger and associated tracks. This can be studied by repeating the entire analysis in a charge separated mode, where the correlation functions are constructed for different charge combinations of trigger and associated particles, that is,  $++,+,-,-+$  and  $--$ .

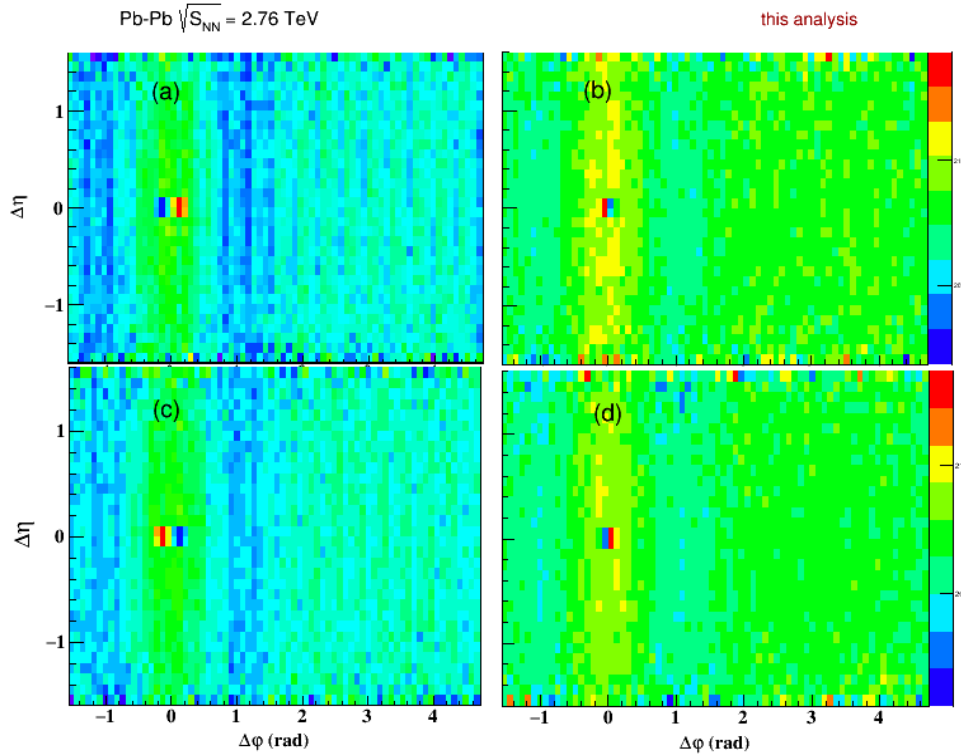


Figure 5.10: (Color online) The dip region in  $(\Delta\eta, \Delta\phi)$  for proton-hadron correlations in 10-20% central Pb-Pb collisions at 2.76 TeV for four charge combinations of trigger and associated particles : **(a)** (trig , assoc ) = (+, -), **(b)** (trig , assoc ) = (+, +), **(c)** (trig , assoc ) = (-, +), and **(d)** (trig , assoc ) = (-, -).

Fig. 5.10 displays the 2-D correlation functions in  $\Delta\eta$  and  $\Delta\phi$  for four different charge combinations of trigger and associated particles, showing a fine dip on the near side peak region of the correlation structure. The dip for like sign combinations of trigger and associated particles are dominantly due to track merging effect, whereas for the unlike pairs the dip originates from the track splitting. It may be noted that dip for the like-sign pairs are exactly located at  $(\Delta\eta, \Delta\phi) = (0, 0)$ , but for unlike pairs, it is slightly displaced on either side  $\Delta\phi$ .

As the track merging and track splitting causes the loss of track pairs from both signal and the combinatorial background, the magnitude of the dip would be more pronounced in central collisions where the background contributions

are really high. This is indeed observed in the Fig. 5.9, where the dip magnitude progressively increases from peripheral to central collisions.

In principle, the track merging and track splitting effects are taken care by two-track resolution cut that removes track pairs with angular separation in  $\Delta\eta$  and  $\Delta\phi_{min}^*$  less than 0.02 from both real and mixed events. The angular separation  $\Delta\phi_{min}^*$  of a track pair is calculated at a radius, where the inter-track separation in  $\phi$  is minimum. For TPC-only tracks,  $\Delta\phi_{min}^*$  is calculated within the TPC radii, i.e,  $80 \text{ cm} < R < 250 \text{ cm}$ . However, for global tracks, to avoid track merging or track splitting in the ITS,  $\Delta\phi_{min}^*$  is calculated within the radial stretch of ITS + TPC, i.e,  $20 \text{ cm} < R < 250 \text{ cm}$ .

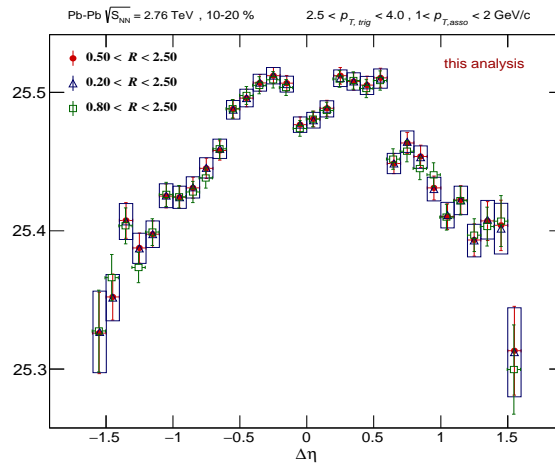


Figure 5.11: (Color online) The  $\Delta\eta$  projection of unsubtracted 2-D correlation function, showing comparison of dip structure on the near side peak region after correcting for the two-track resolution effects in three different ranges of radial distances

Fig. 5.11 shows the  $\Delta\eta$  projection of proton triggered correlation (without background subtraction) in the  $\Delta\phi$  interval of  $\pm\pi/2$  for 10-20% most central collisions, after correcting for the two-track resolution effects in three different ranges of radial distances. Also, the criterion for rejecting the track pairs with minimum angular separation in  $\Delta\phi$ , i.e ,  $\Delta\phi_{min}^*$ , is varied from the default value of 0.02 to 0.05 and 0.1, which are shown in Fig.5.12. These variations, though

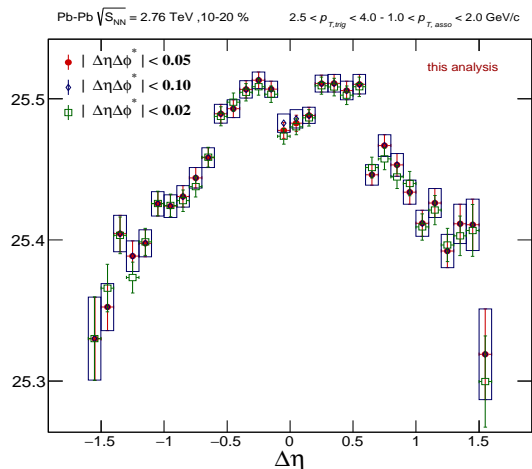


Figure 5.12: (Color online) The  $\Delta\eta$  projection of unsubtracted 2-D correlation function, showing comparison of dip structure on the near side peak region for different magnitudes of two-track resolution cuts

reduce contributions from track merging or splitting, but no significant change in the dip structure is observed.

Similar depletion in the correlation structure was also reported in the balance function analysis [20], where it was argued to be an effect of charge dependent short range correlations and, not an effect of detector in-efficiency. However, unlike balance function distributions, where the depletion is seen to be more pronounced in peripheral collisions, proton triggered correlations, in contrary, exhibit stronger depletion in the central events.

## 5.4.2 Near Side Depletion in MC models

To examine further, whether the origin of the dip is limited to trivial effects of detector inefficiency, correlation functions triggered by identified particles are calculated from the MC event generators without implementing any detector effect. Interestingly, in some of the event generators (see Fig. 5.13), identical dip in the correlation function is replicated, when triggered by protons at low or intermediate values of  $p_T$ .

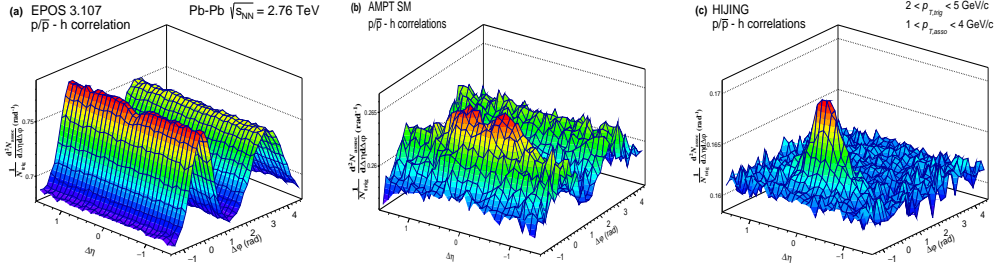


Figure 5.13: (Color online) Associated yields per trigger proton as a function of  $\Delta\phi$  and  $\Delta\eta$  for 10%-20% most central events in trigger and associated  $p_T$  ranges of  $2 < p_{T,trig} < 5$  GeV/c and  $1 < p_{T,asso} < 4$  GeV/c, respectively are shown for 3 MC models. **(a)**: EPOS 3.107 with hadronic rescattering, **(b)**: AMPT string melting (AMPT SM) with hadronic rescattering, **(c)**: HIJING, only jets and minijets. The combinatorial and flow backgrounds are not subtracted

Fig.5.13 presents the per-trigger yield from MC simulations at the generator level in the similar kinematic ranges of trigger and associated particles  $p_T$ . Both EPOS and AMPT-SM simulations show a depletion, although, the physics processes or the particle production mechanisms in the given kinematic ranges are widely different in these two models. However, no such dip is observed in HIJING simulations. Since both EPOS and AMPT-SM models are known to reproduce collective features of the QGP through hydrodynamics (EPOS) or two-body elastic parton scatterings (AMPT-SM), the depletion observed in these models suggest, that regardless of physics processes implemented, dip on the near side peak may have a “collective origin”.

Based on the peak-shape analysis by Jan-Fiete et al., [21] dip appears to be an effect of radial flow. It is suggested that the depletion is primarily related to the strength of the radial flow. However, these arguments are entirely based on the AMPT simulations that seems to reproduce the dip and also describe the peak width broadening upto some extent.

### 5.4.3 Extraction of Near Side Yield

The strength of the near side jet peak can be quantified in terms of per-trigger yield of associated hadrons, in absence of flow-correlated background in  $\Delta\phi$ . Therefore, in order to extract the pure jet-like yield, contribution from single-particle azimuthal anisotropies has to be subtracted. This is performed here using the  $\eta$ -gap method, where the 1-D  $\Delta\phi$  distribution at large  $\Delta\eta$  region ( $|\Delta\eta| > 1$ ) is subtracted from that of the  $\Delta\phi$  distributions in the short-range part ( $|\Delta\eta| < 1$ ). However, this procedure seems not to be suitable in the present scenario, because of the broadening of the peak shape [21]. When subtracting the flow-background by  $\eta$ -gap method, it must be ensured that the near side jet peak is contained within a narrow  $\Delta\eta$  region, preferably  $|\Delta\eta| < 1$ . Otherwise, some part of the jet peak, extended beyond  $\Delta\eta \approx 1$ -1.2 may get subtracted together with the flow modulated background, leading to an underestimation of the actual jet yield.

Alternatively, jet yields are extracted using a 2-D fit to the correlation function, excluding the bins within the depletion (dip) region. In the fitting function, the near side jet peak is characterized by a 2-D generalized Gaussian and, the background distribution is characterized by flow-motivated truncated Fourier series of cosine terms. The composite form of the fitting function is presented in Eq. 5.10.

$$f(\Delta\eta, \Delta\phi) = A \times \frac{\beta_{\Delta\eta} \beta_{\Delta\phi}}{4\sigma_{\Delta\eta} \sigma_{\Delta\phi} \Gamma(\frac{1}{\beta_{\Delta\eta}}) \Gamma(\frac{1}{\beta_{\Delta\phi}})} e^{-|\frac{\Delta\eta}{2\sigma_{\Delta\eta}}|^{\beta_{\Delta\eta}} - |\frac{\Delta\phi}{2\sigma_{\Delta\phi}}|^{\beta_{\Delta\phi}}} + B (1 + 2 \sum_1^4 V_n \cos(n\Delta\phi)) \quad (5.10)$$

The generalized Gaussian function has two parameters,  $\beta$  and  $\sigma$ . For  $\beta = 2$ , it reduces to a normal Gaussian distribution and, for  $\beta = 1$  it is an exponential distribution in two-dimension. The background distribution represent the

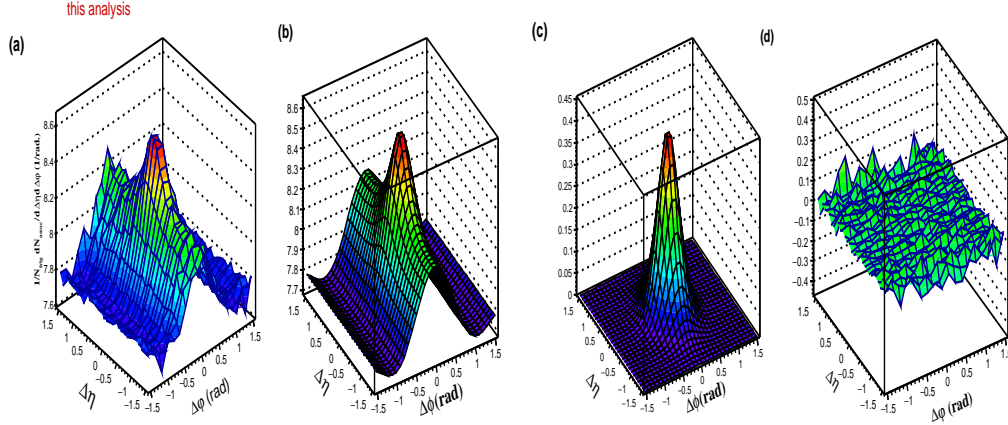


Figure 5.14: (Color online) Illustration of the fitting procedure for the 0-10% most central PbPb collisions  $\sqrt{s_{NN}} = 2.76$  TeV for pion triggered correlations in  $2.5 < p_{T,trig} < 5.0$  GeV/c and  $1.8 < p_{T,asso} < 5.0$  GeV/c: (a) the 2-D  $\Delta\eta$  and  $\Delta\phi$  distributions of associated particles per-trigger yield, (b) the 2-D fit of the near side region, (c) the signal peak component from the fit by Eq. 5.10 and (d) the difference between the data and the fit. The z-axis for all plots in this figure represent associated per-trigger yield expressed by  $\frac{1}{N_{trig}} \frac{d^2 N_{asso}}{d\Delta\eta d\Delta\phi} (rad^{-1})$ .

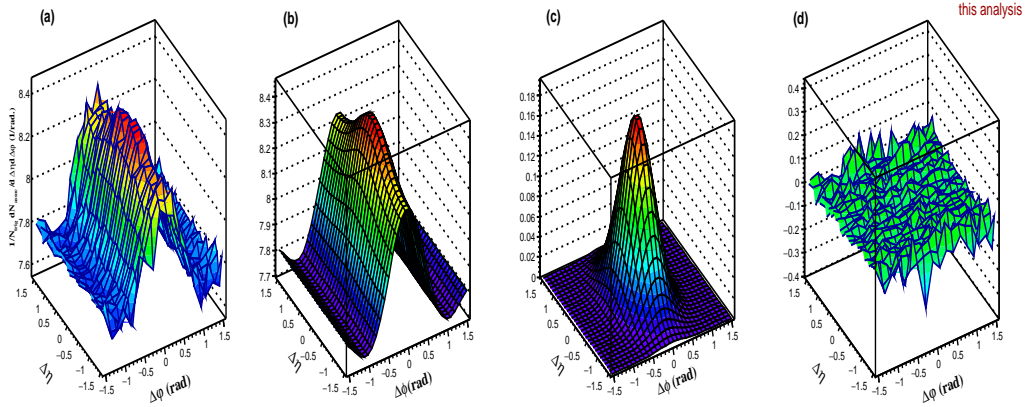


Figure 5.15: (Color online) Illustration of the fitting procedure for the 0-10% most central PbPb collisions  $\sqrt{s_{NN}} = 2.76$  TeV for proton triggered correlations in  $2.5 < p_{T,trig} < 5.0$  GeV/c and  $1.8 < p_{T,asso} < 5.0$  GeV/c: (a) the 2-D  $\Delta\eta$  and  $\Delta\phi$  distributions of associated particles per-trigger yield, (b) the 2-D fit of the near side region, (c) the signal peak component from the fit by Eq. 5.10 and (d) the difference between the data and the fit. The z-axis for all plots in this figure represent associated per-trigger yield expressed by  $\frac{1}{N_{trig}} \frac{d^2 N_{asso}}{d\Delta\eta d\Delta\phi} (rad^{-1})$

anisotropic modulation of trigger and associated ( $V_n = v_n^{trig} \times v_n^{asso}$ ) hadrons in  $|\Delta\phi|$ , over the uncorrelated combinatorial background upto fourth order in

magnitude.

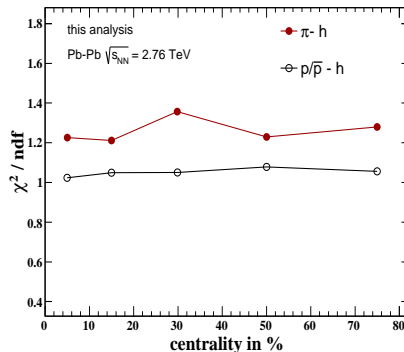


Figure 5.16: (Color online)  $\chi^2/Ndf$  of the 2-D fit to the correlation functions for pion and proton triggered correlations for all centrality classes of Pb-Pb collision at 2.76 TeV

A sample plot of 2-D fit to pion and proton triggered correlation functions are shown in Fig. 5.14 and Fig. 5.15 respectively. The goodness of the fit, measured in terms of  $\chi^2/$  No. of degrees of freedom, is shown in Fig. 5.16. Parameters extracted from these fits are used to characterize the near side peak shape. Yields are calculated at the 2-D level by integrating the area under the Gaussian peak, shown in panel (c) of Fig. 5.14 and Fig. 5.15.

## 5.5 Systematic Uncertainty

To estimate the systematic uncertainties related to this measurement, selection criteria that include tracking and particle identification efficiency, two-track resolution effects, resonance decay contributions, vertex range and the size of the exclusion region around  $\Delta\eta, \Delta\phi = (0,0)$  particularly for proton triggered correlations, shown in Fig.5.17, are varied and the analysis repeated. The uncertainties from different sources are extracted and added in quadrature. It turns out, that the domain of exclusion around the depletion region contribute dominantly to the overall uncertainty. The exclusion domain around  $\Delta\eta, \Delta\phi =$

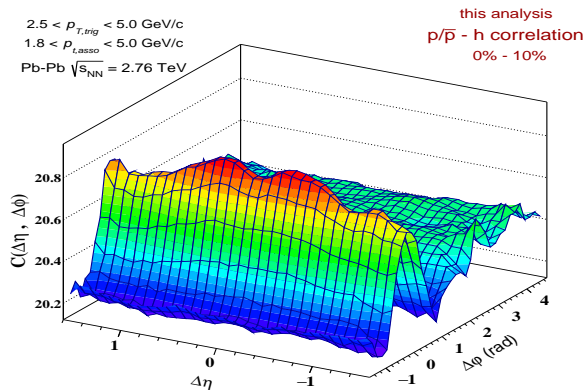


Figure 5.17: (Color online) The dip on the near side peak of proton triggered correlation is zoomed in.

(0,0) is varied from 0.05 (0.05) in the  $\Delta\eta$  ( $\Delta\phi$ ) to 0.2 (0.17). The uncertainty

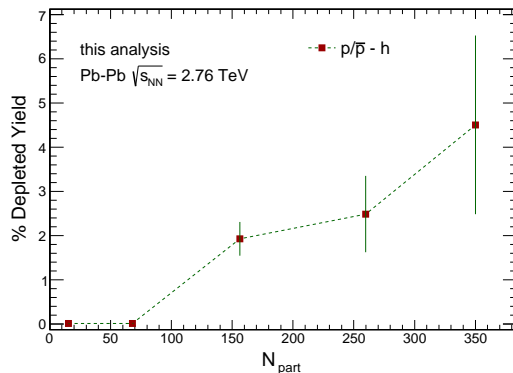


Figure 5.18: (Color online) The centrality dependence of yield in the depletion region with respect to the overall peak yield calculated from the 2-D fit. Vertical lines indicate systematic errors associated with the variation of the size of the exclusion region.

due to the depletion is evaluated by taking the difference of the fit function and the histogram in the excluded region and then dividing the difference by the normalization constant from the 2-D fit. The Fig.5.18 shows the per-trigger yield in the depletion region relative to the overall peak yield (normalization constant) as a function of centrality for proton triggered correlations in the kinematic ranges of trigger and associated  $p_T$ , where yields are extracted (Fig. 5.19). It is seen that  $(4.2 \pm 2.0)\%$  of the yield is missing in the 0%-10% most central events.

This value gradually decreases with centrality. For 40%-60% and 60%-90% centrality, depletion is not significant. These values are propagated as systematic errors when calculating the ratio of proton over pion triggered yield in Fig. 5.21.

## 5.6 Results and Discussions

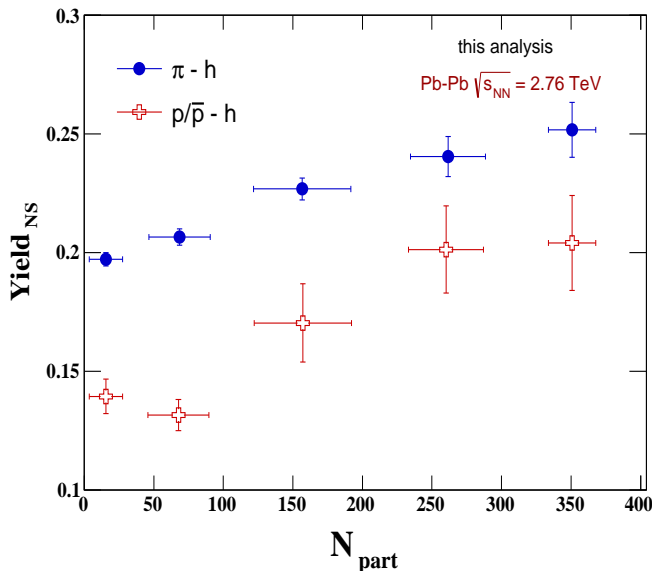


Figure 5.19: (Color online) The near side per-trigger yield of associated charged hadrons triggered by pions (blue) and protons (red) in  $2.5 < p_{T,trig} < 5.0$  GeV/c and  $1.8 < p_{T,asso} < 5.0$  GeV/c as function of  $N_{part}$  for Pb-Pb collisions at 2.76 TeV. Error bars on the yield are statistical only

In Fig. 5.19, the near side per-trigger jet yields are shown as a function of collision centrality, expressed in terms of number of participating nucleons  $N_{part}$ , for  $\pi - h$  and  $p/\bar{p} - h$  correlations in Pb-Pb collisions at 2.76 TeV. All yields are extracted from a 2-D fit to the correlation function using an analytical formulation described in Eqn. 5.10. Figure 5.19 shows that both pion and proton triggered yields increase with centrality however, the rate of increase has a trigger species dependence. The associated near side yield for pion triggered correlations increases smoothly with centrality. The proton triggered

yields are systematically lower than the pion triggered yields, but it also rises with  $N_{part}$  upto  $N_{part} < 300$ . In 0%-10% most central collisions ( $N_{part} \sim 360$ ), proton triggered yield are seen to deviate from the  $N_{part}$  dependent increase as observed in the  $\pi$ -h correlations for all values of  $N_{part}$ . Within the limits of statistical uncertainties, proton triggered yields in 0%-10% and 10%-20% centrality classes are consistent and seems to have saturated.

Similar measurements were performed at top-RHIC energy for  $p_{T,asso}$  and  $p_{T,trig}$  ranges of  $1.8 < p_{T,asso} < 2.5$  GeV/c and  $2.5 < p_{T,asso} < 4.0$  GeV/c, respectively [10, 11]. As shown in Fig. 5.20, the near side yield per meson trigger increases linearly with centrality whereas, the near side associated yield per baryon trigger is suppressed in the most central collisions, after an initial rise. It was observed that the baryon triggered yield at most central collisions is consistent with the yield extracted from the baryon triggered correlations in peripheral events within error bar.

Lately, STAR Collaboration, using statistically separated samples of pion and non-pion triggers [12], also reported similar observation consistent with the earlier measurements by the PHENIX collaboration as discussed above. The associated yield per pion trigger is seen to have increased in central Au-Au collisions compared to the minimum bias d-Au collisions at the same energy. However, the associated yield per non-pion trigger was measured to be similar in both of these systems.

It can therefore be concluded, at RHIC and LHC energies, the behaviour of meson triggered yields are qualitatively similar. It has been observed, that both at RHIC and LHC the jet-like yield associated with pion triggers in central Au-Au/Pb-Pb collisions is enhanced with respect to d-Au / peripheral collisions at the same energy. The enhancement is seen to be of the order of 24% at

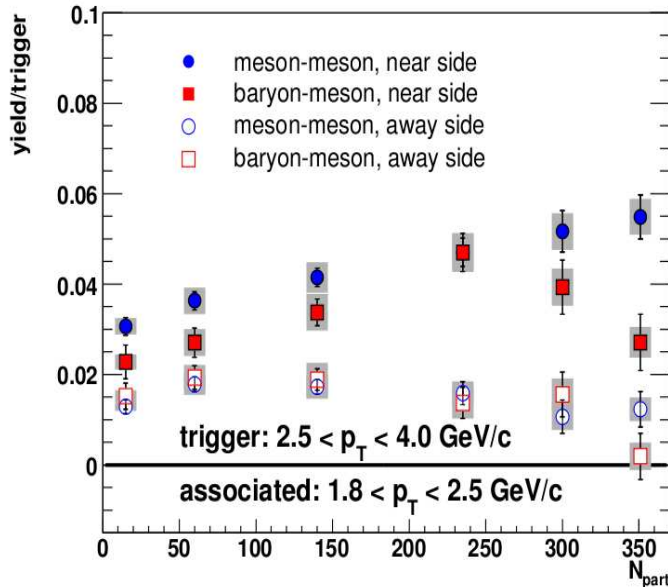


Figure 5.20: (Color online) The near side yields per trigger for baryon (squares) and meson (circles) triggers with associated mesons. Triggers have  $2.5 < p_{T,trig} < 4.0$  GeV/c and associated particles have  $1.8 < p_{T,asso} < 2.5$  GeV/c. The error bars are the statistical errors and the boxes show the systematic errors. There is an additional 13.6% normalization error [11].

RHIC and 31% at LHC in the respective  $p_{T,trig}$  and  $p_{T,asso}$  ranges. As it can be seen from Fig. 5.20, the proton triggered yield at RHIC does not show any enhancement in central collisions and, seen to have similar values as that of the reference measurement in d-Au/peripheral Au-Au collisions. However, at LHC energy, the present analysis shows that proton triggered yield is also enhanced as a function of centrality, leading to a saturation in 10%-20% and 0%-10% centrality bins of Pb-Pb collisions. The relative enhancement at saturation with respect to peripheral collisions at same energy is seen to be  $\approx 25$ -26%. The proton trigger yield in 60%-90% and 40%-60% peripheral bins are however, seen to be consistent within the error bar. Previous measurements have shown that the jet-like yield associated with the unidentified charged hadron triggers is also enhanced when studied as a function of collision centrality in a range of trigger and associated  $p_T$ , as discussed here. Since majority of the charged

particles are pions, results obtained for identified triggered correlations seems to be consistent.

The enhancement of jet-like yield of the soft hadrons associated with pions/unidentified charged hadron triggered correlations may be attributed to the jet-quenching and/or medium-induced modification of fragmentation functions. On the other hand, the observed suppression (or lack-of enhancement) for non-pion or baryon triggers might be interpreted as a combined effect of competing processes that involve jet-medium interactions and quark recombination. If particles are dominantly produced from the recombination of boosted thermal quarks, suppression in the per-trigger yield could be naturally expected, because hadrons created from the recombination of thermal partons are unlikely to have jet-like correlated partners in small angles. This suppression or dilution in the per-trigger yield would be stronger for baryons, as baryons are dominantly produced from such a mechanism than mesons. The initial rise in case of proton triggered correlation could be an effect of modification of jet fragmentation in a color charged medium. This could be a dominant effect in lower centrality. But, with the increase in centrality, the effect of recombination takes over and more baryons are produced without associated hadrons. The combined effect of these two competing processes results in the saturation of the yield.

However, at LHC, the large enhancement of intermediate  $p_T$  baryons over mesons, is also seen to be consistent with the hydrodynamics [7]. In hydrodynamical models, baryon enhancement is treated as an effect of radial flow that boost heavy particles to higher values of  $p_T$  relative to lighter ones. The peak of proton-to-pion ratio at LHC is approximately 20% larger than at the RHIC, consistent with the increase in the average radial flow velocity at LHC, of similar magnitude (20-30%).

These results have triggered a lot of debates on the possible origin of baryon-to-meson enhancement. Based on the inclusive measurements of identified particles and quark-number scaling of  $v_2$  at intermediate- $p_T$ , it seems, baryon-meson difference at LHC is congruous with the mass of the particle and hence could be explained in the realms hydrodynamical models without requiring an additional mechanism hadronization, such as quark recombination. An attempt is being made to test the interpretation of baryon-to-meson enhancement at intermediate- $p_T$  in a hydrodynamic model using the present correlation measurements. To make a quantitative statement, results presented here for identified triggered correlations are compared with that obtained from Monte Carlo models, like, EPOS [22] and string melting version of AMPT (AMPT-SM) [23], that have implemented hydrodynamics and coalescence, respectively.

### 5.6.1 Model Comparison

EPOS [22] is a hybrid MC event generator that contains both soft and hard physics. It implements a flux-tube initial condition followed by a hydrodynamical phase, modelled by 3+1D viscous hydrodynamics. An additional hadronization process is implemented at intermediate- $p_T$ , where the jet-fluid interaction gives an additional momentum push to baryons compared to mesons. Thus, this interaction results in an increased yield of baryons over mesons at intermediate- $p_T$ . Although this model reproduces the centrality dependence of inclusive baryon-to-meson enhancement qualitatively well, but it overestimates the magnitude.

AMPT [23], on the other hand, derives its initial conditions from the HIJING event generator in terms of spatial and momentum distributions of strings and mini-jet partons. This is followed by an incoherent scatterings of mini-jet and string-melted partons. Once the interactions seize, nearest neighbour quarks

coalesce to hadrons. Hadrons are then transported through a A Relativistic Transport (ART) model that accounts for the hadronic interactions prior to the final freeze-out.

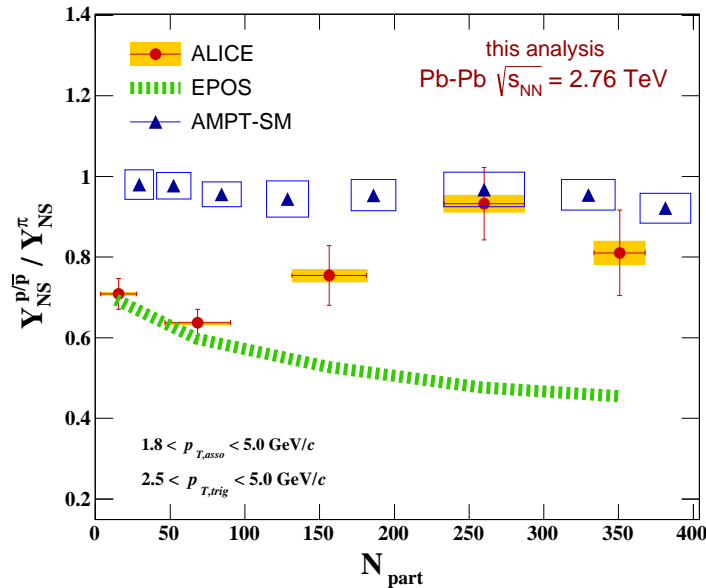


Figure 5.21: (Color online) The ratio of the per-trigger jet-like yield of protons to that of the pions are shown as function of collision centrality, characterized by  $N_{part}$ . The blue triangle and green dashed line represent comparison with AMPT-SM and EPOS MC event generators, respectively. Error bars are statistical and the boxes denote the systematic uncertainty primarily due to the loss of small angle correlated pairs in the depletion region for proton triggered correlations.

Fig. 5.21 presents the centrality dependence of the ratio of associated yields for pion and proton triggered correlations for Pb-Pb collisions at 2.76 TeV. This ratio quantifies the relative modification in the proton triggered yield compared to pions. The ratio increases with the increase in centrality upto mid-central collisions, followed by a marginal reduction (or saturation) in the 0%-10% most central collision. This suggests that both pion and proton triggered yields increase with the centrality but the rate of increase is relatively higher for protons, except in the most central collisions where proton triggered yield might have reduced to some extent.

This measurement is compared with EPOS and AMPT models at the same kinematic range, but none of the models could describe the data points over the entire centrality region. At the most central bins, AMPT is seen to be closest to data as compared to that of EPOS. A combination of hydrodynamics and jet-quenching as implemented in EPOS seems to suggest that shifting of protons from low to intermediate or high- $p_T$  region results in an increased suppression of the ratio of proton to pion triggered yield ( $Y_{NS}^{p/\bar{p}}/Y_{NS}^{\pi^\pm}$ ) with centrality. In a recent publication [24] it has been shown that the increasing suppression of this ratio with multiplicity/centrality is because of the enhancement in soft proton trigger particles which lack jet-like correlated partners. This happens because of the radial flow that shifts more of heavy particles to higher- $p_T$  relative to lighter ones. Thus, the number of soft trigger protons at intermediate- $p_T$  is relatively more compared to pions leading to an enhanced suppression of proton triggered yield compared to that of the pions. In AMPT,  $Y_{NS}^{p/\bar{p}}/Y_{NS}^{\pi^\pm}$  is seen to exhibit no multiplicity dependence. This result can be contrasted with the model simulation discussed in chapter 2, in which at low  $p_{T,trig}$  region,  $Y_{NS}^{p/\bar{p}}/Y_{NS}^{\pi^\pm}$  shows suppression in the most central collisions. As the present  $p_{T,trig}$  range, which is higher than that investigated in chapter 2, lack of any suppression indicate that contributions from thermal recombination fall off sharply at high- $p_T$  [25]. Also, it must be noted that the region of baryon excess in data and AMPT are different. If the above ratio is calculated in the respective regions of baryon excess, it is seen that the ratio  $Y_{NS}^{p/\bar{p}}/Y_{NS}^{\pi^\pm}$  in AMPT is progressively suppressed with increasing centrality [25]. However, the trend in data is completely different. After an initial rise it saturates or marginally suppressed. Since the color charge and radiative processes of energy loss are missing in AMPT, the difference between data and AMPT model might indicate the significance of in-elastic processes of energy loss, as well as, the differences in the relative contributions

from quark and gluon jets.

# Bibliography

- [1] Z.W. Lin and C. M. Ko, Phys. Rev. Lett. 89, 202302 (2002); D. Molnar and S. A. Voloshin, Phys. Rev. Lett. 91, 092301 (2003); R. C. Hwa and C. B. Yang, Phys. Rev. C 67, 064902 (2003); R. J. Fries, B. Muller, C. Nonaka, and S. A. Bass, Phys. Rev. Lett. 90, 202303 (2003); V. Greco, C. M. Ko, and P. Levai, Phys. Rev. Lett. 90, 202302 (2003).
- [2] B. I. Abelev et al. (STAR Collaboration), Phys. Rev. Lett. 97, 152301 (2006).
- [3] B. I. Abelev et al. (STAR Collaboration), Phys. Rev. C 75, 054906 (2007).
- [4] B. Abelev et al. (ALICE Collaboration), Phys. Lett. B 736, 196-207 (2014).
- [5] B. Abelev et al. (ALICE Collaboration), Phys. Rev. Lett. 111, 222301 (2013).
- [6] B. Abelev et al. (ALICE Collaboration), JHEP 06 190, (2015).
- [7] J. Adam et al. (ALICE Collaboration), Phys. Rev. C 93, 034913 (2016).
- [8] B. Abelev et al. (ALICE Collaboration), Phys. Rev. C 91, 024609 (2015).
- [9] S. Singha and Md. Nasim, Phys. Rev. C 93, 034908 (2016).

- [10] S.S. Adler et al. (PHENIX Collaboration), Phys. Rev. C 71, 051902 (2005).
- [11] A. Adare et al. (PHENIX Collaboration), Phys. Lett. B 649 359-369, (2007).
- [12] N.M. Abdelwahab et al. (STAR Collaboration), Phys. Lett. B 751, 233240 (2015).
- [13] B. Abelev et al. (STAR Collaboration), arXiv:1603.05477, (2016).
- [14] P. Abreu et al., (DELPHI Collaboration), Eur. Phys. J. C 17, 207-222 (2000).
- [15] S. Sapeta and U. A. Wiedemann, Eur. Phys. J. C 55, 293-302 (2008).
- [16] P. Aurenche and B. Zakharov, Eur. Phys. J. C 71, 1829 (2011).
- [17] S. Chatrchyan et al., (CMS Collaboration), JHEP 1210 087, (2012).
- [18] Rudolph C. Hwa and C. B. Yang, Phys. Rev. C 70, 024905 (2004).
- [19] R. J. Fries et al., Phys. Rev. Lett. 90, 202303 (2003) and Phys. Rev. C 68, 044902 (2003).
- [20] Alis Rodriguez Manso, CERN-THESIS-2015-227. - 137 p.
- [21] ANA-56 <https://aliceinfo.cern.ch/Notes/node/33>
- [22] K. Werner, Phys. Rev. Lett. 98 (2007) 152301 ; K. Werner, et al., Phys. Rev. C 82, 044904 (2010) ; K. Werner, et al., Phys. Rev. C 89 064903, (2014) ; K. Werner, Iu. Karpenko, T. Pierog, Phys. Rev. Lett. 106, 122004 (2011) ; K. Werner, et al., Phys. Rev. Lett. 112, 232301 (2014).
- [23] Z.-W. Lin, C.M. Ko, B.-A. Li, B. Zhang, S. Pal, Phys. Rev. C 72, 064901 (2005).

- [24] D. Sarkar, S. Choudhury, and S. Chattopadhyay, Phys. Lett. B, pp 763-768 (2016).
- [25] S. Choudhury, D. Sarkar, and S. Chattopadhyay, Phys. Rev. C 93, 054902 (2016).

# Appendix

## Fabrication large size oil free Bakelite RPC

The single-gap Resistive Plate Chambers or RPCs [1] are robust and cost-effective gas-filled detectors which have been extensively used in high energy physics experiments because of its excellent time resolution (about 1 nano-sec). A single gap RPC utilizes a pair of highly resistive parallel plate electrodes that conceive an uniform gas-gap and maintains a constant and uniform electric field. The electrodes are generally made of special grades of glass or High Pressure Laminate (HPL), familiar as bakelite, having bulk resistivity of the order of  $10^{10-12} \Omega \text{ cm}$ .

As a choice of electrode material, bakelite is preferred over glass as it simplifies the construction process and minimises the scope of mechanical damages as well. Since bakelite can be casted into large sheets of micron level thickness, it also finds application in fabricating detectors requiring large surface area.

In the upcoming India-based Neutrino Observatory (INO) [2], an underground facility for neutrino research, bakelite-RPCs are candidates for the active detectors to track muons in the INO-ICAL (Iron Calorimeter). As proposed, 30K RPC modules each of dimension  $200 \text{ cm} \times 200 \text{ cm} \times 0.2 \text{ cm}$  would be sandwiched between each pair of 140 layers of magnetized iron plate (ICAL) that weighs almost 50 ktons. This experimental condition demands, that RPCs

to be used should be rugged and have high longevity, along with good timing (1-2 nano-sec) and moderate spatial ( $\sim 1$  cm) resolution. As a member of this collaboration, Variable Energy Cyclotron Centre (VECC), Kolkata, India, has been actively involved in the research and development of RPCs using high pressure paper laminate sheets procured from local industries in India [3, 4, 5].

Despite several advantages, bakelite RPCs are however, vulnerable to ageing [6]. It has been shown, with time its surface smoothness and hence the detector efficiency reduces drastically. To counter the ageing effect, it is a common practice to use HPL-sheets coated with polymerized linseed oils [7]. Such surface treatment although ensures long term stability of the chamber but has its own de-merits.

In case of oil-treated RPCs, uncured oil droplets accumulate in the form of “stalagmites” [8] on the inner surface of the HPL plates. These droplets offer a low-resistive path to the current across the gas gap resulting in high leakage current. Investigations have revealed that the surface resistivity of the oil-treated HPL changes during its course of operation. These problems were however, eliminated by using cured linseed oil [9].

Although surface treatments with oil significantly improves the detector performance [7] but continuous efforts are being made to look for its alternative or to develop glossy finished bakelite surfaces which could be used without further oil treatment. The work reported here is a parallel effort to fabricate a large oil-free HPL-RPC for prolonged stable operation [4].

## Detector Fabrication

A 240 cm  $\times$  120 cm  $\times$  0.2 cm oil-free bakelite RPC, shown in Fig. 5.22, was fabricated using raw materials like bakelite sheets, glue, spacers available in Indian market. A detailed characterization of the HPL sample was done by

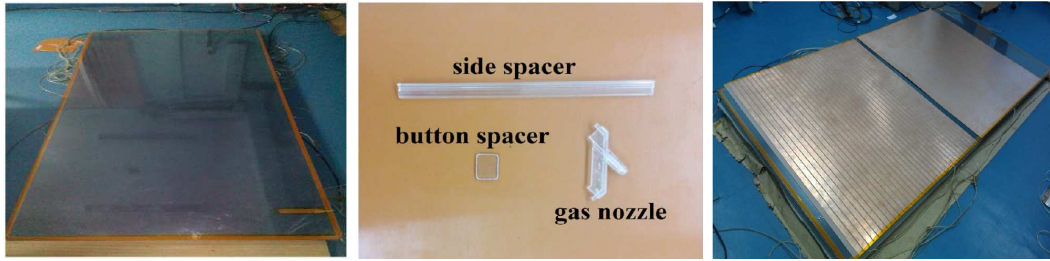


Figure 5.22: (Color Online) **Left**: Photograph of graphite coated RPC module, **Middle**: Button and side spacers, **Right**: Photograph of RPC module with pick-up panel used for signal extraction

measuring its surface and bulk resistivities. Fig.5.23 shows the measured bulk and surface resistivities of the HPL sample as a function of the applied high voltage. The average value of the bulk resistivity of the sample was found to be  $\sim 9 \times 10^{11} \Omega \text{ cm}$  whereas, the surface resistivity was measured to be  $\sim 3 \times 10^{11} \Omega / \square$ . These values were found to suit the requirements of RPC electrode [10].

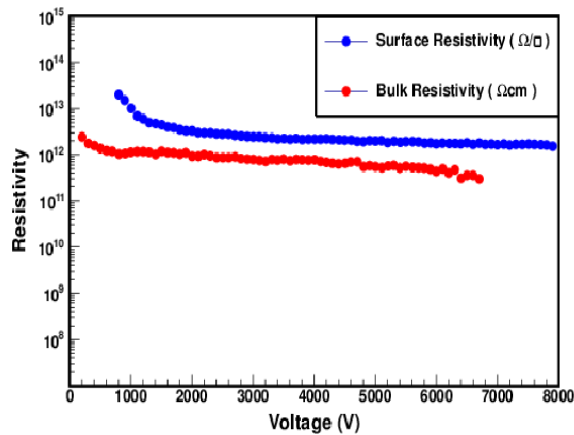


Figure 5.23: (Color online) Variation of surface and bulk resistivities as a function of applied voltage.

To maintain uniform gas-gap and provide mechanical support to the chamber, two type of spacers were used - button spacers and side spacers (see Fig. 5.22, middle panel). Glues were applied on the surface of the spacers to fix them on the electrode surface. Since glues could be source of high-leakage

current of the RPCs, resistivity of the glue should be an order of magnitude higher than the electrodes. Several grades of glue samples were tried and one with bulk resistivity of  $\sim 10^{14} \Omega\text{cm}$  (100 times higher than the electrodes) was chosen for the fabrication of the chamber.

Several other intermediate steps, which are indeed essential for the fabrication of such large sized detector are not mentioned here. A detailed description of detector fabrication, illustrating several hurdles of fabricating this detector along with the techniques improvised to overcome the challenges are thoroughly documented in [11, 12].

## Test Results

The RPC was tested with cosmic rays in a standard cosmic ray test set-up. All tests were performed in the streamer mode of operation of the RPC with a gas mixture of Argon:Freon(R134a):Iso-butane::34:57:9 by volume. A typical gas flow rate of  $\sim 0.75$  litre/hour was maintained over the entire testing period yielding a  $\sim 3$  changes of gas volume per day. The current of the detector was found to remain stable over the period operation. Over the entire testing period, temperature and relative humidity in the laboratory was maintained at  $\sim 20^\circ\text{C}$  and 45% - 55% respectively.

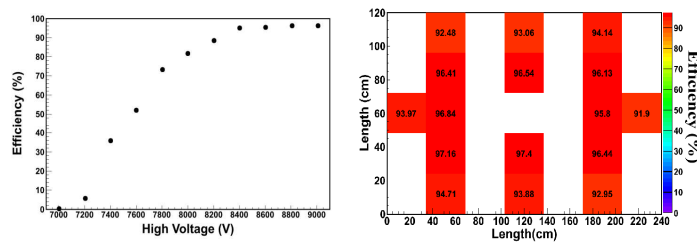


Figure 5.24: (Color Online) RPC performance, **Left**: Efficiency as a function of applied voltage, **Right**: Plot showing spatial efficiency distribution. Different locations where efficiency values were measured are highlighted in red color (not upto the scale).

At a signal threshold of -20 mV and  $\sim 0.75 \text{ Hz/cm}^2$  noise rate, the average

efficiency of RPC was measured to be  $> 95\%$  at 9kV. Fig. 5.24 shows the uniformity of the detector performance. Efficiency values were measured at 16 different locations and the variation was noted to be  $< 10\%$ . Time resolution of the detector was measured at a central location and found to be  $\sim 0.83$  nano-sec at 9kV, comparable to the values reported in [1, 5].

Long term testing of the detector is currently underway. Results available from the cosmic ray test over a period of 60 days [13] indicate that the chamber remains appreciably stable in terms leakage current, efficiency, noise rate and time resolution. The results obtained are compatible with the requirements for muon detection in large neutrino experiments and hence this particular grade of HPL-sheet might find applications in the development of development of large size (240 cm  $\times$  120 cm) RPCs for INO-ICAL or in the Near Detector (ND) of the Deep Underground Neutrino Experiment (DUNE) [14].

# Bibliography

- [1] R. Santonico, R. Cardarelli, Nucl. Instr. and Meth. 187 (1981) 377., G. Aielli, et al., Nucl. Instr. and Meth. A 714, 115-120 (2013) .
- [2] INO Project Report, INO/2006/01,  
<http://www.ino.tifr.res.in/ino//OpenReports/INOREport.pdf>.
- [3] S. Biswas, et al., Nucl. Instr. and Meth. A 617, 138-140 (2010).
- [4] S. Biswas, et al, Nucl. Instr. and Meth. A 602, 749 (2009).
- [5] S. Biswas, et al, Nucl. Instr. and Meth. A 604, 310-313 (2009).
- [6] J. Vavra, Nucl. Instr. and Meth. A 515, 354 (2003) .
- [7] M. Abbrescia, et al., Nucl. Instr. Methods A 394, 13-20 (1997).
- [8] F. Anulli et al., Nucl. Instr. and Meth. A 508, 128 (2003) ; F. Anulli et al., Nucl. Instr. and Meth. A 508, 455 (2003).
- [9] F. Anulli et al., Nucl. Instr. and Meth. A 552, 276-291 (2005) ; F. Ferroni et al., Nucl. Instr. and Meth. A 602, 649-652 (2009).
- [10] K. K. Meghna, et al., JINST 7 P10003 (2012).
- [11] *Probing the Earth Matter Density through INO-ICAL and related Detector Development*, Rajesh Ganai thesis in preparation.
- [12] R. Ganai et al., JINST 11 P04026 (2016), arXiv:1510.02028.

[13] R. Ganai et al., arXiv:1604.03668.

[14] <http://www.dunescience.org/>.